

# Control of Topological Magnetic Textures by Magnetic and Electric Fields in Magnetoelectric Helimagnet $\text{Cu}_2\text{OSeO}_3$

THÈSE N° 7719 (2017)

PRÉSENTÉE LE 27 AVRIL 2017

À LA FACULTÉ DES SCIENCES DE BASE  
LABORATOIRE DE MAGNÉTISME QUANTIQUE  
PROGRAMME DOCTORAL EN PHYSIQUE

ÉCOLE POLYTECHNIQUE FÉDÉRALE DE LAUSANNE

POUR L'OBTENTION DU GRADE DE DOCTEUR ÈS SCIENCES

PAR

Ping HUANG

acceptée sur proposition du jury:

Prof. F. Mila, président du jury  
Prof. H. M. Rønnow, directeur de thèse  
Dr I. Kézsmárki, rapporteur  
Prof. A. Rosch, rapporteur  
Prof. F. Carbone, rapporteur



ÉCOLE POLYTECHNIQUE  
FÉDÉRALE DE LAUSANNE

Suisse  
2017



江天一色无纤尘，皎皎空中孤月轮。

江畔何人初见月，江月何年初照人。





# Acknowledgements

It has always been very very difficult for me to write the acknowledgement because there are always so many nice people and experiences that I am deeply grateful. Thus I would like to dedicate this work to all of these in token of gratitude!

Please let me express special appreciation to my supervisor Prof. Henrik M. Rønnow. I have been feeling very lucky since the very beginning of my Ph.D under his supervision, and as time passes by, this feeling are becoming stronger and stronger. Prof. Rønnow can always give very insightful instructions on my work and is ready for patient discussions almost any time I need. He has been demonstrating by his actions what he said to me "education is my first priority". Besides, Prof. Rønnow keeps me very free in my research with his warm encouragement and valuable suggestions so that some work in this thesis that is out of the initial plan can be accomplished. Only during these free explorations that I can build the ability of independence. On the other hand, I have also got precious enlightenment from his rather simple but very positive and constructive attitude towards life. What I learned from Prof. Rønnow will definitely inspire me throughout my professional and personal life.

I would also like to express my deep gratefulness to Dr. Marco Cantoni, who intensively instructed and helped me in all my LTEM experiments. As one of the few experts that know very well of the instruments in CIME, EPFL and in charge of them, Dr. Cantoni has, of course, been very busy, but even so, he still showed up every time I needed, teaching and helping me with his profound knowledge and rich experience from sample preparation to various crucial details of LTEM operations. It is really difficult to imagine how I can finish my work in this thesis without him. His optimism and humor is a very efficient catalyst for the research, especially during those tough stages.

Thanks to Prof. Rønnow and all the colleagues, the highly creative and harmonic atmosphere in LQM makes it really a wonderful lab. Specifically, working with Dr. Ivica Živković and Dr. Julian Piatek gave me the opportunity to learn lots of knowledge on the low temperature experiments, and frequent discussions with Dr. Arash A. Omrani, Alex Kruchkov, Dr. Peter Babkevich, Dr. Minki Jeong, Dr. Bastien Dalla Piazza, Dr. Jonathan S. White and Prof. Johan Chang broadened my view of points in various aspects of quantum magnetism. I also enjoyed working and discussing with Claudia G. Fatuzzo, Noore Elahi Shaik and all the TP4 and master students worked in the lab. A special gratefulness should be given to our secretary Caroline A.

## Acknowledgements

---

Pletscher. Her kind help made me get through many difficulties as a foreigner.

I would like to thank our collaborators for their efforts in promoting the research and especially for what I learned from them: Dr. Arnaud Magrez from the Crystal Growth Facility. Prof. Fabrizio Carbone, Dr. Rajeswari Jayaraman and Dr. Yoshie Murooka from LUMES, EPFL. Dr. Yu Xiu Zhen and Prof. Yoshinori Tokura from RIKEN. Prof. Thierry Giamarchi from the University of Geneva. Dr. Damien McGrouther from the University of Glasgow.

*Lausanne, 14 January 2017*

HUANG Ping

# Abstract

Magnetic skyrmions, topologically non-trivial chiral whirl-like spin configurations, have been under massive investigations in both fundamental and application aspects. In some special compounds, these quasi-particles can form triangular skyrmion lattice (SkL) exhibiting abundant unique properties. This thesis presents my comprehensive studies on the SkL in the magnetoelectric (ME) coupling helimagnet  $\text{Cu}_2\text{OSeO}_3$ .

Starting from measurements on single crystal bulk  $\text{Cu}_2\text{OSeO}_3$  samples, including dc magnetization, magnetoelectric susceptibility and neutron scattering, so as to get the general understanding of this system, the main work of this thesis focused on the investigation of quasi-two dimensional thin slab samples by the state-of-the-art Lorentz electron transmission electron microscopy (LTEM). Various magnetic textures including the spin helices and skyrmions were observed and analyzed. What separates the work presented here from literatures is the special emphasis on the dynamics of the SkL under various excitations in real space and real time, such as thermal fluctuation, magnetic field and electric field. Specifically, the magnetic field induced melting of the SkL in  $\text{Cu}_2\text{OSeO}_3$  was, for the first time, observed and analyzed quantitatively. Two-step melting process was observed and demonstrated to follow the Kosterlitz-Thouless-Halperin-Nelson-Young (KTHNY) theory. The application of electric field can not only rotate the SkL, but also create skyrmions from the helical phase.

My studies, especially those focused on the emergent properties induced by external fields, are intended to provide deeper insight into the fundamental knowledge of the SkL in  $\text{Cu}_2\text{OSeO}_3$  and to promote the the development of skyrmion based spintronic applications.

Key words:

skyrmions, magnetoelectric coupling, Lorentz electron transmission microscopy, 2D crystal melting



# Résumé

Les skyrmions magnétiques, des configurations de spin chirales topologiquement non triviales, ont été sous des enquêtes massives à la fois fondamentales et applicatives. Dans certains composés, ces quasi-particules peuvent former un treillis de skyrmion (SkL) propriétés uniques. Cette thèse présente mes études approfondies sur le couplage magnéto-électrique (ME) helimagnet  $\text{Cu}_2\text{OSeO}_3$ .

A partir de mesures sur des échantillons en vrac monocristallins  $\text{Cu}_2\text{OSeO}_3$ , y compris la magnétisation en courant continu, Susceptibilité magnéto-électrique et la diffusion des neutrons, de manière à obtenir compréhension de ce système, le travail principal de cette thèse a porté sur l'étude Des échantillons de films minces quasi-bidimensionnels par la transmission électronique à l'état de l'art de Lorentz Microscopie électronique (LTEM). Diverses textures magnétiques incluant les hélices de spin et on a observé et analysé des skyrmions. Ce qui fait le travail présenté ici à partir de littératures Est l'accent particulier sur la dynamique de la SkL sous diverses excitations dans l'espace réel Et le temps réel, tels que la fluctuation thermique, champ magnétique et champ électrique. Plus précisément, le La fusion induite par champ magnétique de la SkL dans  $\text{Cu}_2\text{OSeO}_3$  a été, pour la première fois, observée et analysées quantitativement. Le processus de fusion en deux étapes a été démontré pour suivre le KTHNY theorie. L'application du champ électrique peut non seulement faire tourner le SkL, mais aussi créer des skyrmions de la phase hélicoïdale.

Mes études, en particulier celles axées sur les propriétés émergentes induites par des champs externes, sont on croit fournir un aperçu plus profond de la connaissance fondamentale de la SkL dans  $\text{Cu}_2\text{OSeO}_3$  et de favoriser fortement le développement d'applications spintroniques basées sur le skyrmion.

Mots clés:

Skyrmions, couplage magnétoélectrique, microscopie à transmission d'électrons de Lorentz, fusion de cristaux 2D



# Contents

<b>Acknowledgements</b>	<b>i</b>
<b>Abstract</b>	<b>iii</b>
<b>Résumé</b>	<b>v</b>
<b>Table of contents</b>	<b>vii</b>
<b>List of figures</b>	<b>ix</b>
<b>List of tables</b>	<b>xi</b>
<b>Chapter 1 Introduction</b>	<b>1</b>
1.1 Magnetic skyrmions . . . . .	1
1.2 Some properties of skyrmions . . . . .	3
1.2.1 Topology . . . . .	4
1.2.2 Topological Hall effect . . . . .	4
1.2.3 External control . . . . .	6
1.3 Skyrmion lattice . . . . .	7
1.3.1 Spin configuration of skyrmion lattices . . . . .	7
1.3.2 Properties of skyrmion lattices . . . . .	8
1.4 Content of the thesis . . . . .	9
<b>Chapter 2 Properties of bulk single crystal <math>\text{Cu}_2\text{OSeO}_3</math></b>	<b>11</b>
2.1 Basic model for $\text{Cu}_2\text{OSeO}_3$ . . . . .	11
2.1.1 Magnetic interactions and phases . . . . .	11
2.1.2 Magnetoelectric coupling . . . . .	14
2.2 Experimental results and analysis . . . . .	17
2.2.1 Magnetic properties . . . . .	17
2.2.2 Magnetoelectric susceptibility . . . . .	17
2.2.3 Small angle neutron scattering with electric field . . . . .	24
2.3 Conclusion . . . . .	27
	vii

## Contents

---

<b>Chapter 3 Static investigation of SkL by LTEM</b>	<b>29</b>
3.1 Introduction to Lorentz transmission electron microscopy . . . . .	29
3.2 Experiments . . . . .	33
3.3 LTEM observation of the helical phase . . . . .	34
3.4 Magnetic field induced helical to SkL phase transition . . . . .	37
3.5 Defects and fluctuations in SkL . . . . .	38
3.6 Discussion . . . . .	42
3.7 conclusion . . . . .	43
<b>Chapter 4 Magnetic field induced melting of SkL</b>	<b>45</b>
4.1 Introduction to 2D lattice melting . . . . .	45
4.1.1 Topological defects and the KTHNY theory . . . . .	46
4.2 Experiments and results . . . . .	48
4.3 Quantitative analysis . . . . .	50
4.3.1 Pair correlation function . . . . .	50
4.3.2 Structure factor . . . . .	53
4.3.3 Orientational and translational correlation functions . . . . .	55
4.4 Discussions . . . . .	58
4.5 Conclusion . . . . .	59
<b>Chapter 5 SkL dynamics induced by electric field</b>	<b>61</b>
5.1 Experiments . . . . .	62
5.2 E-field induced rotation of SkL . . . . .	63
5.3 E-field creation and annihilation of skyrmions . . . . .	65
5.4 Discussion . . . . .	72
5.5 Conclusion . . . . .	73
<b>Chapter 6 Conclusion and outlooks</b>	<b>75</b>
6.1 Conclusion . . . . .	75
6.2 Outlooks . . . . .	76
6.2.1 For fundamental research . . . . .	76
6.2.2 For application . . . . .	76
<b>Appendix A Image processing</b>	<b>79</b>
A.1 Image filters . . . . .	79
A.2 Image registration . . . . .	81
<b>Appendix B Algorithm of skyrmion identification</b>	<b>83</b>
B.1 Images full of skyrmions . . . . .	83
B.2 Images with both skyrmions and helices . . . . .	84
<b>Bibliography</b>	<b>93</b>
<b>Curriculum Vitae</b>	<b>95</b>



# List of Figures

1.1	Spin configurations of Néel and Bloch type skyrmions and topological equivalences	2
1.2	Interfacial DM interaction	3
1.3	Topological Hall effect	5
1.4	EEMF induced by skyrmions	6
1.5	Spin configuration of the skyrmion lattice	7
1.6	Phase diagram of MnSi	8
2.1	Crystal structure of $\text{Cu}_2\text{OSeO}_3$	12
2.2	Helical and conical spin configurations	13
2.3	Phase diagrams of $\text{Cu}_2\text{OSeO}_3$	15
2.4	Electric polarization distribution of $\text{Cu}_2\text{OSeO}_3$ skyrmions	16
2.5	M-T curves of $\text{Cu}_2\text{OSeO}_3$	18
2.6	M-H curves of $\text{Cu}_2\text{OSeO}_3$	19
2.7	$dM/dE$ setup	20
2.8	$dM/dE$ temperature scan	21
2.9	$dM/dE$ field scan	22
2.10	$dM/dE$ phase diagram	23
2.11	SANS setup and sample geomerty	24
2.12	E-field SANS	26
3.1	Principle of LTEM	30
3.2	TIE analysis of magnetite	32
3.3	Sample thickness	33
3.4	Low temperature LTEM setup	34
3.5	Helical phase with two domains	35
3.6	Defects in the helical phase	35
3.7	Helical to SkL phase transition	36
3.8	Skyrmions in helices	37
3.9	TIE analysis of the SkL	39
3.10	Dislocations in the SkL	40
3.11	Temporal fluctuations of the SkL	41
3.12	E-beam induced rotation of the SkL	42
4.1	Illustration of dislocations	46

## List of Figures

---

4.2	Illustration of the formation of a dislocation pair by mismatch. The figures are reproduced from Ref. [1]. . . . .	47
4.3	Illustration of disclinations . . . . .	47
4.4	Illustration of SkL melting induced by magnetic field and temperature respectively. . . . .	48
4.5	B-field induced melting of the SkL . . . . .	49
4.6	Pair correlation functions . . . . .	52
4.7	Structure factors . . . . .	54
4.8	Orientational correlation function $G_6(r)$ . . . . .	57
4.9	Translational correlation function $G_k(r)$ . . . . .	57
5.1	E-field LTEM sample . . . . .	62
5.2	E-field induced rotation of the SkL . . . . .	64
5.3	E-field dependence of the SkL orientation . . . . .	65
5.4	Rotation by splitting into domains . . . . .	66
5.5	E-field creation/annihilation of skyrmions . . . . .	67
5.6	Real space images of the moving of the SkL domain boundary in the helical phase background as a function electric field. . . . .	70
5.7	Number of skyrmions as a function of bipolar E-field . . . . .	71
A.1	LoG filtering of images . . . . .	80
A.2	Image registration . . . . .	82
B.1	Illustration of the dynamical box algorithm. . . . .	83
B.2	Orientational map of an image containing two helical domains. . . . .	84
B.3	Skyrmion identification . . . . .	85

## List of Tables

5.1 Azimuth angles of the SkL at different electric field. Positive(negative) angle corresponds to clockwise(counterclockwise) direction. . . . .	63
---	----



# 1 Introduction

Magnetic skyrmions have been attracting massive attention since initially discovered in 2009[2]. Abundant interesting properties have been discovered in this topological magnetic texture[3] including 2D lattice formed by skyrmion quasi-particles[2, 4], topological Hall effect[5, 6], electric field[7] and current controlling[8, 9]. Besides the significance in fundamental physics, it is also considered as one of the most promising candidates as the building block for the next generation spintronics[10]. In the following, a brief introduction will be given so that a basic framework can be established to get into my specific work.

## 1.1 Magnetic skyrmions

Skyrmions, named after T. H. R. Skyrme who introduced this conception for the first time in 1962[11], were topological soliton solution describing mesons and baryons in particle physics. Its analog in condensed matter physics was first proposed in 1989[12] and then intensively studied, mainly theoretically, as a unique excitation in quantum Hall systems[13, 14]. At that time, many unique properties of skyrmions were proposed as quasi-particles. However, the experimental discovery of skyrmions had not been achieved until a few years ago.

Magnetic skyrmions are topological chiral whirl-like spin configurations, as shown in Fig. 1.1. By "topological", it means that a skyrmion cannot be formed by continuously changing the spin configuration from any other spin configurations, neither vice versa. Thus the topological protection makes skyrmions rather stable.

Until now, skyrmions have been found to exist in many different materials, but the most important common feature for all of them is the combination of a parallel (or antiparallel) spin-spin interaction and a non-parallel one. Both interactions originate actually from the Coulomb repulsive interactions among electrons in combination with the Pauli exclusion

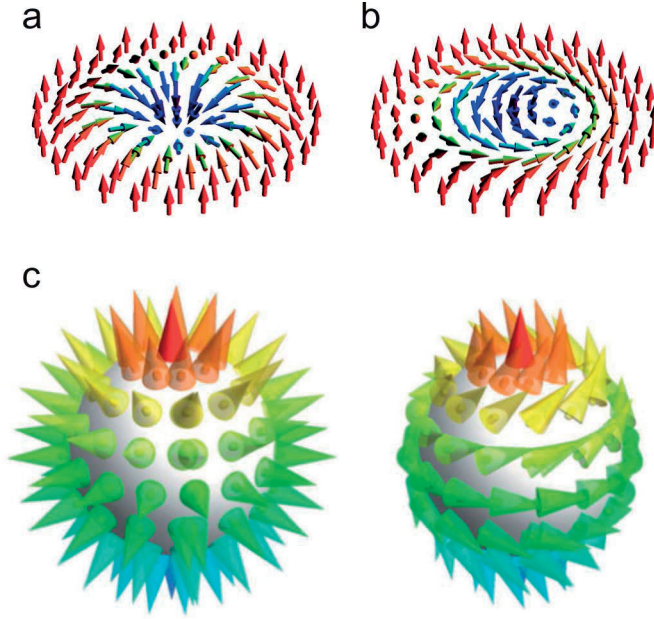


Figure 1.1 – **a.** and **b.** Spin configurations of a Néel and a Bloch type skyrmion respectively. The image is reproduced from Ref. [15]. **c.** Corresponding topological equivalences of the two types of skyrmions mapping the spins onto the surface of a sphere. The image is reproduced from Ref. [16].

principle for fermions. The former interaction, the Heisenberg interaction, has the form:

$$H_{\text{Heisenberg}} = -J_{12} \mathbf{S}_1 \cdot \mathbf{S}_2 \quad (1.1)$$

while the latter one, firstly phenomenologically introduced by Dzyaloshinskii[17] then generalized by Moriya[18] via involving spin-orbital coupling (SOC) into anisotropic super-exchange interaction (thus called the Dzyaloshinskii-Moriya interaction, or briefly the DM interaction), has the form:

$$H_{\text{DM}} = \mathbf{D}_{12} \cdot \mathbf{S}_1 \times \mathbf{S}_2 \quad (1.2)$$

It is obvious to see that  $H_{\text{Heisenberg}}$  makes spins to be locally either parallel or anti-parallel, while  $H_{\text{DM}}$  alone would make spins perpendicular to each other.

Unlike the Heisenberg interaction  $H_{\text{Heisenberg}}$  being a general interaction once there are unpaired electrons, the DM interaction  $H_{\text{DM}}$ , on the other hand, depends heavily on the symmetry of the lattice on which the on-site spins locate. For example, if there is a center of inversion,

then  $\mathbf{D}_{12} = 0$ , resulting in no DM interaction.

There are until now two types of skyrmion hosting materials, the ferromagnet-heavy metal (so that there is strong SOC) interfacial systems and the single crystal bulk systems. In the former system, the large SOC of the heavy metal atoms induces DM interaction between the interfacial ferromagnetic spins as shown in Fig. 1.2, resulting in a skyrmion groundstate[10]. Here, interfaces are necessary in breaking the inversion symmetry so that the DM interactions can survive.

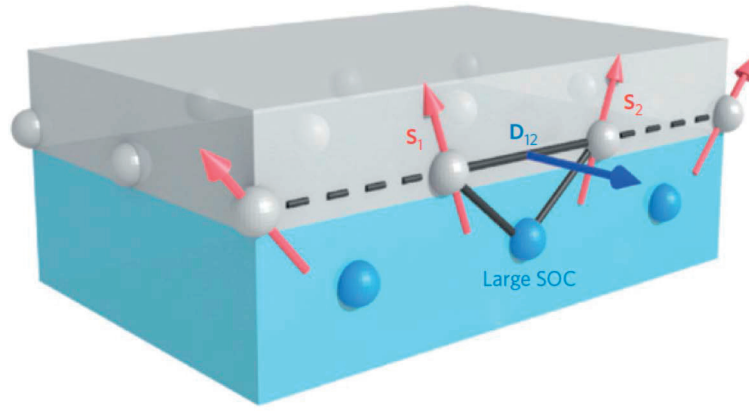


Figure 1.2 – Illustration of DM interactions among spins in a ferromagnet-heavy metal interface. The image is reproduced from Ref. [10].

Skyrmions are also found in crystals without inversion symmetry. For example, the first reported skyrmion system is a B20 compound MnSi[2], with the chiral space group  $P2_13$ . Other materials in this family were discovered shortly after, including metallic  $\text{Fe}_{1-x}\text{Co}_x\text{Si}$ [4], FeGe[19] and insulating  $\text{Cu}_2\text{OSeO}_3$ [20, 21]. Beyond chiral cubic space group  $P2_13$ , GaV<sub>4</sub>S<sub>8</sub>, a semiconductor with non-chiral but polar rhombohedral structure (space group  $C_{3v}$ ) was also reported to host skyrmions[15]. Very recently, the  $\beta$ -Mn-type alloy Co-Zn-Mn system with another chiral cubic space group,  $P4_132$  (or equivalently  $P4_332$  depending on the handedness), was reported to exhibit skyrmion phase in room temperature[22].

## 1.2 Some properties of skyrmions

Upon intensive investigation, skyrmions are found to exhibit abundant unique properties, a large variety of which can be accounted by its non-trivial topology.

### 1.2.1 Topology

The skyrmion winding number is widely used to characterize the topology of skyrmions. It is defined as[23, 24]:

$$\Phi_{\text{skyrmion}} = \frac{1}{4\pi} \int dx dy \mathbf{n} \cdot \left( \frac{\partial \mathbf{n}}{\partial x} \times \frac{\partial \mathbf{n}}{\partial y} \right) \quad (1.3)$$

where  $\mathbf{r}(x, y)$  is the coordinates on the plane perpendicular to the magnetic field  $\mathbf{B}$  and  $\mathbf{n}(\mathbf{r}) = \mathbf{M}(\mathbf{r})/|\mathbf{M}(\mathbf{r})|$  is the local orientation of magnetization. The integration results in 1 for a single skyrmion (or -1 for an anti-skyrmion, which connects to a skyrmion with time reversal symmetry). The skyrmion number actually characterizes how many turns the spins wind around the unit sphere, as illustrated in Fig. 1.1c.

Mathematically, the skyrmion winding number defined above is one of those winding numbers distinguishing different topological classes, or "homotopy groups". For example, vortices are another topologically non-trivial defects that can be seen in type II superconductors but have a different definition of their winding numbers[24]. The main difference between skyrmions and vortices is the former have the order parameter asymptotically goes to constant while that of the latter becomes singular at the core.

Fig. 1.1a and b show respectively the Néel type and the Bloch type skyrmions. This classification originates from the Néel and the Bloch domain walls, with the spiral vectors parallel and perpendicular to the norm vector of the domain wall respectively.

### 1.2.2 Topological Hall effect

It is reported that the Hall effect of MnSi within the skyrmion phase can be expressed as[25]:

$$\rho_{yx} = \rho_{yx}^N + \rho_{yx}^A + \rho_{yx}^T \quad (1.4)$$

where  $\rho_{yx}$  is the totally Hall resistivity,  $\rho_{yx}^N = R_{H0}B$  is the normal Hall effect (NHE) originating from the gyration of conducting electrons under the Lorentz force in the presence of external magnetic field.  $\rho_{yx}^A = \alpha M \rho_{xx0} + \beta M \rho_{xx0}^2 + b M \rho_{xx}^2$  is the anomalous Hall effect (AHE) for ferromagnets and depends on the magnetization  $M$ , resistivity  $\rho_{xx}$  and residual resistivity  $\rho_{xx0}$  of the sample. The last term is the topological Hall effect (THE):

$$\rho_{yx}^T \approx P R_{H0} B_{\text{eff}}^z \quad (1.5)$$



Here,  $P$  is a factor proportional to the spin polarization of charge carriers,  $R_{H0}$  is the normal Hall effect coefficient and  $B_{\text{eff}}^z$  is an emergent effective magnetic field.

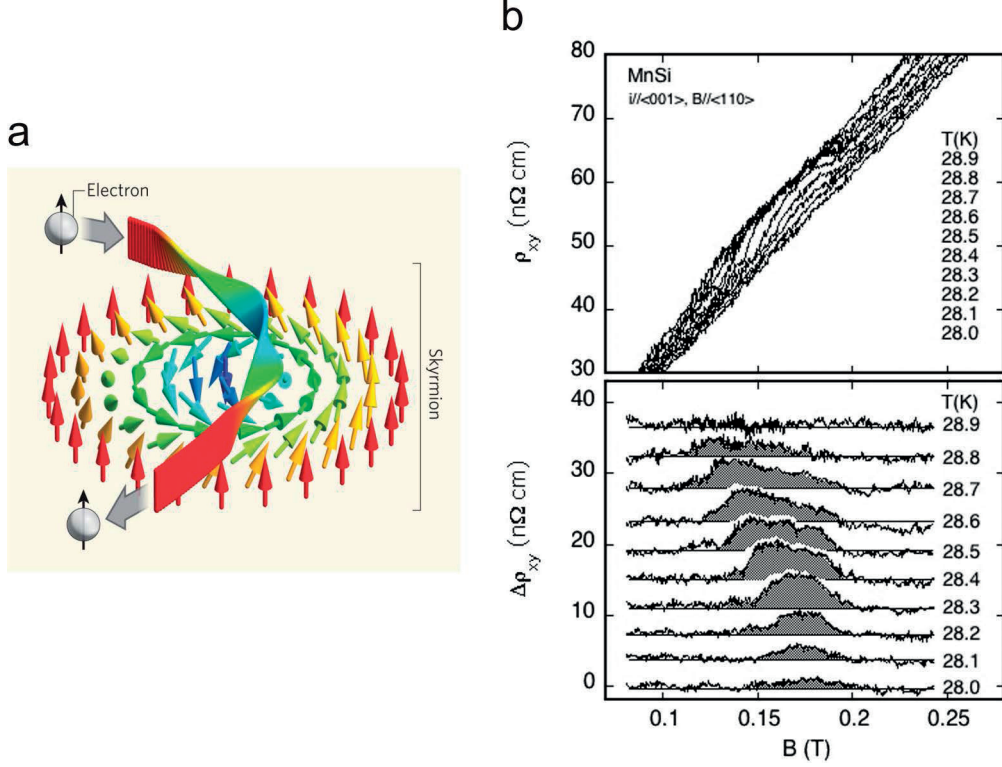


Figure 1.3 – **a.** Illustration of the Berry phase gained by a conduction electron passing through a skyrmion. The figure is reproduced from Ref. [26]. **b.** Upper panel: total Hall resistivity of MnSi in the skyrmion phase, lower panel: pure THE after subtracting NHE and AHE. The figure is reproduced from Ref. [6].

When conduction electrons flow through a slowly varying and topologically non-trivial spin texture, they will remain in the original state but with an additional Berry phase[3],  $\psi = \psi_0 e^{-i\theta}$ , as illustrated in Fig. 1.3a. Similar to the result of the magnetic vector potential in the Aharonov - Bohm effect, the collected Berry phase  $\theta$  can be viewed as arising from a magnetic vector potential and hence from an emergent effective magnetic field  $\mathbf{B}_{\text{eff}}$ . It has been demonstrated that this emergent magnetic field depends on the skyrmion density[6]:

$$B_{\text{eff}}^i = \frac{\Phi_0}{8\pi} \epsilon_{ijk} \mathbf{n} \cdot (\partial_j \mathbf{n} \times \partial_k \mathbf{n}) \quad (1.6)$$

where  $\Phi_0 = h/e$  is the flux quantum and  $\epsilon_{ijk}$  is the antisymmetric unit tensor.

Experimentally, by combining the measurement results of magnetization, resistivity and Hall effect in the skyrmion phase, the THE can be extracted. Fig. 1.3b shows such an example for a typical metallic skyrmion material MnSi[6].

### 1.2.3 External control

In addition to the THE, another consequence of the unique topology of skyrmions is that the emergent effective magnetic field gives rise to a spin transfer torque (STT), which is much more effective than for magnetic domain walls in ferromagnets. STT is the coupling between an applied electric current and the magnetic structure, and it originates from the extra spin currents when driving electric current through magnets that have vortex-like spin structures, such as magnetic domain walls, vortices in type 2 superconductors and skyrmions. Magnus force will arise due to the enhancement of spin current on one side of the vortices and reduction on the other side, resulting in a net torque. Various analytical[27, 8, 28, 29] and numerical[30, 31] calculations predicted that the STT can be utilized to manipulate the motion of skyrmions. Fig. 1.4 is a schematic illustration for the principle of STT induced skyrmion motion[3].

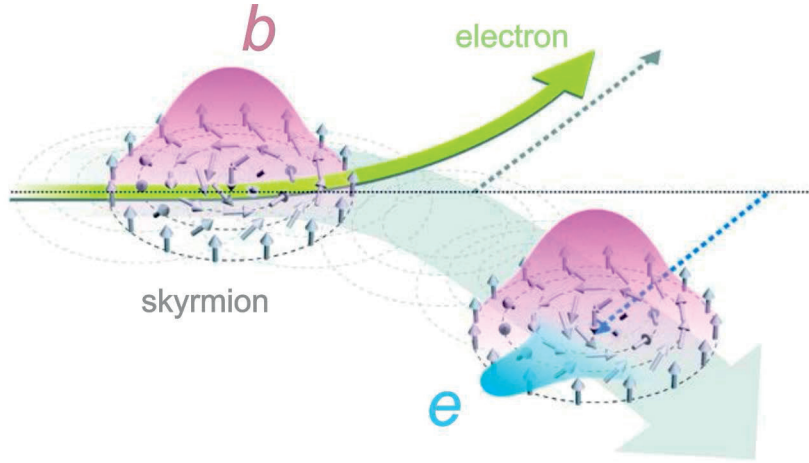


Figure 1.4 – Illustration of interactions of conduction electrons and skyrmions. The emergent electromagnetic fields of skyrmions (labelled as  $b$  for the emergent effective magnetic field and  $e$  for the emergent effective electric field) induces the STT. The image is reproduced from Ref. [3].

Electric current driving motions were observed in both bulk skyrmion lattice systems and interfacial skyrmion systems. Reciprocal space neutron scattering study showed that in the B20 compound MnSi, the combination of a temperature or field gradient and an electric current can lead to a rotation of the skyrmion lattice[32]. Magnetic domain walls can also be driven by electric currents, however, the threshold current density needed for rotating the skyrmion lattice is 5 or 6 orders of magnitude smaller than that needed for magnetic domain walls. Real space Lorentz microscopy experiments demonstrated both rotational and translational motion of skyrmion lattice in FeGe thin plate again with very low current density [33]. In contrast, electric current induced STT was observed to drive individual skyrmions motion in an interfacial system[9]. A very effective coupling of the electric current to the magnetic structure due to the topology induced Berry phase and weak pinning forces due to smooth magnetic structures are proposed as two main reasons to explain the ultra-low current

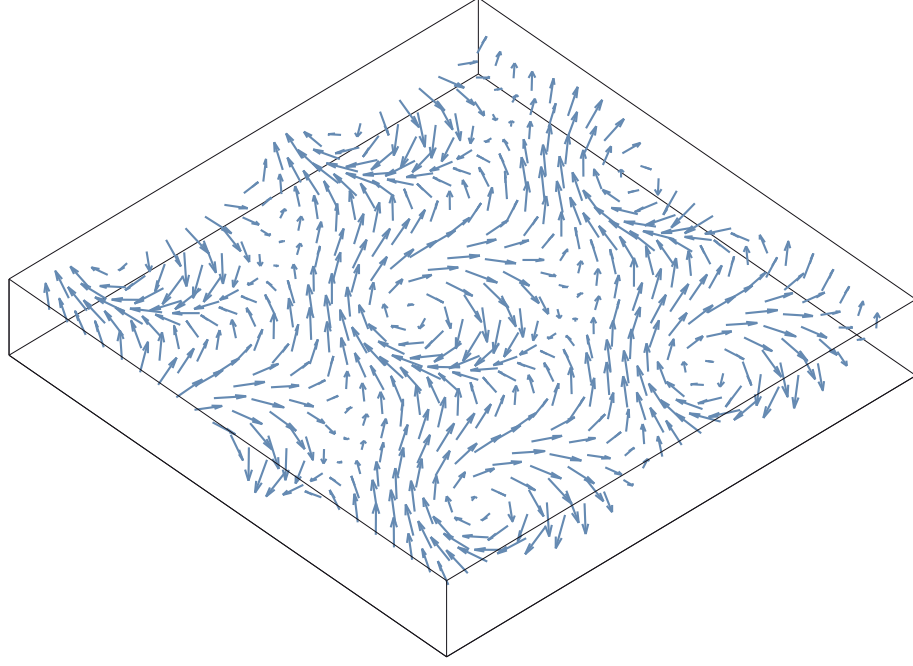


Figure 1.5 – Illustration of the Spin configuration of a simulated skyrmion lattice.

density needed for moving skyrmions, compared to that needed for magnetic domain walls.

### 1.3 Skyrmion lattice

There are two main differences between the interfacial skyrmions and the bulk skyrmions. First, interfacial skyrmions are all Néel type while bulk skyrmions are mostly Bloch type (except in  $\text{GaV}_4\text{S}_8$  in which the skyrmions are Néel type). Second, skyrmions in interfacial systems usually exist individually or form small clusters, with vanishing correlations, in contrast, the equilibrium skyrmion state of bulk systems is a triangular lattice that can extend across the whole sample, with long range translational and orientational correlations. My work focused on the bulk skyrmion system  $\text{Cu}_2\text{OSeO}_3$ , thus a brief introduction on the skyrmion lattice state will be given in the following.

#### 1.3.1 Spin configuration of skyrmion lattices

Mathematically, the skyrmion lattice state can be viewed as the vector sum of three spin helices with the propagation wavevectors in the same plane and forming  $120^\circ$  with each other:

$$\mathbf{S} = \mathbf{S}_0 + \sum_{i=1}^3 \mathbf{S}_i e^{i\mathbf{k}_i \cdot \mathbf{r}} + \mathbf{S}_i^* e^{-i\mathbf{k}_i \cdot \mathbf{r}} \quad (1.7)$$

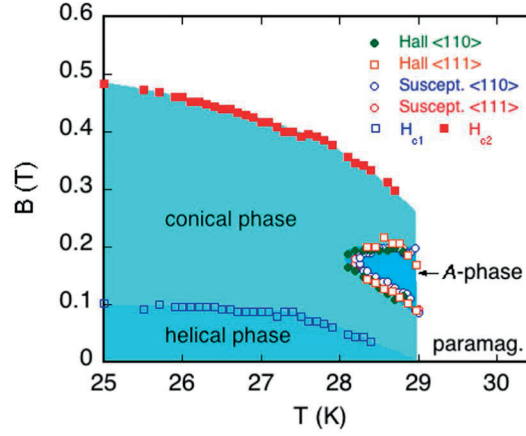


Figure 1.6 – Phase diagram of MnSi obtained by Hall effect measurements. The figure is reproduced from Ref. [6].

The resulting spin configuration of this equation is a two dimensional triangular lattice and each lattice point is a topologically non-trivial Bloch type skyrmion with the skyrmion number -1, as shown in Fig. 1.5.

### 1.3.2 Properties of skyrmion lattices

Although discovered for a long time, a very small pocket in the temperature-magnetic phase diagram of MnSi[6], shown in Fig. 1.6, had been called the A phase before being confirmed as the SkL phase in 2009 by neutron scattering. This phase is surrounded by a so-called conical phase with the single propagation vector of the spin spiral along the direction of the applied magnetic field, such that at little energy cost a homogeneous spin component can develop along the magnetic field. Conventional mean field calculations showed that in the temperature and field range of the SkL phase, its free energy is very close to but always higher than that of the conical phase, in other words, the SkL phase is unlikely to appear. To solve this paradox, A. Rosch with co-workers[2] introduced Gaussian thermal fluctuation term into the conventional Ginzburg-Landau free energy. This small correction leads to the stabilization of the SkL phase.

This shows that the formation of the SkL phase is a typical "order by disorder" mechanism. That is, for (nearly) degenerated states, fluctuations, either thermal or quantum, will pick out the state with higher entropy due to the relation  $F = U - TS$ .

Besides the equilibrium SkL phase, there are also meta-stable SkL states existing in many skyrmion hosts. H. Oike and co-workers[34] gave a pulse of high current density to MnSi in the conical phase so that it was rapidly heated and got into the SkL phase, then the sample was quenched back to the original temperature. They found that skyrmions still existed, as evidenced by the appearance of THE signals. K. Karube *et al.*[35] observed similar phenomenon in  $\text{Co}_8\text{Zn}_8\text{Mn}_4$  by cooling down the sample with magnetic field through the equilibrium SkL phase. These non-equilibrium SkL states are quite robust, which is thought of as a demonstra-

tion of topological protection.

The thermal history can also affect the orientation of the SkL in  $\text{Cu}_2\text{OSeO}_3$ , as reported by K. Makino and colleagues[36], there was a  $30^\circ$  difference of the orientations of the SkL in  $\text{Cu}_2\text{OSeO}_3$  between field cooling from the paramagnetic phase and field warming from the conical phase.

Moreover, external excitations were reported to efficiently alter the SkL phase. In an ac magnetic susceptibility investigation, I. Levatić *et al.*[37] found a dramatic enlargement of the SkL phase in the phase diagram by applying hydrostatic pressure to a single crystal  $\text{Cu}_2\text{OSeO}_3$  sample. Y. Okamura and co-workers[38] reported that the application of electric field along [111] direction of  $\text{Cu}_2\text{OSeO}_3$  can result in the transition from and to the SkL phase, depending on the direction of the electric field.

As already mentioned above, the SkL in metallic materials, *e.g.* MnSi, can be rotated by a combination of a thermal gradient and an electric current, due to the emergent electromagnetic fields. The SkL in the insulating compound,  $\text{Cu}_2\text{OSeO}_3$ , can also be rotated by the application of an electric field, however, through a totally different mechanism, the magnetoelectric coupling. My contribution to this topic can be found in Chapter 2. Note that it does not mean that the emergent electromagnetic fields will mute in insulating SkL. For example, X. Yu *et al.*[39] reported the rotation of the SkL in thin plate  $\text{Cu}_2\text{OSeO}_3$  induced by electron beam radiation, which they explained by the rotational flow of magnons driven by the emergent electromagnetic fields.

## 1.4 Content of the thesis

During my 4-year Ph.D. work, I have been systematically investigating the thermodynamical and dynamical properties of skyrmions, especially the properties of the SkL, in the magnetoelectric coupling skyrmion host compound  $\text{Cu}_2\text{OSeO}_3$ . The results, analysis and discussions of which will all be included in this thesis.

In Chapter 2, comprehensive measurements on bulk samples, including the dc magnetization, our in-house developed magnetoelectric susceptibility as well as small angle neutron scattering with the application of electric field, will be presented.

Experimental results obtained by Lorentz transmission electron microscopy (LTEM), the main technique used in my work, will be presented in three chapters. Chapter 3 focuses on the general static observations of the helical and the SkL phase in  $\text{Cu}_2\text{OSeO}_3$ . Chapter 4 demonstrates a KTHNY (Kosterlitz, Thouless, Halperin, Nelson, and Young) type of melting of SkL induced by magnetic field via real space observation and quantitative analysis. And Chapter 5 contains the real space and real time investigations of the emergent phenomena in the presence of electric field (E-field), including E-field induced rotation and E-field creation/annihilation of skyrmions.

## Chapter 1 Introduction

---

Summaries and outlooks will be given in chapter 6. The conclusions emphasize the dynamics of the SkL investigated in the present work and perspectives based on this are made in both the fundamental and applying aspects.

Also included are two appendices. App. A summarizes the main image processing techniques used in my work and App. B gives detailed description on the skyrmion identification in various conditions, which is the basis of a majority of work in this thesis.

Note that the specific theoretical background and experimental techniques for the content of each chapter will be put at the beginning of the corresponding chapter, rather than compacting them all in a separate chapter. I hope this will make the reading smoother and more natural.

## 2 Properties of bulk single crystal $\text{Cu}_2\text{OSeO}_3$

In this chapter, focus will be given to the magnetic and magnetoelectric properties of bulk  $\text{Cu}_2\text{OSeO}_3$ , which are the basis for the further studies on its SkL. After a brief introduction on the theoretical model for  $\text{Cu}_2\text{OSeO}_3$ , experimental results of magnetization, magnetoelectric susceptibility and neutron scattering will be shown and discussed in detail.

### 2.1 Basic model for $\text{Cu}_2\text{OSeO}_3$

Having a chiral lattice structure[40] belonging to the same  $P2_13$  space group, as shown in Fig. 2.1,  $\text{Cu}_2\text{OSeO}_3$  share some common properties with B20 alloys such as MnSi and FeGe, which are also skyrmion hosts. The lack of the inversion symmetry of space group ensures the existence of the DM interactions in the system.

There are two type of  $\text{Cu}^{2+}$  sites in the unit cell, surrounded by  $\text{O}^{2-}$  tetrahedra (Cu1) and bi-pyramid (Cu2) respectively. The ratio between the number of the two type of  $\text{Cu}^{2+}$  sites is  $\text{Cu1} : \text{Cu2} = 3 : 1$ . In the magnetically polarized state, spins on the Cu1 sites will be parallel with the magnetic field while those on the Cu2 site will be anti-parallel, forming a 3-up-1-down spin configuration[40].

However, in sharp contrast to B20 alloys being metallic,  $\text{Cu}_2\text{OSeO}_3$  is insulating with unique magnetoelectric coupling due to strong spin-orbital coupling. A basic theoretical description will be given below in these two aspects.

#### 2.1.1 Magnetic interactions and phases

The basic magnetic interaction of  $\text{Cu}_2\text{OSeO}_3$ , can be described by the following Hamiltonian:

$$H = - \sum_{\langle i,j \rangle} J_{ij} \mathbf{S}_i \cdot \mathbf{S}_j + \sum_{\langle i,j \rangle} \mathbf{D}_{ij} \cdot (\mathbf{S}_i \times \mathbf{S}_j) - \mathbf{B} \cdot \sum_i \mathbf{S}_i \quad (2.1)$$



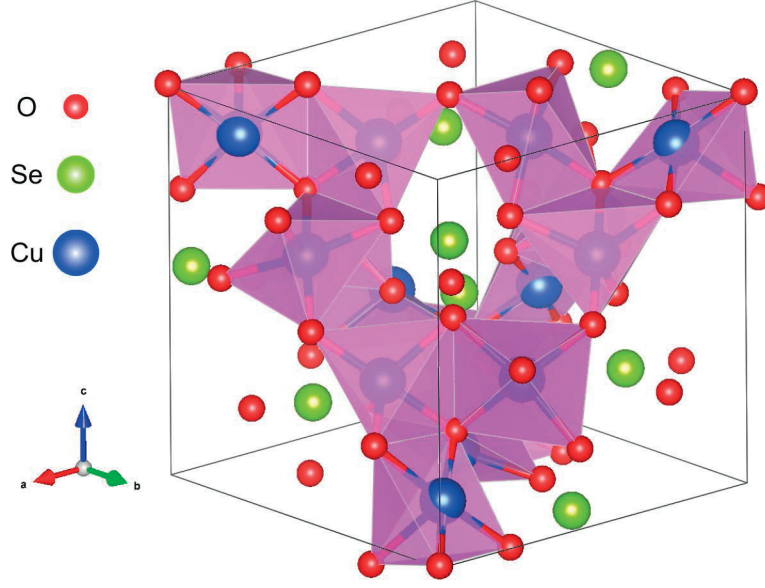


Figure 2.1 – Crystal structure of  $\text{Cu}_2\text{OSeO}_3$ .  $\text{O}^{2-}$  tetrahedra and bi-pyramid are indicated.

The first term is the conventional collinear ferromagnetic Heisenberg exchange interaction, the second term is the noncollinear Dzyaloshinskii-Moriya interaction and the last term is the Zeeman term.

When discussing magnetic order with long period modulation, the free energy of this Hamiltonian can be written in a continuum form using the Landau-Lifshitz approach[41]:

$$F(\mathbf{S}) = \int d^3\mathbf{r} f(\mathbf{S})$$

$$f(\mathbf{S}) = \frac{1}{2}A(S_x^2 + S_y^2 + S_z^2) + \frac{1}{2}J[(\nabla S_x)^2 + (\nabla S_y)^2 + (\nabla S_z)^2] + D\mathbf{S} \cdot (\nabla \times \mathbf{S}) - \mathbf{B} \cdot \mathbf{S} \quad (2.2)$$

here,  $\mathbf{S} = \mathbf{S}(\mathbf{r})$  is the spin density,  $A$  term was introduced to penalize the disuniformity in the cubic symmetry to the first order[42] and the magnetic field is defined along the  $z$ -axis.

Eq. 2.2 is a restriction from all possible spin configurations. It is possible to describe the helical, conical and skyrmion spin configurations by considering the system to have  $N$  periodic spin helices, then the general form of the spin configuration is given by[41]:

$$\mathbf{S} = \mathbf{S}_0 + \sum_{i=1}^N \mathbf{S}_i e^{i\mathbf{k}_i \cdot \mathbf{r}} + \mathbf{S}_i^* e^{-i\mathbf{k}_i \cdot \mathbf{r}} \quad (2.3)$$



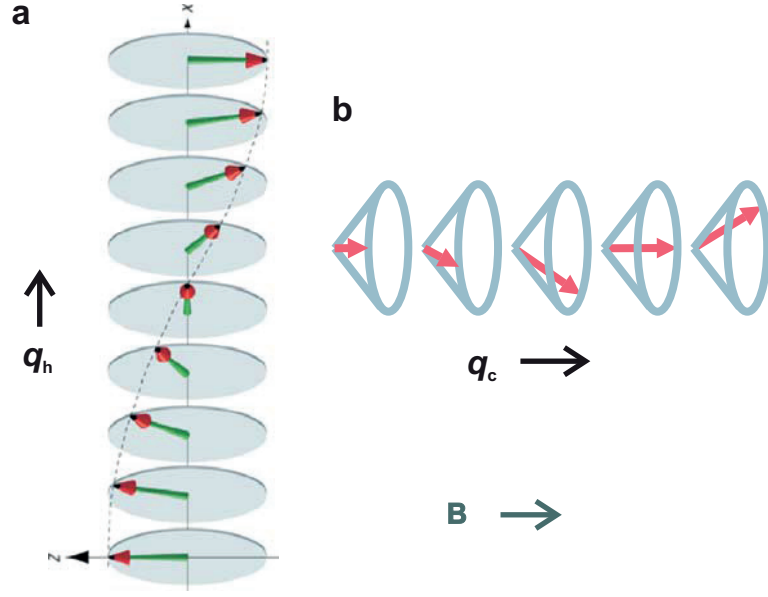


Figure 2.2 – Spin configurations of **a.** helical and **b.** conical phases respectively. Note that in helical spin configuration the wave vector is perpendicular to the magnetic field while in the conical parallel.

If defining  $\mathbf{S}_i \cdot \mathbf{S}_i^* = \frac{1}{2} S_H^2$ , then one can use

$$S_0^2 + NS_H^2 = 1 \quad (2.4)$$

as the normalization condition. So here spins are treated classically, *i.e.* treated as a continuous vector field.

Insert Eq. 2.3 into Eq. 2.2, the energy then has the form:

$$E = \frac{1}{2} NS_n^2 (Jk^2 - 2Dk) - BS_0 \quad (2.5)$$

The  $A$  term is dropped here due to the normalization condition Eq. 2.4 averages the spin configuration so that the disuniformity can be negligible in practice.

This energy can be minimized at  $k = D/J$ , regardless of the direction of propagation vector or the number of the spin helices. Thus it shows clearly that the system has a ground state of spiral magnetic structure, with the modulation wave number  $k = D/J$ , *i.e.* the period of the helicity is solely determined by the ratio between the two types of magnetic interactions.

If introducing anisotropic terms up to the fourth order, as firstly done by Bak and Jensen[43],

the free energy will be expressed as:

$$f(\mathbf{S}) = \frac{1}{2}A(S_x^2 + S_y^2 + S_z^2) + \frac{1}{2}J[(\nabla S_x)^2 + (\nabla S_y)^2 + (\nabla S_z)^2] + D\mathbf{S} \cdot (\nabla \times \mathbf{S}) - \mathbf{B} \cdot \mathbf{S} \\ + \frac{1}{2}C_1 \left[ \left( \frac{\partial S_x}{\partial x} \right)^2 + \left( \frac{\partial S_y}{\partial y} \right)^2 + \left( \frac{\partial S_z}{\partial z} \right)^2 \right] + C_2(S_x^2 + S_y^2 + S_z^2)^2 + C_3(S_x^4 + S_y^4 + S_z^4) \quad (2.6)$$

Now one can further distinguish various spin configurations with different directions of the wave vector  $\mathbf{k}$  and different numbers of spin helices[41]. For example, the groundstate of bulk  $\text{Cu}_2\text{OSeO}_3$  is a single-spiral spin configuration with the propagation vector along  $\mathbf{k} \parallel \{100\}$ , while for  $\text{MnSi}$ ,  $\mathbf{k} \parallel \{111\}$ . So both groundstates are multiple helical domains propagating in symmetry associated directions.

As the magnetic field increases, the system will experience a phase transition from the helical groundstate to the so-called conical phase, another spiral spin configuration whose propagation wave vector is parallel to the magnetic field, as illustrated in Fig. 2.2b.

It has been experimentally observed, however, the skyrmion lattice (SkL) phase in a very small pocket in the phase diagram just below the magnetic ordering temperature and magnetic field in the bulk material. As mentioned in Ch. 1, this phase can be viewed as the vector sum of three spin helices with the propagation vectors form  $120^\circ$  with each other, as shown in Fig. 1.5.

In contrary, there is no conical phase in thin slab samples due to magnetic dipole interactions[44, 45, 46], but the SkL phase extends to the base temperature and to as high as the magnetic field for the ferrimagnetic phase transition.

As a summary, the general phase diagram of  $\text{Cu}_2\text{OSeO}_3$  is shown in Fig. 2.3

### 2.1.2 Magnetoelectric coupling

$\text{Cu}_2\text{OSeO}_3$  exhibits a unique magnetoelectric (ME) coupling originating from spin-orbital interaction. Experiments revealed that this ME coupling can be characterized by the  $d$ - $p$  hybridization model[21, 47, 48, 49, 50], that is, the magnetically induced electric polarization is along the Cu-O bonds and its magnitude depends on the projection of the local magnetic moment along the direction of the Cu-O bonds, as the following:

$$\vec{p}_{ij} \propto (\langle \vec{m}_i \rangle \cdot \vec{e}_{ij})^2 \vec{e}_{ij} \quad (2.7)$$

where  $\langle \vec{m}_i \rangle$  is the magnetic moment of a single  $\text{Cu}^{2+}$  ion and  $\vec{e}_{ij}$  is the unit vector along the Cu-O bonds.

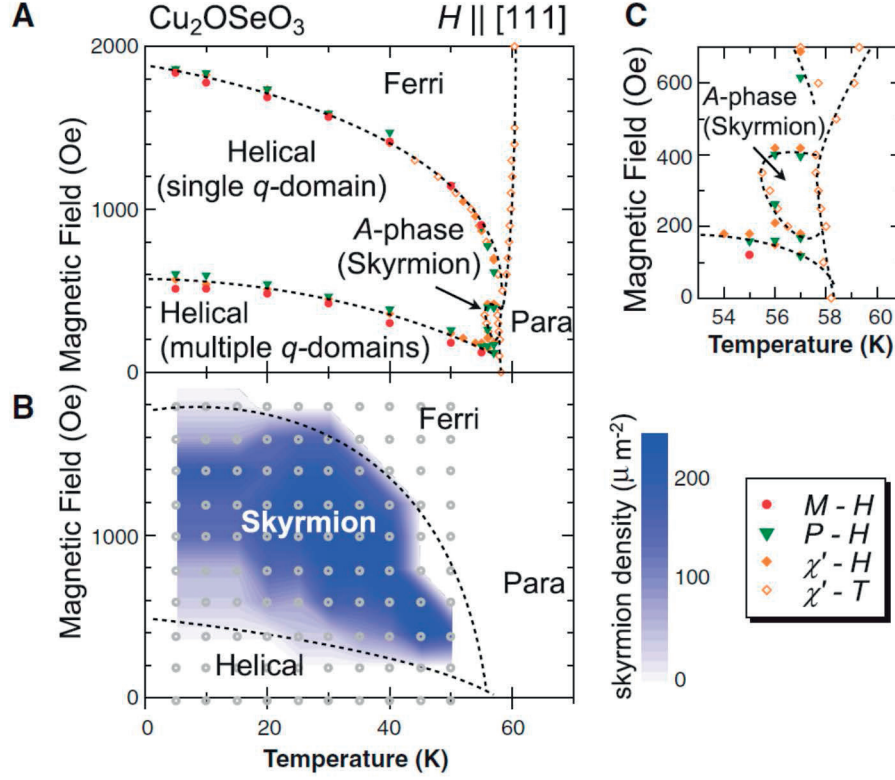


Figure 2.3 – Phase diagrams of bulk and thin film  $\text{Cu}_2\text{OSeO}_3$  respectively. The figure is reproduced from Ref. [20]

Combined with the lattice structure of  $\text{Cu}_2\text{OSeO}_3$ , the polarization of a unit cell is given by[51]:

$$\vec{P} = \lambda(S_y S_z, S_z S_x, S_x S_y) \quad (2.8)$$

where  $\vec{S}$  is the magnetic moment of a whole unit cell.

Inserting the complex magnetic structures described by Eq. 2.3, with  $n = 1$  for the helical and conical phase and  $n = 3$  for the SkL phase, one can then get the macroscopic electric polarization in different phases. Fig. 2.4 shows the local electric polarization distributions of a single skyrmion with the magnetic field along three high symmetry directions of the lattice. When  $\mathbf{B} \parallel [001]$ , there is no electric polarization but electric quadrupoles. When  $\mathbf{B} \parallel [1\bar{1}0]$ , the electric polarization  $\mathbf{P}$  is along  $[00\bar{1}]$ , and for  $\mathbf{B} \parallel [111]$ ,  $\mathbf{P} \parallel [111]$ .

These electric polarization distributions will play a very important role in my research, as can be seen in the following chapters.

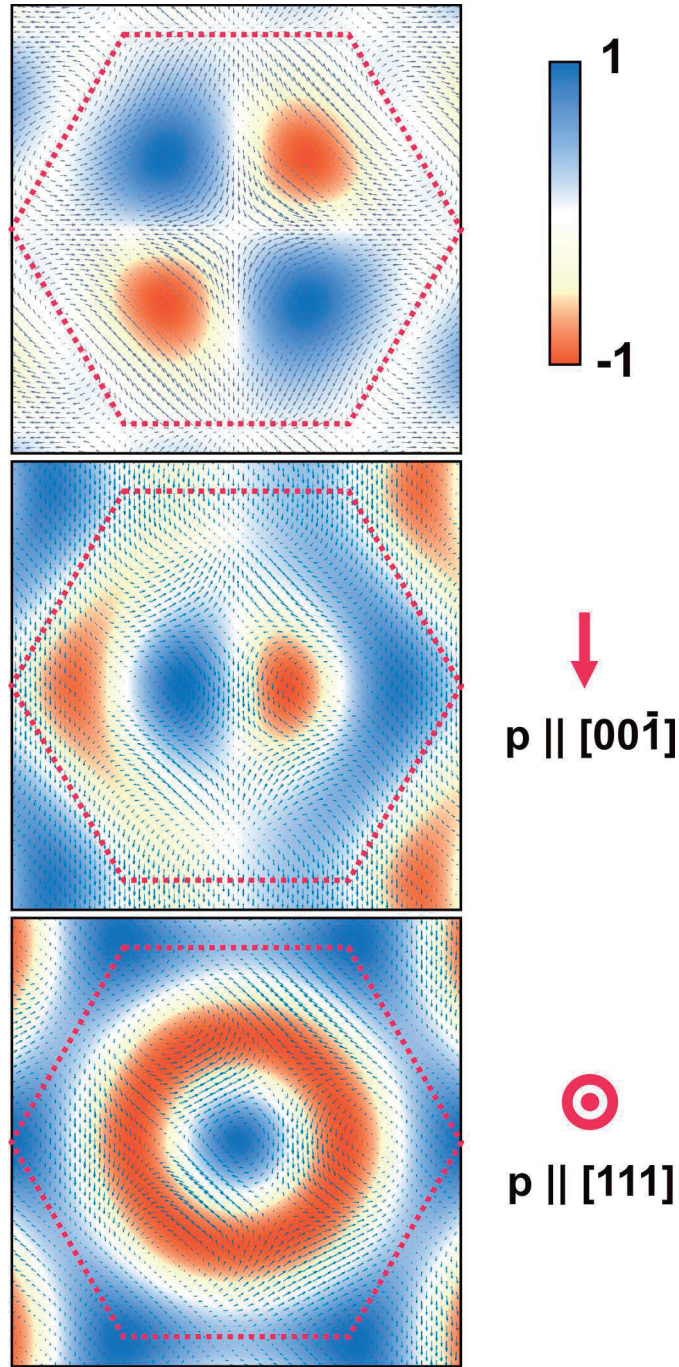


Figure 2.4 – Simulated electric polarization distribution of  $\text{Cu}_2\text{OSeO}_3$  in the SkL phase the magnetic field along **a.**  $[001]$ , **b.**  $[1\bar{1}0]$  and  $[111]$  respectively based on Eq. 2.8. The out of plane components of electric polarizations are normalized respectively with the maximum and minimum value in each case and shown as by color map. The in plane components are shown by arrows representing the vector fields. The dashed line framework in each panel indicates the unit cell of the SkL.

## 2.2 Experimental results and analysis

Very high quality  $\text{Cu}_2\text{OSeO}_3$  single crystals were synthesized by the chemical vapor deposition method. After determining the orientations of a crystal by X-ray Laue diffraction, it was cut according to the need of an experiment so that the externally applied magnetic and/or electric fields can be easily aligned with the desired orientation of the sample. Main experimental results on these samples are given in the following.

### 2.2.1 Magnetic properties

Fig. 2.5a shows the magnetization of  $\text{Cu}_2\text{OSeO}_3$  as a function of temperature under different magnetic fields measured in a zero field cooled (ZFC) process. At high temperature, the measured data exhibit a paramagnetic behavior, obeying the Curie-Weiss Law  $\chi(T) = \frac{C}{T-\theta_w} + \chi_0$ . A phase transition can be observed at around 58K from paramagnetic state to the magnetically ordered state for all the magnetic field applied.

Fig. 2.5b shows the temperature dependent magnetization under magnetic field respectively for the helical phase (5mT) and for the SkL phase (20mT). Here, both ZFC and FC results are shown, and hysteresis can be seen in temperatures well below the ordering temperature.

Fig. 2.6a is the magnetization curve of  $\text{Cu}_2\text{OSeO}_3$  with  $B \parallel [111]$  at 5K. Saturation appears when  $|B| > 1500\text{Oe}$ , and the saturated magnetization is  $0.5\mu_B/\text{Cu}^{2+}$ , perfectly consistent with the 3-up-1-down ferrimagnetic spin configuration composed by spin- $\frac{1}{2}$   $\text{Cu}^{2+}$  ions. Actually, the saturated value of the magnetization around base temperature can be used to identify the quality of the sample. During the field scan the sample underwent two phase transitions, from the helical to the conical phase and from the conical to the polarized phase, which manifest themselves as kinks in the magnetization curve, as labelled by shadowed regions. The insert shows there is only very weak, if not vanishing, magnetic hysteresis.

The magnetization curve measured at 57K is shown in Fig. 2.6b. Although saturation also appears in the curve at field higher than 600Oe, the magnetization value is less than  $0.2\mu_B/\text{Cu}^{2+}$  due to strong thermal fluctuations. Again, one can see small kinks corresponding to various phase transitions, as indicated; however, the transitions look less obvious compared with that in the 5K curve. If one do the ac magnetic susceptibility, or as shown in Fig. 2.5 insert, the differential of the magnetization curve, the transitions become more visible.

### 2.2.2 Magnetoelectric susceptibility

The  $d$ - $p$  hybridization ME coupling gives rise to different configurations of electric polarization distributions in  $\text{Cu}_2\text{OSeO}_3$  in different phases. The conventional polarization as a function of the magnetic field indeed shows different behaviors in different phases, as can be found in Ref. [20, 21]; however, the phase boundaries are still not that sharp and thus it is not so easy to determine the ranges of different phases. ac magnetic susceptibility was also used to

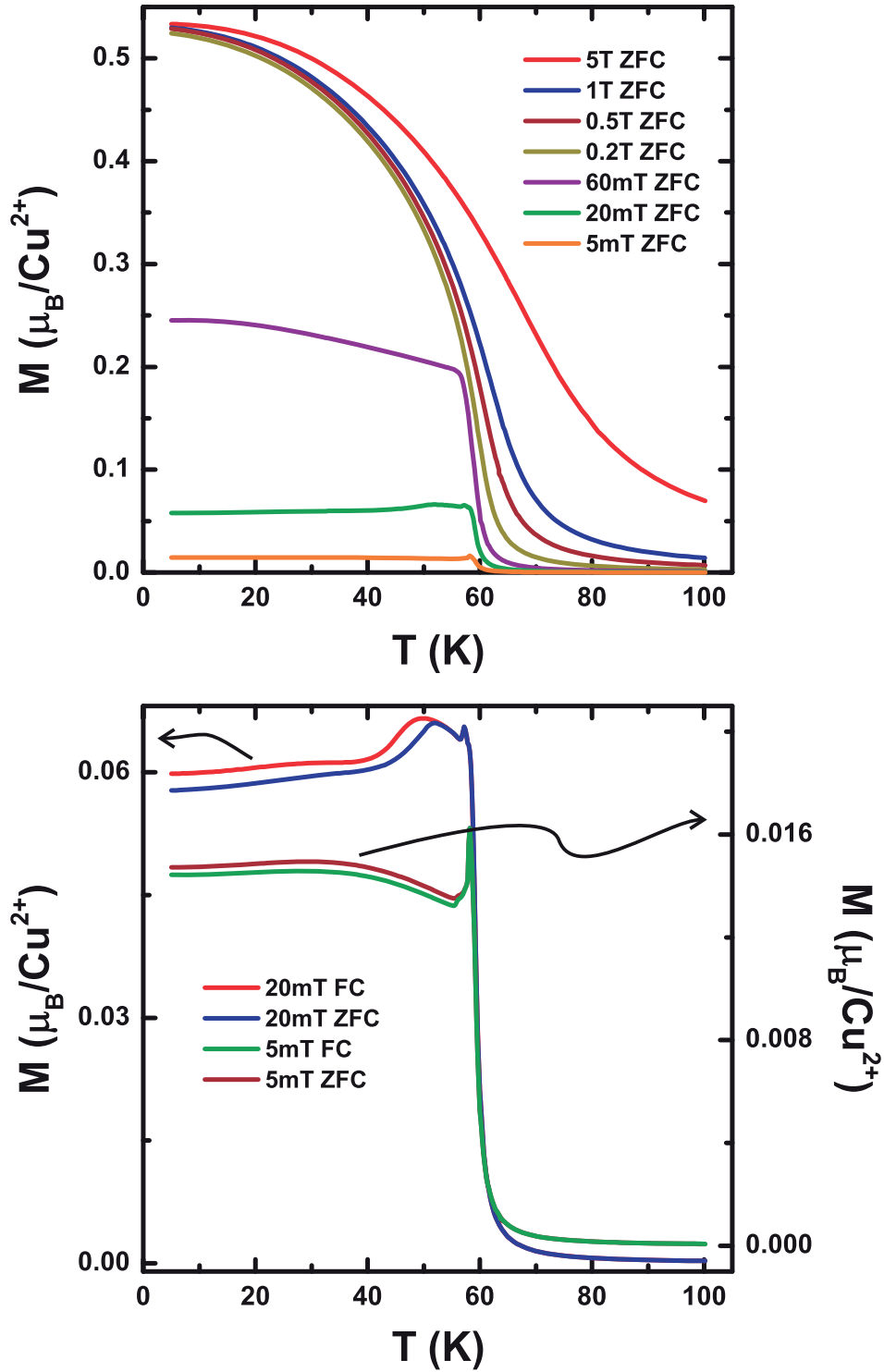


Figure 2.5 – **a.** Magnetization of bulk  $\text{Cu}_2\text{OSeO}_3$  as a function of temperature at different magnetic fields with  $B \parallel [111]$ . All data shown are measured zero field cooled. **b.** Zero field cooled and field cooled measurement of magnetization of  $\text{Cu}_2\text{OSeO}_3$  as a function of temperature in the helical phase and the SkL phase respectively.

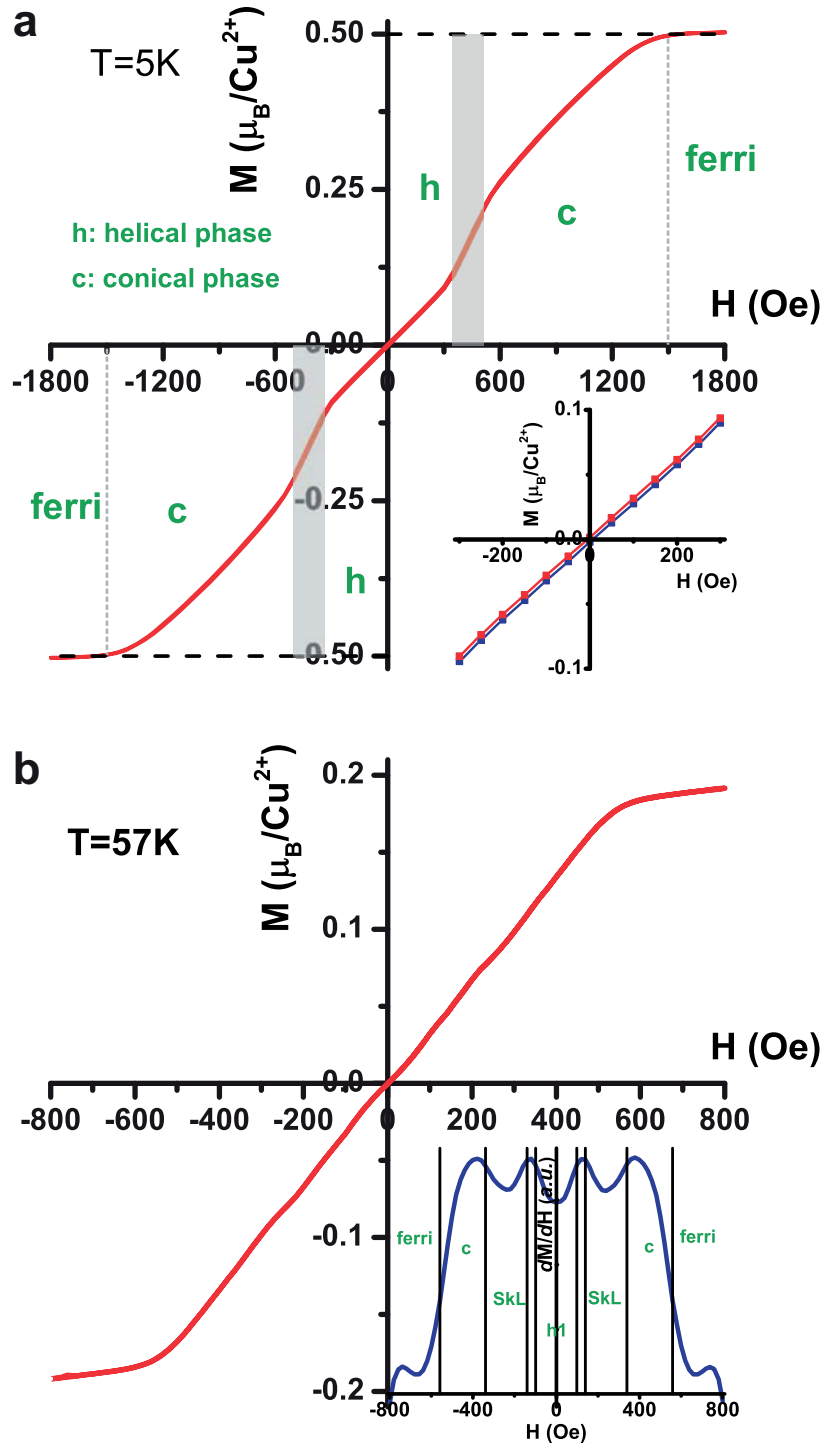


Figure 2.6 – **a.** Magnetization of bulk  $\text{Cu}_2\text{OSeO}_3$  as function of magnetic field at 5K with  $B \parallel [111]$ . Here, the SkL phase cannot be seen and the saturated value of the magnetization is consistent with the 3-up-1-down ferrimagnetic spin configuration. **b.** Magnetization of bulk  $\text{Cu}_2\text{OSeO}_3$  as function of magnetic field at 57K. Several phase transitions among various phases including the SkL phase can be seen. The insert shows the numerical differential, which is comparable with the directly measured ac susceptibility reported in Ref. [20, 21]



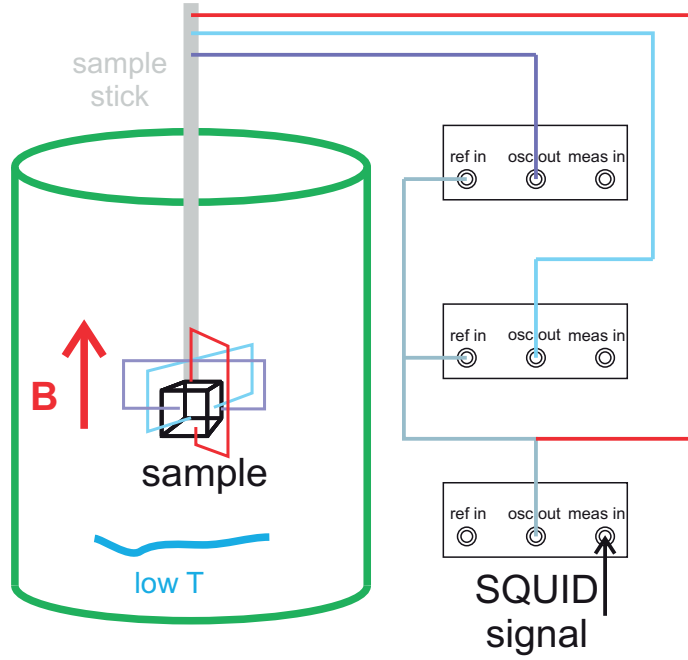


Figure 2.7 – Schematic illustration of the setup for magnetoelectric susceptibility measurement. The final goal will be capable to apply an electric field along any desired direction by three orthogonal components, but data shown here are all measured with only one direction of the electric field.

determine the phase boundaries, yet the results were not ideal either[20].

On the other hand, we found that the ME coupling can be used to perfectly solve this problem by measuring the magnetoelectric susceptibility[52, 53], that is, adjusting the temperature and/or the magnetic field to drive the system into various phases, then measure the ac changes in the magnetization upon an ac electric fields. This technique can thus be called  $dM/dE$ .

Fig. 2.7 shows schematically our  $dM/dE$  setup. Here, we established the instrument based on a conventional SQUID magnetometer in a cryostat. A superconducting magnet provides the dc magnetic field, a lock-in amplifier together with a voltage preamplifier generates the ac electric field, the corresponding ac magnetic moment is sensed by the SQUID and measured by the same lock-in amplifier.

The following Taylor expansion by the ac electric field  $E$  explains why the measurement results are the magnetoelectric susceptibility  $dM/dE$ :

$$M(E_0 \cos(\omega t)) = M(E_{dc} = 0) + \frac{dM}{dE} E_0 \cos(\omega t) + \frac{1}{2} \frac{d^2 M}{dE^2} E_0^2 \cos^2(\omega t) + \dots \quad (2.9)$$

However, since what we directly measure is the analog output of the SQUID sensor, the raw



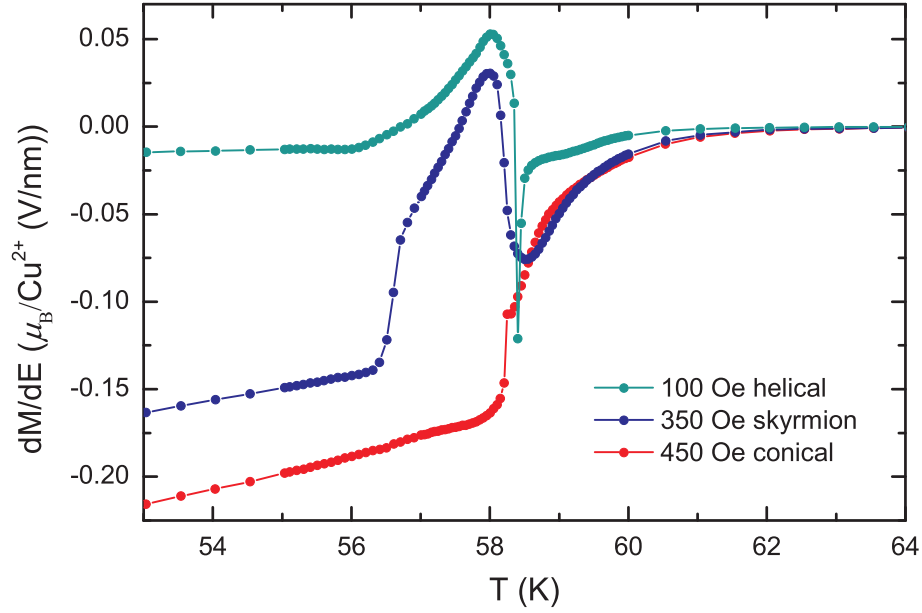


Figure 2.8 –  $dM/dE$  real part as a function of temperature in different phases.

data is in the unit of voltage, and thus the convert of the raw data from voltage to magnetic moment then needs a calibration process.

A standard YIG sample for the magnetic moment is used for this purpose. Firstly, it was measured by the SQUID at the most suitable sensitivity range, getting the raw SQUID voltages as a function of the sample position in this range. Then taking the highest (or symmetrically lowest) sample position as the reference point, the voltage differences can be obtained for all positions. Thus a universal relation between the SQUID voltage and the sample position can be established for a known value of magnetic moment (just in one range, but the similar relations can be obtained based on the SQUID parameters). Moreover, in the SQUID dynamical range, the SQUID voltage is proportional to the magnetic moment. Thus the relation between the magnetic moment and the SQUID voltage difference is known. In practice, in a  $dM/dE$  measurement, the sample will always be fixed in the center of the SQUID pick-up coil to achieve maximum signal. The measured amplitude of the voltage oscillation can then be converted to the value of magnetic moment, and then further getting  $dM/dE$ . Specifically for the system I used, one has 1V of SQUID voltage corresponds to  $2.344 \times 10^{-4}$  emu.

Fig. 2.8 shows the temperature dependence of the real part of the  $dM/dE$  measured in the  $\mathbf{B}||[111]$  and  $\mathbf{E}||[111]$  configuration. One can see that in the paramagnetic phase sufficiently above the phase transition, there is no  $dM/dE$  signal. The onset of the  $dM/dE$  signal appears at around 62K, a temperature slightly higher than the magnetically ordered temperature, 58.5K. After a critical behavior[54] approaching the phase transition, different anomalies occur when entering different magnetically ordered states. For the helical phase, there is a very sharp peak then followed by a broad bump decaying to almost constant small signal. For the skyrmion

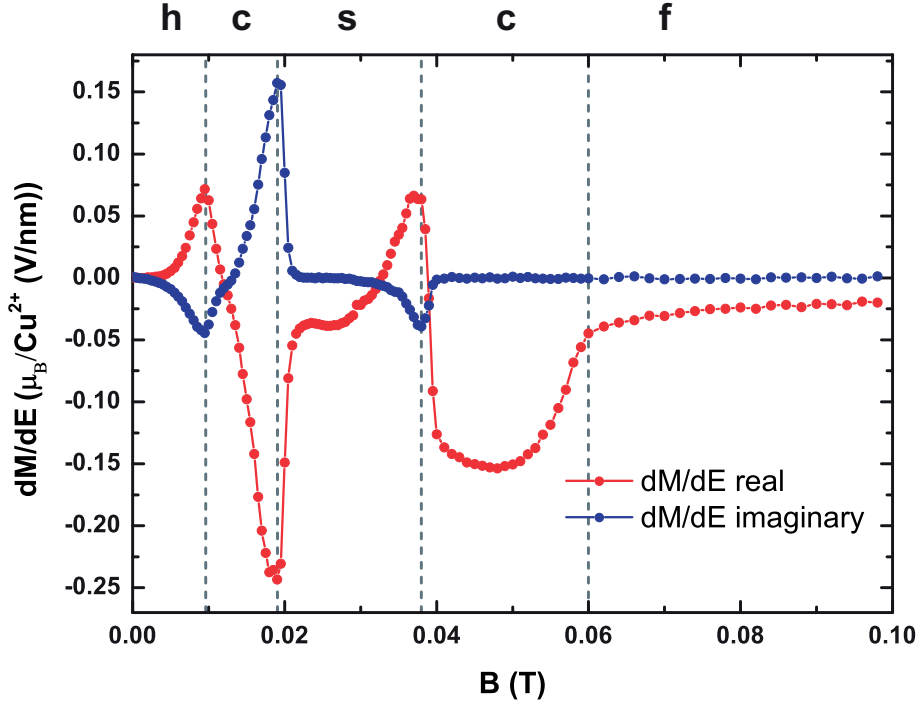


Figure 2.9 –  $dM/dE$  as a function of magnetic field at 58K. Note that a phase correction process was carried out to the original data to reduce the phase shift caused by the circuit.

phase, there is not such a sharp peak as in the helical phase, but directly the rise of the signal in the opposite direction of the critical correlation, then a broad bump indicates the appearance of the skyrmion phase until the system goes into the conical phase where the  $dM/dE$  signal increases linear with temperature. For the conical phase, the phase transition is characterized by a sharp jump, which is followed by a linear increase again.

Fig. 2.9 shows the magnetic field scan of  $dM/dE$  at 58K. As expected, the sample went through successively the helical phase, the conical phase, the SkL phase, the conical phase again and finally the ferri-phase. But the most striking feature is, instead of nearly invisible kinks in dc magnetization, there are very sharp peaks at the phase transitions, and hence the various phases can now be easily and well distinguished.

A typical phase diagram obtained from temperature scan of  $dM/dE$  at different magnetic fields is shown in Fig. 2.10, in which the phase boundaries between different phases can be clearly seen. Note that although the step of the magnetic field is coarse, with the finest step to be 20Oe, one can still get a skyrmion phase pocket well consistent with that reported in literature. Also note that the signals near the ordering temperature in low magnetic field phases are much stronger than those well inside the phases, implying strong fluctuation near the critical point.

A Ginzburg-Landau calculation[52, 55] has predicted a linear dependence of  $dM/dE$  on the

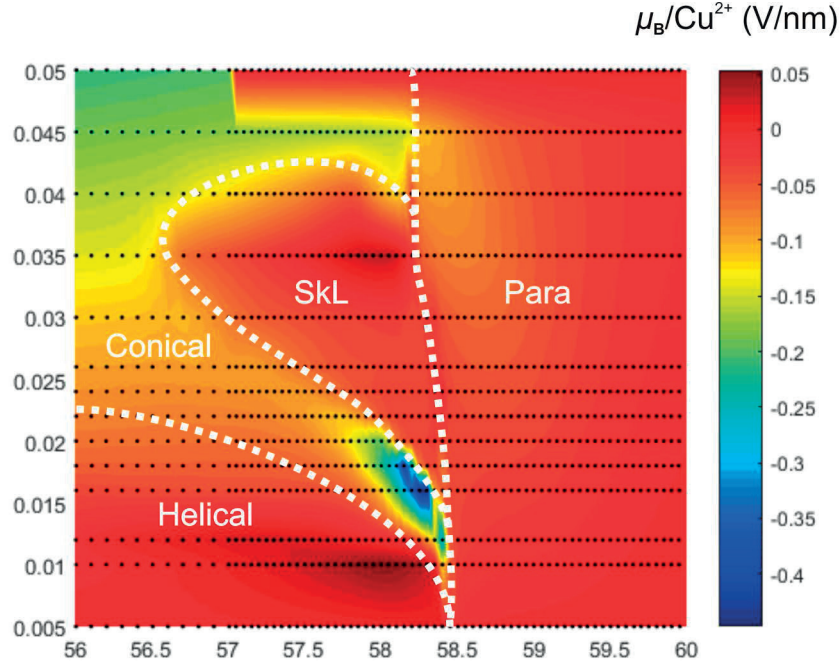


Figure 2.10 –  $B - T$  phase diagram of  $\text{Cu}_2\text{OSeO}_3$  extracted from temperature scan of  $dM/dE$  (the real part) at various magnetic fields. Phase boundaries among the helical, the conical, the SkL and the para- phase are clearly seen as indicated by white dot lines. Black spots indicate where the experiments were carried out.

applied magnetic field  $B$  in the conical phase:

$$dM/dE = 4\sqrt{3}(gn\mu_B|\mathbf{S}|)^2 \frac{\lambda}{(8JK^2)^2} B \quad (2.10)$$

where  $\lambda$  is the magnetoelectric coupling constant,  $n$  is the number of Cu sites in a unit cell and  $K = D/2J$  is the ratio between the DM and Heisenberg interactions. Thus by measuring  $dM/dE(B)$  in the conical phase then doing the linear fit, one can estimate the ME coupling constant  $\lambda$ . Such an example can be found in Ref. [52], and the resulting ME coupling constant was estimated to be  $\lambda = 0.0146 \text{ meV}/(\text{V/nm})$ , consistent with the value obtained by first principle calculations.

While our  $dM/dE$  technique gives very sharp phase boundaries, the ac magnetic susceptibility as function of the dc magnetic field just gives anomalies with discontinuous derivatives of the curve. It can be qualitatively understood if we note the magnetically induced electric polarization in Eq. 2.8. The nonlinear dependence of the electric polarization as a function of magnetization makes the magnetoelectric coupling here to be much more complex and thus exhibit very sharp peaks near the phase boundaries where fluctuations are strong.

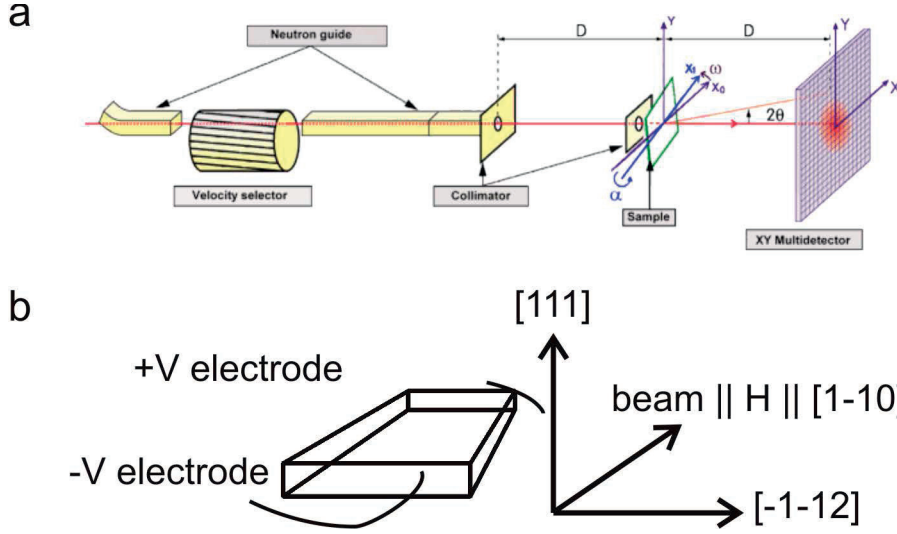


Figure 2.11 – **a.** Illustration of the SANS setup. Neutron beams scattered by the sample are detected by the detector long distance away from the sample so that only neutrons scattered within a small solid angle can be detected. This technique is very useful for magnetic structures with long wavelength modulation. **b.** E-field SANS sample configuration. Note that the applied E-field was in the same plane with the spontaneous electric polarizations.

Since all three types of ME coupling mechanisms discovered so far exhibit dependence of the local electric polarization as a function local magnetic moment to the second order, the unique feature of  $dM/dE$  technique is extremely suitable to investigate ME systems with complex phase diagram. In fact, I have applied this technique to several other ME systems, including  $\text{GaV}_4\text{S}_8$ ,  $\text{Ba}_2\text{CoGe}_2\text{O}_7$ ,  $\text{CaBaCo}_4\text{O}_7$  and  $\text{Ba}_2\text{MnGe}_2\text{O}_7$ , and high quality phase diagrams with sharp phase boundaries were obtained, consisting with reported results by other methods.

### 2.2.3 Small angle neutron scattering with electric field

Neutron, as an electrically neutral particle with spin 1/2, has unique interaction with matter. Neutron scattering is widely used to investigate the atomic structures, magnetic structures and magnetic interactions and excitations, by means of various techniques, including powder diffraction, small angle neutron scattering and triple-axis inelastic scattering *etc.*

Specifically for our skyrmion system, small angle neutron scattering (SANS) is a powerful tool to investigate the collective behavior of the skyrmion lattice in reciprocal space. The basic setup is shown in Fig. 2.11a. The incident monochromatic parallel neutron beam interacts with the sample located in a precisely controlled environment, such as temperature and magnetic field, and the scattered neutrons are counted by a 2D detector about a dozen of meters away from the sample, thus only those neutrons scattered within a small solid angle will be detected.

The first demonstration of a skyrmion lattice (SkL) by SANS was in 2009 in the B20 alloy MnSi,

where the scattering pattern of six scattering peaks arranged in hexagonal symmetry with long modulation was observed for the first time. Furthermore, with the addition of a temperature gradient, electric current applied to this metallic system was observed to successfully rotate the SkL. Note that the current needed to rotate the SkL was several orders of magnitude smaller than that of moving a magnetic domain wall.

For the insulating  $\text{Cu}_2\text{OSeO}_3$ , the unique magnetoelectric coupling implies the possibility of controlling the SkL by electric field. We carried out SANS measurements with the application of electric field and, for the first time, rotation of the SkL was observed. A perturbation theory with higher order magnetic anisotropic terms was developed to explain the behavior[7].

The sample was cut so that the largest surface was along the  $[111]$  direction, and the other two sides corresponded to  $[1\bar{1}0]$  and  $[\bar{1}\bar{1}2]$  respectively. In this case, the magnetically induced electric polarization was along  $[00\bar{1}]$ , which was on the  $[1\bar{1}0]$  surface, as shown in Fig. 2.11b. The external electric field, up to  $|E| = 1.89\text{kV/mm}$ , was applied along  $[111]$  direction via silver paste covering the two  $(111)$  surfaces so as to form a plate capacitance configuration. To prevent electrical breakdown, the sample space was pumped to vacuum, leaving only a very low pressure of pure helium gas for thermal coupling.

The experiments were carried out on SANS-I and SANS-II in the Paul Scherrer Institute, and the wavelength of the neutron beam was  $8\text{\AA}$ .

Fig. 2.12a shows the phase diagram obtained by temperature and field scan of the SANS pattern, well consistent with the reported results. Helical and SkL scattering patterns are shown respectively in the right panel. Note that both theoretical and experimental studies demonstrated that in the Bulk  $\text{Cu}_2\text{OSeO}_3$  system, the preferred directions of the helical propagation vectors are along  $\{001\}$ . For our sample and instrument configuration, only  $[001]$  can be observed. After transition to the SkL phase, one of the three pairs of the scattering spots preserved the  $[001]$  orientation.

The differences between scattering patterns before and after the application of electric field are shown in Fig. 2.12b. Rotations of the patterns in opposite directions were observed when opposite directions of electric field was applied respectively. Moreover, the largest angle achieved in opposite E-field directions are significantly different, showing a strong asymmetric behavior.

To understand this, we carried out analytical calculation based on a Hamiltonian containing Heisenberg interaction, DM interaction, Zeeman term, ME coupling and magnetocrystalline anisotropic terms up to the sixth order[7]. The zero order approximation reveals no effect of the ME coupling on the orientation of the SkL. However, after carrying out the first order

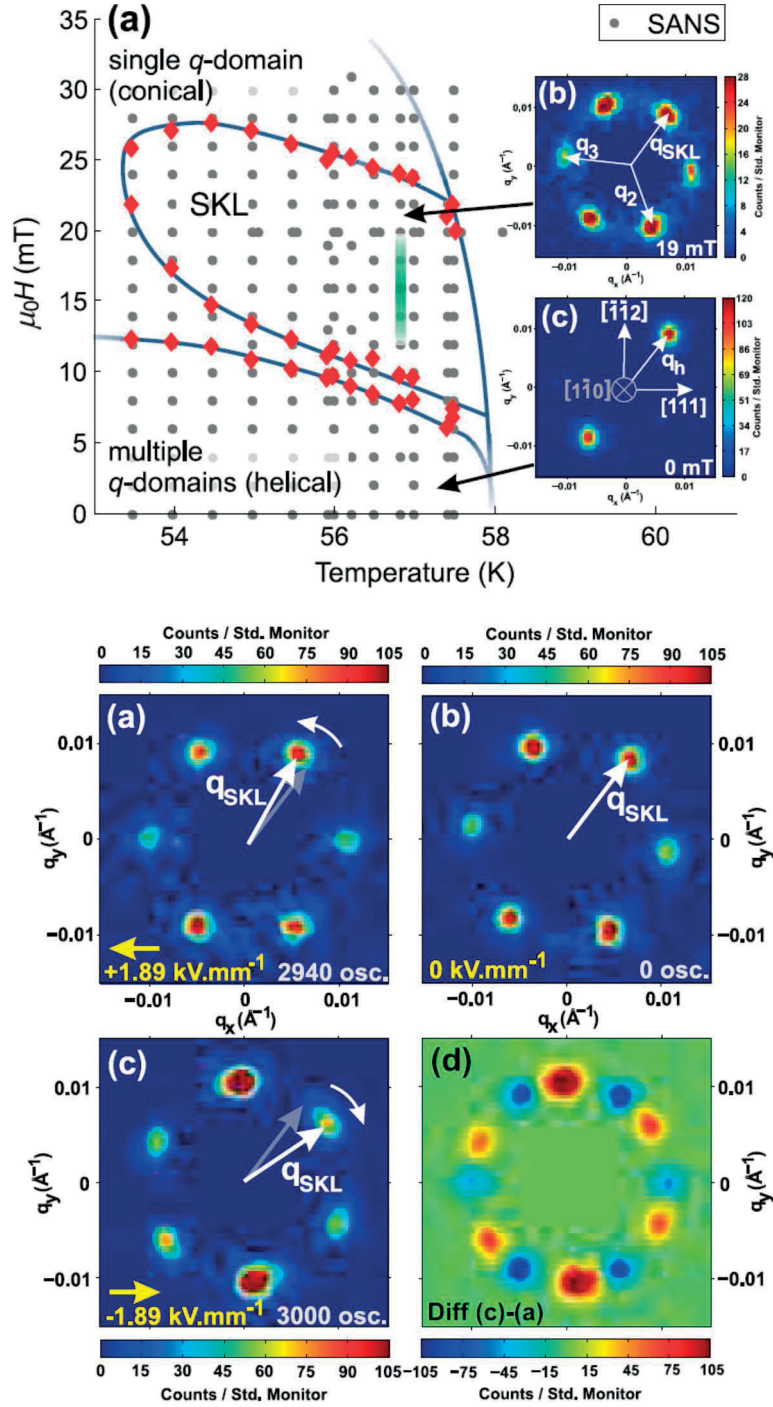


Figure 2.12 – A. The high-T portion of the magnetic phase diagram of  $\text{Cu}_2\text{OSeO}_3$ . Gray points denote where SANS measurements were done, and red diamonds the estimated locations of the phase boundaries. Insert (top to bottom): typical SANS images from the SKL phase and the zero-field helical phase respectively. B. (a-c) SANS diffraction patterns from the SKL with the sample under different electric fields, and (d) the foreground data of panel a, subtracted from those of panel c. The figures are reproduced from the author's published work[7].



perturbation, an electric field dependent anisotropic energy  $\mathcal{E}$  was obtained:

$$\mathcal{E} = \frac{3m_H^4}{512} ((\xi + \frac{\sqrt{2}}{4}\lambda)^2 + \lambda^2)^{-\frac{1}{2}} \cos 6(\phi + \theta_E) \quad (2.11)$$

where  $m_H$  is the helical component of magnetization,  $\xi = 5m_H^2 B$  ( $B$  represents the amplitude of the sixth order spin anisotropy),  $\theta_E$  describes the azimuthal SkL rotation angle away from the zero electric field orientation  $\phi$ , and

$$\theta_E = \frac{1}{6} \arctan\left(\frac{\lambda}{\xi + C\lambda}\right) \quad (2.12)$$

with  $\lambda = 270\sqrt{2}A\alpha E/Dk_0$ , containing the electric field  $E$ . Note that this expression indeed reveals an asymmetric dependence of the rotation on the electric field, as what observed in our experiments.

## 2.3 Conclusion

The magnetic and magnetoelectric properties of single crystal bulk  $\text{Cu}_2\text{OSeO}_3$  have been systematically investigated by dc magnetization, magnetoelectric susceptibility and SANS measurements.

The magnetization as a function of temperature revealed a magnetic ordering temperature at around 59K, with slight change with the variance of the given magnetic field. Sharp but narrow ranged, both in temperature and in magnetic field, anomaly can be seen at low field and temperature close to the magnetic ordering temperature, indicating the skyrmion phase. On the other hand, the magnetization versus field at base temperature revealed a saturation value of  $0.5\mu_B/\text{Cu}^{2+}$ , demonstrating ferrimagnetism as the polarized state with 3  $\text{Cu}^{2+}$  up and 1  $\text{Cu}^{2+}$  down in each  $\text{Cu}^{2+}$  tetrahedron. The M-H curve measured at 57.5K, a temperature within the SkL phase range, demonstrates various phase transition between the helical, conical, SkL and the ferri-phase.

Our unique  $dM/dE$  technique investigates directly the magnetoelectric coupling properties of  $\text{Cu}_2\text{OSeO}_3$ . The  $dM/dE(B)$  curves measured at the skyrmion temperatures exhibit sharp peaks at phase boundaries, clearly separate various phases, which is in sharp contrast to the the M-H curves in which phase transitions manifest themselves only as slight anomalies.  $dM/dE$  as a function of temperature, on the other hand, gives not only clean critical correlation near the transition from the paramagnetic phase to the magnetically ordered phase, but also exhibits dramatically different behaviors getting into different ordered phase, the underlying physics of which deserves deeper investigations both theoretically and experimentally.

Electric field induced rotation of SkL in  $\text{Cu}_2\text{OSeO}_3$  was demonstrated by our systematic SANS experiments and a perturbation theory considering magnetic anisotropic energy up to the 6th order was proposed to explain the observation. While more dynamical properties, such as SkL de-pinning from the underlying atomic lattice and SkL domain structures, real space information is highly demanded. The following chapters will provide observations and analysis in such a perspective of view.



## 3 Static investigation of SkL by LTEM

As mentioned in the previous chapter, real space and real time tools are highly demanded to investigate the dynamics of skyrmions and SkL. Lorentz Transmission Electron Microscopy (LTEM) is exactly such kind of technique that has been proven to be very powerful in this field. In this chapter, a brief introduction on the theoretical principle and practical process will be given. Then follow the LTEM results and analysis on the helical and SkL phase and various intermediate states. The main purpose of this chapter is to exhibit conventional magnetic phase properties of  $\text{Cu}_2\text{OSeO}_3$  in the form of thin slab sample in real space and real time, and also to establish a basis for more complex dynamical properties that will be discussed in Ch. 4 and Ch. 5.

### 3.1 Introduction to Lorentz transmission electron microscopy

In transmission electron microscopy (TEM), a beam of electrons are passed through a sample. Conventional TEM measurements include simple absorption measurements in the near field behind the sample. Various more complex imaging techniques exist, which utilise optical and/or coherence aspects of the electron beam.

When there is in-plane component of magnetic moment in the sample, the incident electron beam will interact with the moment according to the Lorentz's law:

$$\mathbf{F} = q(\mathbf{E} + \mathbf{v} \times \mathbf{B}) \quad (3.1)$$

where  $q$  is the charge of the particle,  $\mathbf{E}$  is the electric field and  $\mathbf{B}$  is the magnetic field.

As a result, the electron beam will be deflected, then some part of the detector will receive more electrons while some part less, as shown in Fig. 3.1, generating additional contrast to the conventional structure and element dependent TEM image, and thus reveal the magnetic

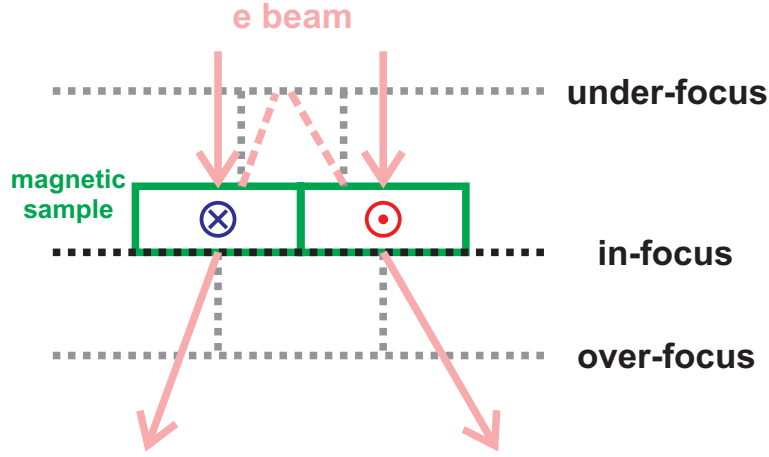


Figure 3.1 – Schematic illustration of the principle of LTEM.

textures, such as magnetic domain walls and long range magnetic modulation *etc.* To observe this deflection, however, one needs to set the focus of the lenses out of the sample, *i.e.* the microscope should work in the so-called Fresnel mode.

More quantitatively, according to quantum mechanism, the role of a magnetic field to an electron is adding a phase factor to the wave function of the electron through the magnetic vector potential. To see this, let's write the magnetic field and electric field in the form of a scalar and a vector potential:

$$\mathbf{B} = \nabla \times \mathbf{A}, \mathbf{E} = -\nabla\phi - \dot{\mathbf{A}} \quad (3.2)$$

Then, the Hamiltonian of an electron in magnetoelectric field will be:

$$H = \frac{1}{2m} \left( -i\hbar\nabla - \frac{q}{c} \mathbf{A}(\mathbf{r}, t) \right)^2 + q\phi(\mathbf{r}, t) \quad (3.3)$$

Consider only the magnetic vector potential  $\mathbf{A}$ , and insert Eq. 3.4 into the time dependent Schrödinger equation:

$$\frac{1}{2m} \left( -i\hbar\nabla - \frac{q}{c} \mathbf{A}(\mathbf{r}, t) \right)^2 \psi = i\hbar \frac{\partial \psi}{\partial t} \quad (3.4)$$

The solution of Eq. 3.3 has the following form:

$$\begin{aligned}\psi(\mathbf{r}, t) &= e^{ig(\mathbf{r})}\psi_0(\mathbf{r}, t) \\ g(\mathbf{r}) &= \frac{q}{\hbar c} \int_{\mathbf{r}_0}^{\mathbf{r}} d(\mathbf{r}') \cdot \mathbf{A}(\mathbf{r}')\end{aligned}\tag{3.5}$$

where  $\psi_0$  is the solution when  $\mathbf{A} = 0$ .  $\mathbf{r}_0$  and  $\mathbf{r}$  are the initial and final point of the electron respectively.

Thus there is a phase shift of the electron beam after going through a sample with magnetic moments, if the following two condition are fulfilled: 1. there is in-plane magnetic moments on the sample, and 2. the defocus value is nonzero. The former is due to the fact that if there is only the vertical magnetic moment, *i.e.* parallel with the beam, then the resulting magnetic vector potential  $\mathbf{A}$  will be perpendicular to the beam, thus the dot product  $d(\mathbf{r}') \cdot \mathbf{A}(\mathbf{r}')$  will vanish. For the latter, in focus means  $\mathbf{r} = \mathbf{r}_0$ , and in this case the integration will always be zero. These conclusions are consistent with those got from the classical theory, and the phase shift is the origin of the magnetic contrast. More generally speaking, the magnetic structure we get from LTEM is a phase contrast.

On one hand, this phase of the electron beam, say having a plane wave function  $\Psi(x, y, z) = \sqrt{I(x, y, z)}e^{-ikr}e^{i\phi(x, y, z)}$ , passing through a magnetic sample contains information of its in-plane magnetic moment distribution; on the other hand, this phase can be retrieved by the so-call Transport-of-Intensity Equation (TIE)[56]:

$$\frac{2\pi}{\lambda} \frac{\partial}{\partial z} I(x, y, z) = -\nabla_{xy} \cdot (I(x, y, z) \nabla_{xy} \phi(x, y, z))\tag{3.6}$$

where  $\lambda$  is the wavelength of the electron beam, along the  $z$ -axis.  $I(x, y, z) = \Psi\Psi^*$  is the intensity of the electron beam, which is the quantity directly measured by the detector.  $\phi(x, y, z)$  is the phase. Solving Eq. 3.5, one gets:

$$\phi(x, y, z) = -\frac{\lambda}{2\pi} \nabla_{xy}^{-2} \nabla_{xy} \cdot \left( \frac{1}{I(x, y, z)} \nabla_{xy} \nabla_{xy}^{-2} \frac{\partial}{\partial z} I(x, y, z) \right)\tag{3.7}$$

where  $\nabla_{xy}^{-2}$  is the inverse Laplacian operator. Eq. 3.6 can be solved by Fourier transform given that

$$\nabla_{xy}^{-2} = -F^{-1} g^{-2} F\tag{3.8}$$

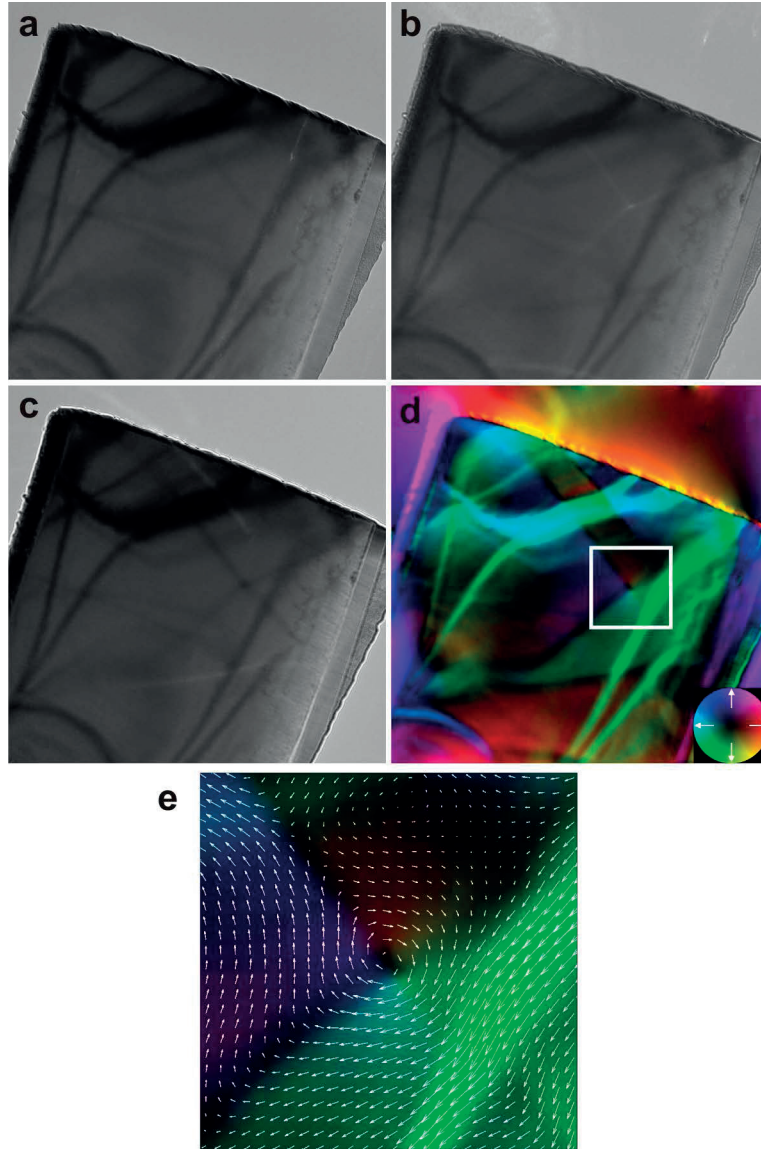


Figure 3.2 – The process of retrieving the magnetic moment distribution of a magnetite sample by TIE. **a.** In focus image of the sample. **b.** and **c.** Under and over focus images respectively. Additional magnetic contrast appears in both images, as indicated by arrows. **d.** Magnetic moment distribution obtained by TIE. The hue of the color map denotes the directions of the moments and the saturation denotes the intensity.

with  $g^2 = g_x^2 + g_y^2$  to be the square of the amplitude of reciprocal vectors.

In practice, the  $\frac{\partial}{\partial z} I(x, y, z)$  term is approximated by:

$$\frac{\partial}{\partial z} I(x, y, z) = \frac{I(z + \Delta) - I(z - \Delta)}{2\Delta} + O(\Delta^2) \quad (3.9)$$

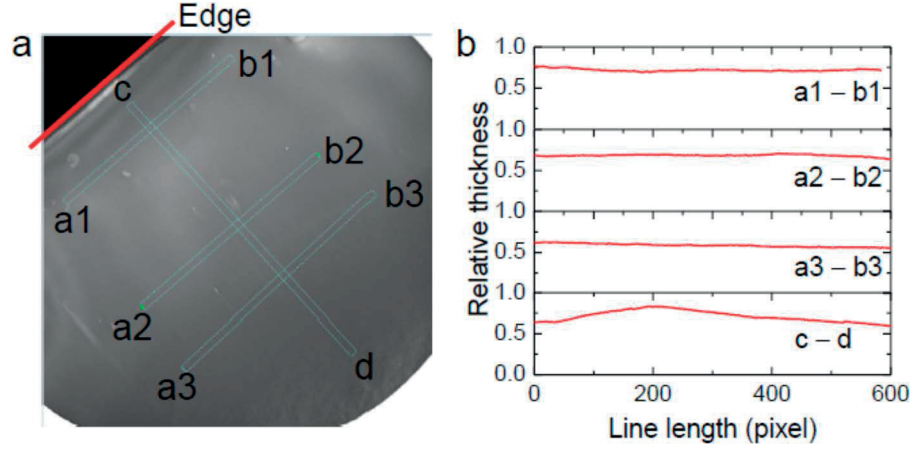


Figure 3.3 – **a**. Thickness map of my sample. Four lines each of 20 pixels thick are marked in the thickness map along which line profiles were recorded. The line profiles are shown in **b**. The relative thickness remains practically constant at 0.6 along the lines parallel to the edge whereas for line perpendicular to the edge, the relative thickness varies between 0.6 - 0.7.

So to get the phase distribution at the sample plane, *i.e.*, in focus with  $z = 0$ , at least three images  $I(0)$ ,  $I(-\Delta)$  and  $I(\Delta)$ , are needed.

Knowing the phase distribution, the magnetization distribution  $\vec{M}$  on the sample can then be quantitatively revealed by:

$$\nabla_{xy}\phi(x, y, z) = -\frac{e}{\hbar}(\vec{M} \times \vec{n})t \quad (3.10)$$

where  $\vec{n}$  is the unit vector along the beam direction and  $t$  is the thickness of the sample.

Fig. 3.2 shows an example of such a phase retrieval process carried out for magnetite. Magnetic domain walls can be clearly seen in the defocused images and domains with different magnetization orientations are clearly retrieved by TIE.

## 3.2 Experiments

$\text{Cu}_2\text{OSeO}_3$  single crystals were first aligned and cut so that the main planes were perpendicular to  $[111]$  or  $[1\bar{1}0]$  directions respectively. Then the rectangularly shaped samples were mechanically polished down to about  $20\mu\text{m}$ . Focused Ion Beam (FIB) was adopted to further mill a TEM lamella of about  $150\text{nm}$  thick. A thickness of  $100\text{-}200\text{nm}$  is chosen to be thin enough to have sufficient electron transmission, but thick enough to have good magnetic contrast. A thickness map obtained by energy filtered TEM imaging is shown in Fig. 3.3, demonstrating a good thickness homogeneity.

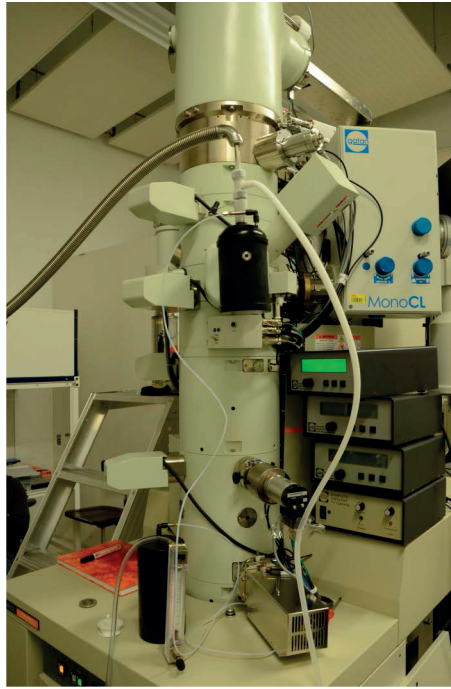


Figure 3.4 – Setup of my LTEM experiment in a JEOL 2200FS TEM. Connection of the transfer tube to the liquid helium sample hold ensures an easy handling of the cryogen so that improves the efficiency of the experiments.

The whole setup of the low temperature LTEM is shown in Fig. 3.4. The TEM in the figure is JEOL 2200FS with free lens control mode, in which the objective lens can be controlled freely to provide external magnetic field in a single polarization; a FEI Titan Themis TEM was also used. One advantage of the latter is having a Lorentz mode with bipolar magnetic field. The sample was installed in a Gatan liquid helium sample holder with 4 electric feed-through, allowing connection to external instruments.

Rather than connecting the holder to a vacuum pump to generate the helium gas flow, I kept the liquid helium transfer tube linked between the reservoir and the holder and maintained a (almost) constant over pressure in the reservoir to drive the liquid helium in the holder to flow through the cold head so as to cool the sample down. Since there are springs fixing the holder to the TEM goniometer and relatively low magnifications (maximum  $7700\times$ ) were used in the experiment, the vibration of the holder is negligible. The advantages of this setup include much easier control of the liquid helium transfer and longer low temperature experiment time (up to two hours, much longer than the guaranteed value of 40 minutes).

### 3.3 LTEM observation of the helical phase

Fig. 3.5 shows the LTEM image of the helical phase, obtained at  $T = 23.2\text{K}$  and  $B = -176\text{Oe}$ , which manifested itself as parallel stripes with alternating dark and bright contrasts, forming



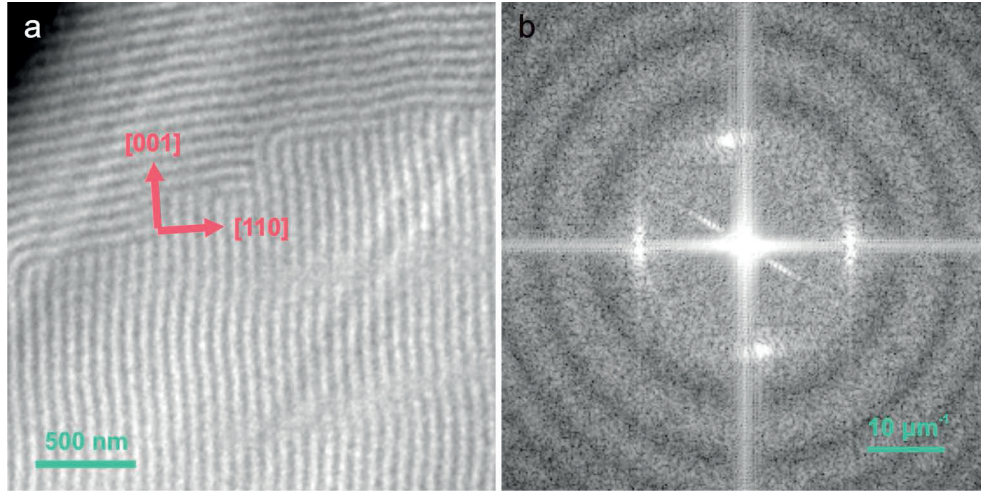


Figure 3.5 – **a.** Two helical domains perpendicular to each other in the  $[1\bar{1}0]$  plane. Note that  $[001]$  and  $[110]$  directions are preferred in bulk and thin plate sample respectively. **b.** The FFT of **a.**

a one-dimensional lattice. In the Fourier transform, one can see two sets of Bragg spots, corresponding to the two helical domains in the real space image.

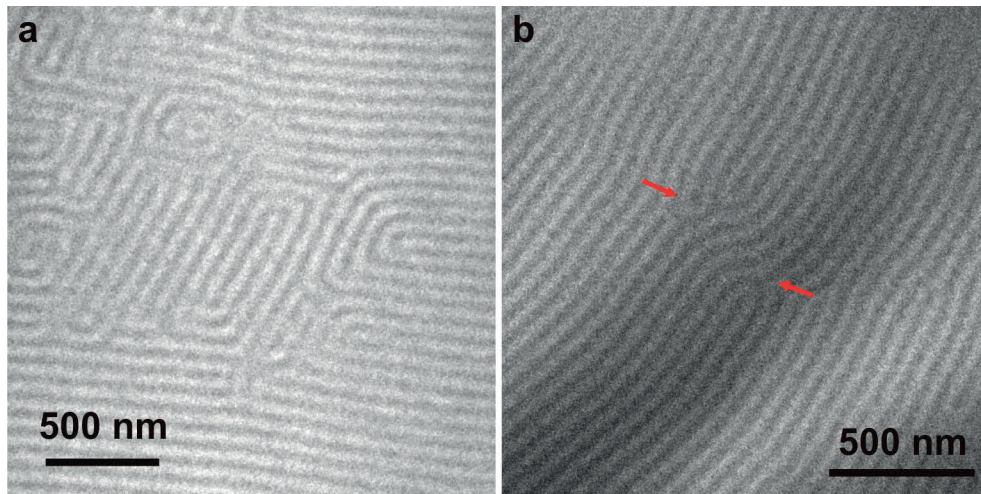


Figure 3.6 – **a.** Closed helices **b.** Helices with a dislocation pair as indicated by arrows.

The energetically preferred wave vector orientation of the helical phase in thin film  $\text{Cu}_2\text{OSeO}_3$  sample is along  $\{110\}$  directions, reported experimentally[20] and confirmed theoretically[41], different from that along  $\{100\}$  directions in bulk samples. This is clearly seen in the lower part of Fig. 3.5. However, a helical domain along  $[001]$  direction was also observed, in Fig. 3.5a upper part. This indicates that perturbing factors, such as the edge of or cracks in the sample can stabilize other directions of the helical propagation vector.

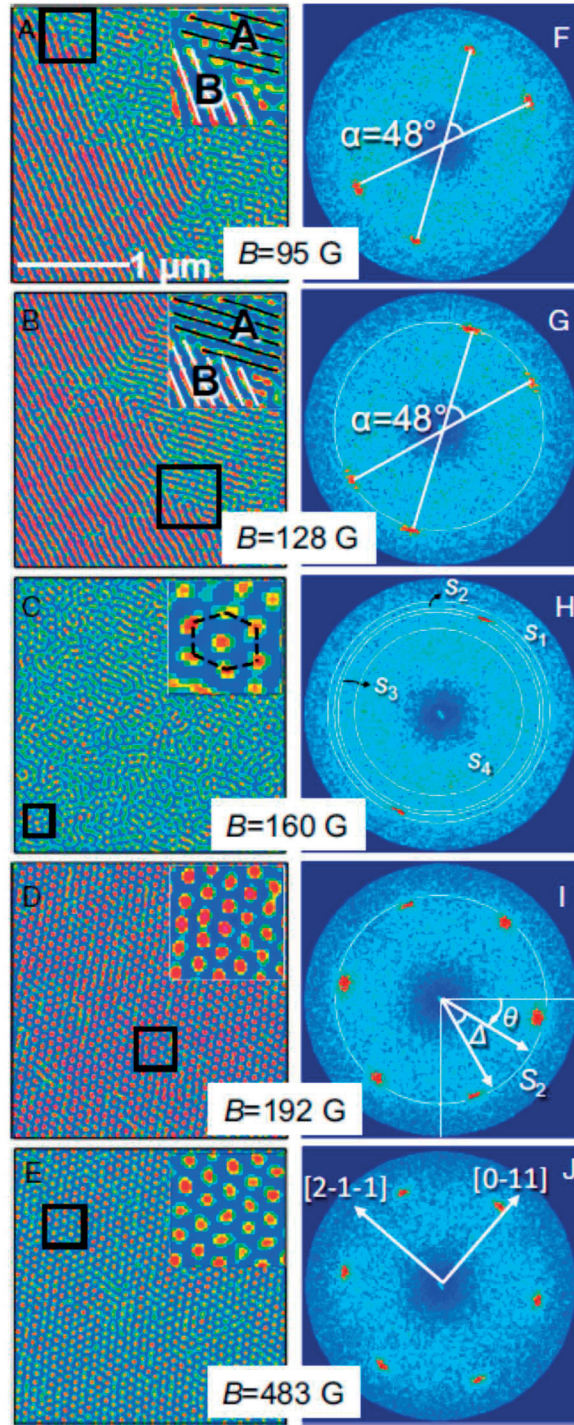


Figure 3.7 – **A. - E.** Real space images and **F. - J.** their FFT of the magnetic phase transition from the helical phase to the SkL phase. At  $B = 95\text{G}$  and  $B=128\text{G}$ , the helical phase with two different helical domains is observed.  $B=160\text{G}$  represents a transition region from the helical to skyrmion phase. At higher fields, a complete SkL phase is observed. The figures are reproduced from the author's published work[57].



Various defects can be seen in the helical phase. As local defects, the helical lines can be closed or rolling, as shown in Fig. 3.6a. Dislocations, a type of global also topological defects, is shown in Fig. 3.6b. Topological defects play an very important role in lattice dynamics, which will be further discussed in the following.

### 3.4 Magnetic field induced helical to SkL phase transition

Upon increasing of the magnetic field, the system undergo a transition from the helical phase to SkL phase[57]. Note that due to the constraint in the thickness of the sample, there will not be conical phase, and SkL phase extends to much larger temperature and magnetic field ranges, in contrast to the bulk samples.

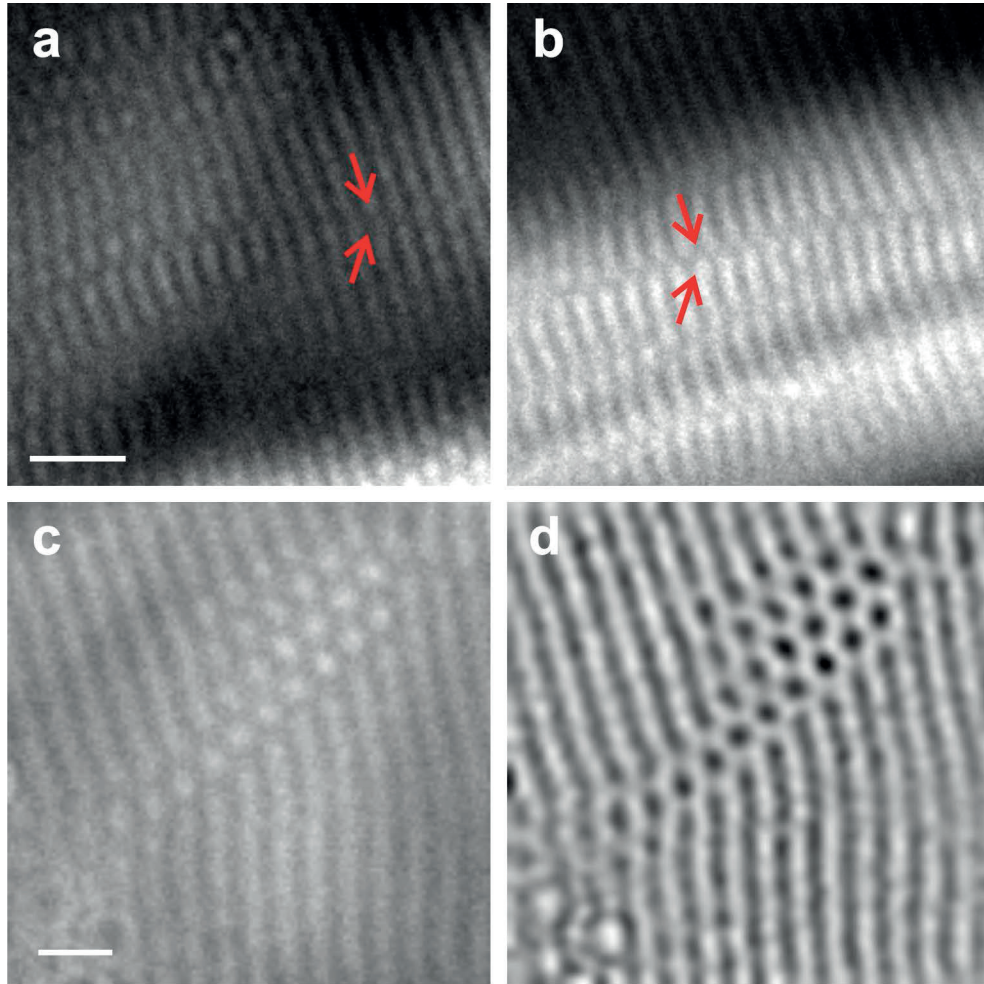


Figure 3.8 – Defects in the helical phase. Aligned **a.** and half lattice constant shifted **b.** broken helices. An end of a helix is called a meron or a half-skyrmion with the skyrmion number of  $1/2$ . **c.** Skyrmion clusters in helical background. **d.** LoG filtering of **c.** for better illustration. Both scale bars are 50nm.

Fig. 3.7 shows the phase transition process at  $T \approx 7\text{K}$  with the increase of the magnetic field. The helical phase showed up spontaneously when cooled down to temperature below the ordering temperature about 60K. The helical phase stayed stable (Fig. 3.7a and b) with the increase of the magnetic field until 160G, at which the helices became glassy (Fig. 3.7c). At higher field established the SkL phase, the image of which exhibits dark spots formed triangular lattice as shown in Fig. 3.7d.

If going further into the helical-SkL crossover regime, more physics will arise. Analytical[58] and numerical[59] calculations both demonstrated that right at the end of a helix, spins will close the line and form a texture having the skyrmion number of 1/2, thus the end of a helix can be viewed as a "half-skyrmion", and an interrupted helix line can be seen as two half-skyrmions. Fig. 3.8a and b shows ended helices aligned ( $T \approx 29.3\text{K}$  and  $B = -365\text{Oe}$ ) and half lattice constant shifted respectively ( $T \approx 27.3\text{K}$  and  $B = -365\text{Oe}$ ). Individual and clusters of skyrmions were also found in the helical phase, as shown in Fig. 3.8c ( $T \approx 25.9\text{K}$  and  $B = 262\text{Oe}$ ). These results provide abundant potential of further investigating the crossover between the helical and the skyrmion phase.

TIE analysis was carried out for the SkL, as shown in Fig. 3.9. Combining real space images acquired at in-focus,  $400\mu\text{m}$  over and under focus ( $B = -443\text{Oe}$ ), the in-plane magnetic moment distribution of the sample was retrieved and shown as a color map, with the hue representing the directions of the moments and the saturation representing the intensity. One can see that for each skyrmion in the real space images, the TIE calculation gives a closed counter-clockwise wheel, well consistent with the theoretical expectation for a (right-handed) Bloch type skyrmion.

### 3.5 Defects and fluctuations in SkL

Similar to conventional atomic lattices, SkL is usually NOT a perfect lattice globally, with various defects existing, among which topological defects, including dislocations and disclinations, are the most important for the thermodynamic properties of SkL. To see that, I did further analysis to the SkL images.

Firstly, skyrmions were identified in each image through an automatic algorithm (detailed description can be found in App. B), and the location coordinates of all skyrmions were obtained. Then Delauney triangulation was carried out to characterize the neighbouring relations among skyrmions. In this step, skyrmions that do not have 6 neighbours were highlighted. There can be artifacts in the results, thus a manual correction was followed at the end. Fig. 3.10a shows an example of processed images.

Now dislocations formed by a pair of 5-7 polygons are clearly seen, as further indicated in Fig. 3.10b and c, with the zoom-in of a single such feature. Notice that 4 lines go in and only 3 lines go out in 2 of the 3 main directions, leaving the last direction unaffected. Although a dislocation seems a local imperfection of the lattice, it does actually have a global impact,

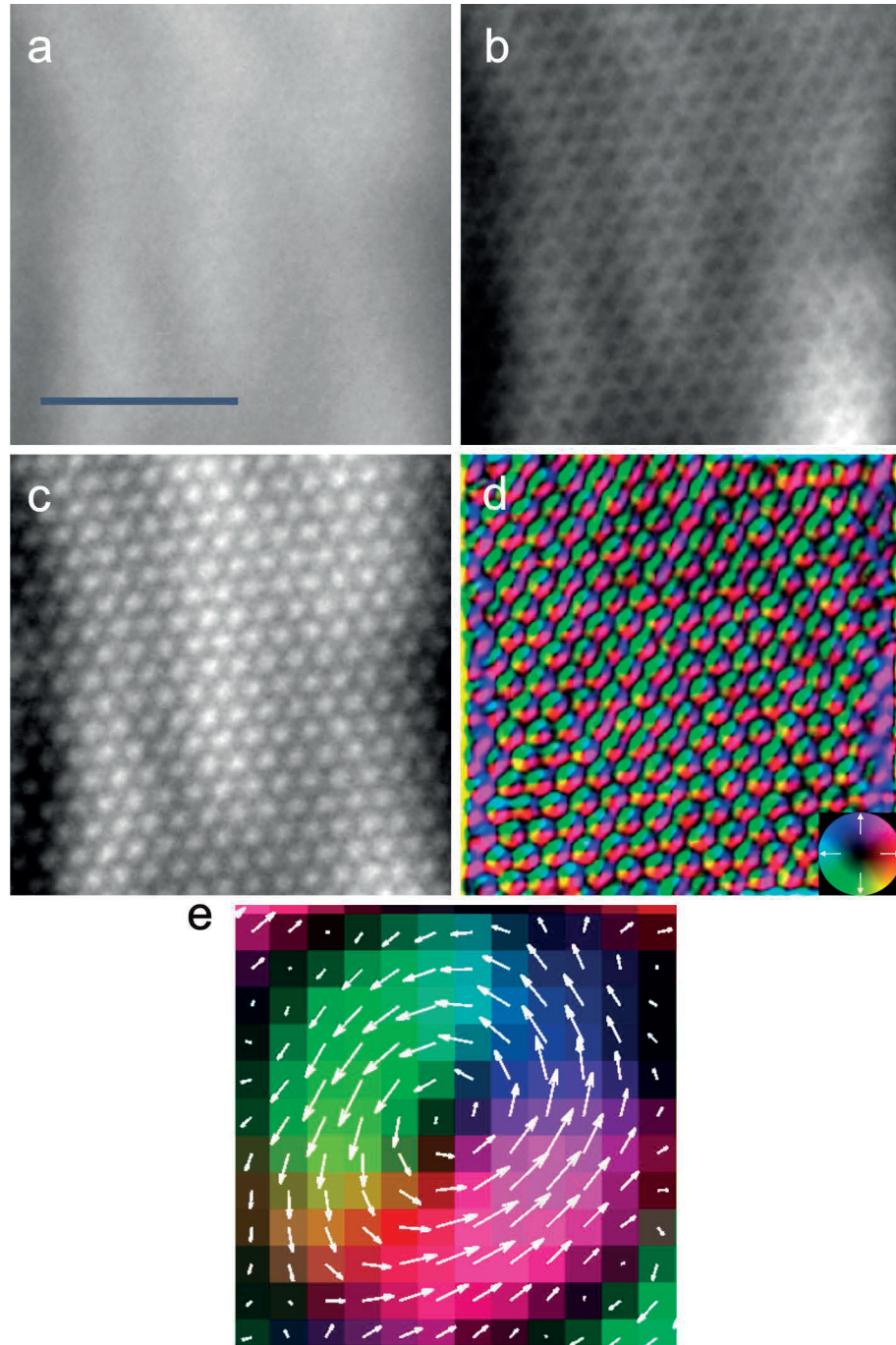


Figure 3.9 – TIE analysis of the SkL. **a.** - **c.** Real space LTEM images acquired at 0, +400 μm and -400 μm defocus values respectively. **d.** Retrieval of the in-plane magnetic moment distribution shown as a color map, in which the directions and the intensities of the local magnetic moments are represented as the hue and saturation respectively summarized as a color wheel in the insert. The scale bar is 500 nm. **e.** A magnified view of a single skyrmion with local magnetization distribution indicated by white arrows.



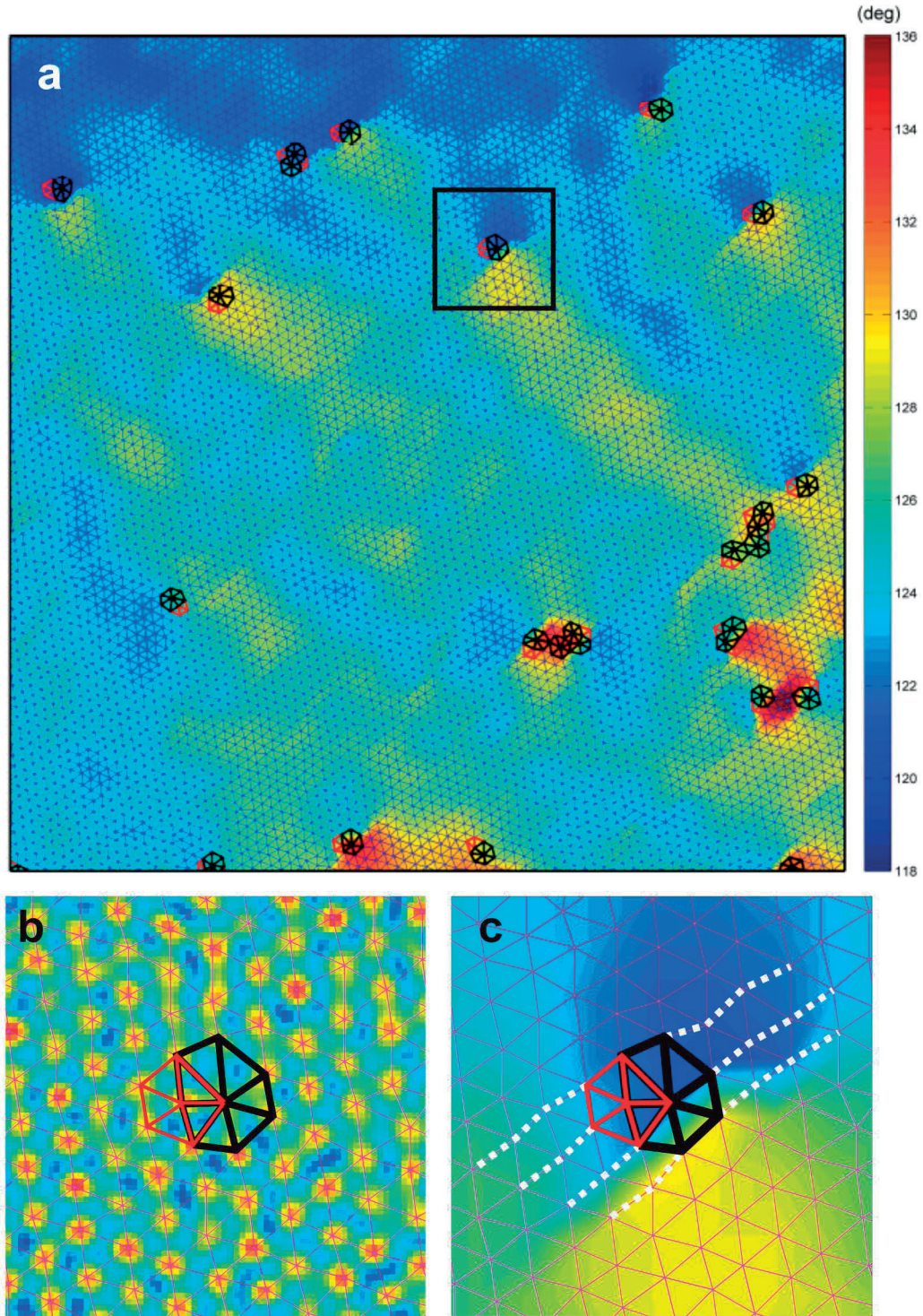


Figure 3.10 – **a.** Local orientational map of a large scale SkL. **b.** A SkL and a Delaunay triangulated lattice (magenta lines) obtained for  $B=483\text{G}$ . A skyrmion pair with 7- and 5- neighbors respectively is highlighted with black and red lines. **c.** A zoom-in of the region marked by the square in **a.** White dashed lines are guide for the eye to indicate the dislocation. The figure is reproduced from the author's published work[57].

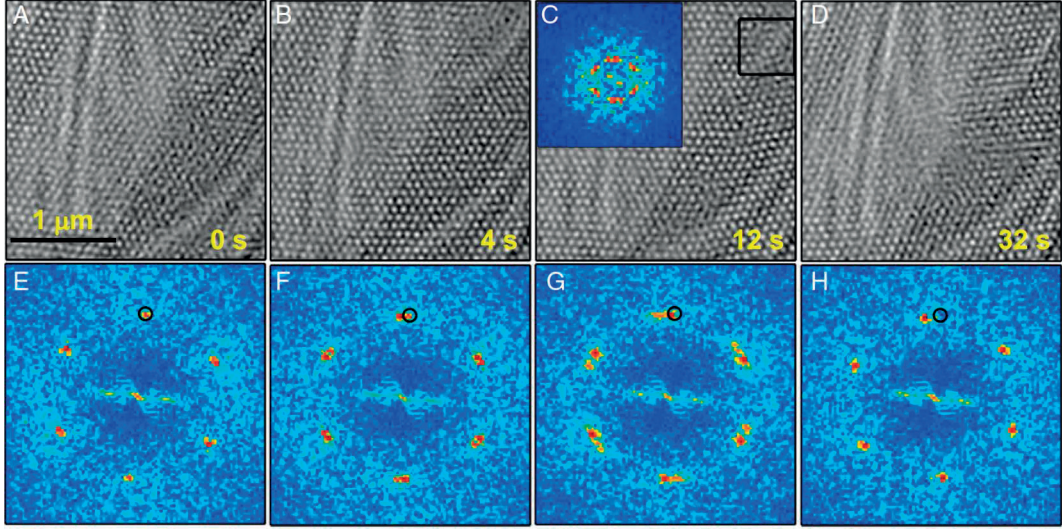


Figure 3.11 – **A. - D.** The real-space images and **E. - H.** the corresponding FFT at the relative time as labelled. Fluctuations of the SkL and formation of domains with different orientations as a function of time are evidenced by the splitting and unsplitting of the Bragg peaks and their continuous change of position. The figures are reproduced from the author's published work[57].

as one can find out from the local orientation distribution map in Fig. 3.10a. The color map was calculated by taking a small portion of the image, typically  $70 \times 70$  pixels and moving this window in a small step to scan the whole image, then doing FFT in each window, identifying the orientation of the Bragg peaks. It is clearly shown that there are domains with distinct orientations throughout the lattice, and right on the boundaries of different domains locate the dislocations. As one can see the following chapters, topological defects can be involved in other interesting physics of the lattice dynamics.

One the other hand, SkL is not a static collection of skyrmions, but it continuously fluctuates in the presence of thermal and/or field excitations. Fig. 3.11 shows the fluctuation in conventional LTEM conditions, *i.e.* with temperature and magnetic field somewhere in the middle of the phase diagram. Small but finite swinging can be clearly seen.

Moreover, it has been reported that concentrated electron beam radiation can cause the rotation of the SkL due to the magnon propagated STT[39]. I also observed such phenomena, as shown in Fig. 3.12 ( $T \approx 13\text{K}$  and  $B = -408\text{Oe}$ ). However, contrary to what was reported in literature, I was able to observe rotation in both clock-wise and anti-clockwise direction, which may require a re-consideration of the mechanism of rotation.



### 3.6 Discussion

There are many TIE analysis on the helical phase and SkL phase in literature, however, technical details are rarely mentioned. According to my experience, the key issue to get a good magnetic moment distribution map is the perfect alignment of corresponding objects between the multiple images taken with under, on and over focus. Any drift between these images must be corrected for.. Thus several factors should be carefully considered.

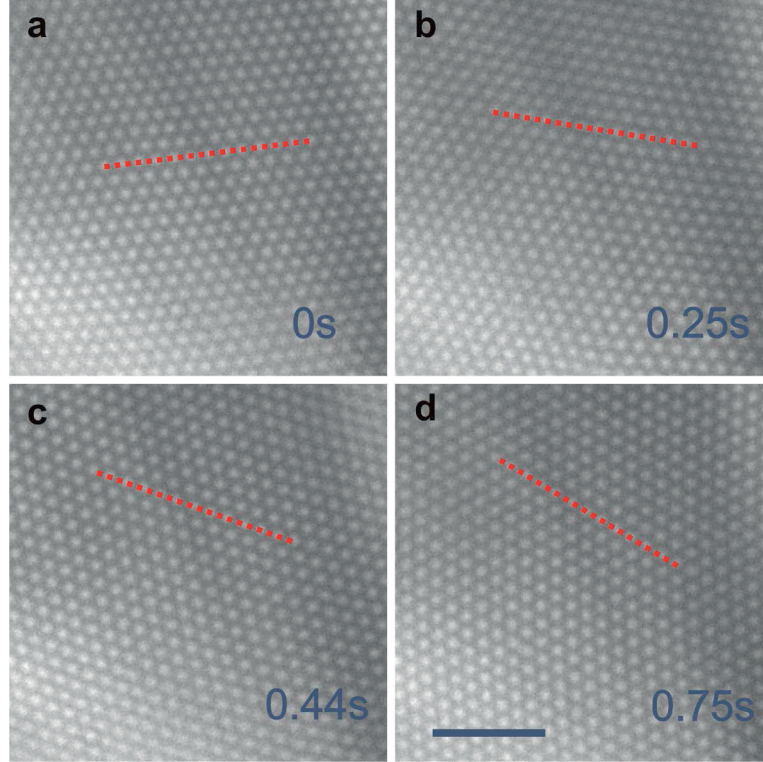


Figure 3.12 – Electron beam radiation induced a clockwise rotation of the SkL. Red dashed lines are guide for the eyes. The scale bar is 500nm.

Firstly, one should minimize the thermal fluctuations of objects. A good solution will be cooling down the sample to as low temperature as possible and diverging the electron beam. Second, change the focus value as quickly as possible with each image exposed in a short time. This can further lower down the impact of fluctuations. For the consideration of aligning images (see App. A for more details), include some special features in the images such as edges and cracks *etc.*

Practically, if calculating directly using Eq. 3.7, one will probably get a result that contains a slowly varying feature covering the desired phase variance from objects under investigation. Ishizuka and Allman[56] suggested a Tikhonov-type filter  $T(g) = g^2 / (g^2 + g_c^2)^2$  to replace the  $g^{-2}$  factor in the inverse Laplacian operator defined by Eq. 3.8. Here,  $g_c$  is a constant vector in the reciprocal space and usually have a value of several  $g_0 = 2\pi/l$ , the basic spacial frequency

in fourier transform. If taking care of all issues mentioned above, one should get a very nice TIE result.

A very interesting question, yet unfortunately not discussed in detail here, is how the 2D SkL arranges. Peierls[60] indicated qualitatively that there be will no long range order in one- and two-dimension due to thermal fluctuations. This is further quantitatively proven by Mermin[61] using a rigorous inequality. Specifically for 2D crystalline system, Kosterlitz and Thouless[62] proposed a quasi long range order, they named it as topological long range order, in which the translational order decays algebraically.

On the other hand, calculations were carried out for periodic systems by Giamarchi and Doussal[63] in the presence of weak (impurity) disorder, and they found a both glassy and quasicrystalline phase, as they called the Bragg glass, in which the mean square relative displacements exhibit crossovers among three regimes. As the authors pointed out, the analogy of the quasicrystalline between the Bragg glass and the general 2D lattice is puzzling, the SkL discussed here might be a good model system to investigate the general thermodynamics of 2D lattice, especially provided that we can get more than the order of magnitude of  $10^5$  skyrmions in a single image. In fact, some attempts will be presented in the next chapter in which the melting process of the SkL induced by magnetic field was quantitatively analyzed including the positional order.

### 3.7 conclusion

Thermodynamical properties of thin slab (*i.e.* geometrically constrained quasi-2D)  $\text{Cu}_2\text{OSeO}_3$  samples were investigated systematically by LTEM. Helical phase and SkL phase were observed and basic characterizations were carried out. While the preferred orientation of the helical phase in thin slab sample is different from that in bulk samples, the wavelength of the modulation remains the same as reported in literature.

The whole process of helical to SkL phase transition was recorded by LTEM and a glassy state near the phase boundary was reported for the first time. Besides nearly perfect 2D lattice of helices and skyrmions that are common in literature, various defects and fluctuations are observed and analyzed. Dislocations, a type of topological defects, were reported for the first time and the local orientation map in a defected SkL revealed that these defects serve as the origins of domains with different local orientations.

The so-called half-skyrmions, or also known as merons, were also observed, which manifest themselves as the ends of helices, with the topological number to be  $1/2$ . There were 3 different types of configurations: aligned breaking helices, shifted breaking helices and breaking helices with skyrmions in between. The angle of between the breaking line and the propagation vector of helices was observed to be about 24 degree, in good agreement with micromagnetic calculations.

### **Chapter 3   Static investigation of SkL by LTEM**

---

Thermal fluctuations, either spontaneous in fixed conditions or tuned by electron beam radiation, were also reported. These abundant phenomena call for more efforts in theories that should combine general 2D lattice dynamics and magnetic excitation consideration.



## 4 Magnetic field induced melting of SkL

It is of great importance and interest to understand whether SkL, a 2D lattice formed by topological magnetic quasi particles, has similar thermodynamic properties as conventional lattices. A typical thermodynamic behavior is melting, a phase transition from long range ordered crystal phase to liquid phase with only short range order through increasing temperature or tuning other parameter such as external fields. In this chapter, I will present the observation of the magnetic field induced melting of SkL and demonstrate via comprehensive quantitative analysis that the microscopic physics of the melting process obeys the topological defects mediated 2-step theory proposed by Kosterlitz, Thouless, Halperin, Nelson, and Young (KTHNY theory) [62, 64, 65].

### 4.1 Introduction to 2D lattice melting

Periodic arrangements of objects forms lattices. The symmetry in a lattice is lower than that in liquid or gas phases in which objects locate randomly. There are only 1, 2, 3, 4 and 6 fold rotational symmetries and a discrete long range translational symmetry in a lattice, while in the liquids, there are continuous rotational and translational symmetries. In addition, there are spatial inversion, mirror plane reflection, screw axis and slide plane symmetries allowed in a lattice. The combinations of those symmetry operations can be described by space groups and all together there are 230 types of space groups for 3D lattice and only 17 types in 2D.

When tuning parameters such as temperature and external field, the system can undergo transitions between phases. Spontaneous breaking of symmetries is a common feature in phase transitions from high temperature high symmetry phase to low temperature low symmetry phase. Using mean field method, Landau developed a theory describing continuous phase transition, and in this theory, concepts such as symmetry breaking and order parameters were proposed. Theoretical and experimental studies both revealed macroscopic universal classes behaviors near the critical point of a second order phase transition, irrelevant to the microscopic interaction details but depending only on the degree of freedom and dimensionality.

On the other hand, in the microscopic scale, the lattice points are not fixed in positions, but vibrate in various collective modes. The energies of these vibration modes are quantized, and the quantized quasi-particles are called phonons. As temperature increases, the amplitudes of the lattice vibrations will increase correspondingly. So generally speaking, once the vibration amplitudes reach a certain value, *i.e.* the empirical Lindemann criterion[66], the crystal will lose the long range order and melt.

Apparently, such a simple phenomenological picture is far from precise description of lattice melting. In fact, in the 3D case, the melting mechanism has been under debating for a long period of time, yet no agreement has been reached. However, in 2D, the KTHNY theory provides a detailed description of a two-step melting process and has been demonstrated suitable in many systems including suspended colloid lattices on the liquid surface[67], the vortex lattices in type-2 superconductors[68] among other realizations.

### 4.1.1 Topological defects and the KTHNY theory

As already shown in Ch. 3, topological defects such as dislocations exist in the SkL, giving a global impact on the whole lattice. There are mainly two types of topological defects in 2D lattices, dislocations and disclinations, representing the breaking of the long range translational and orientational orders respectively. These topological defects play the essential role in the KTHNY mechanism of 2D lattice melting.

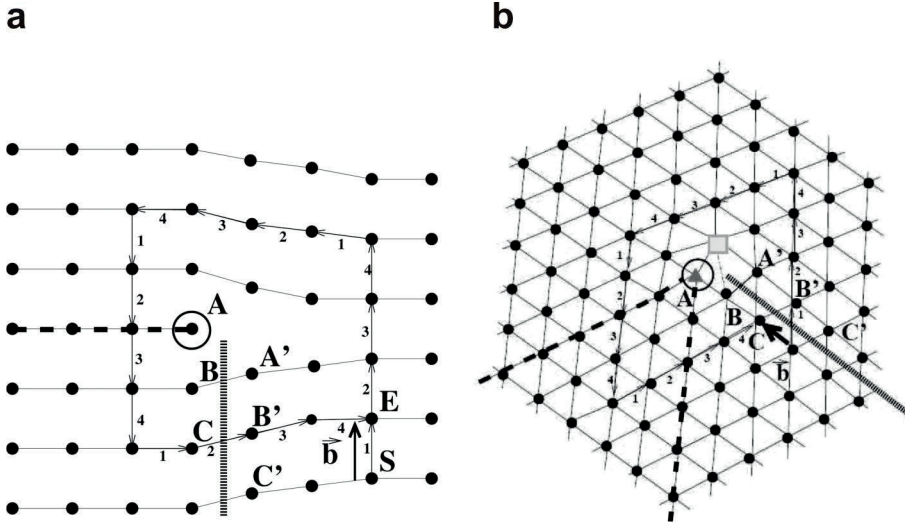


Figure 4.1 – Illustration of dislocations respectively in **a.** square lattice and **b.** triangular lattice. The Burgers vector in each case is also shown. The figures are reproduced from Ref. [1].

The first type of the topological defects, dislocations, can be considered as insertion of half lattice lines into a perfect 2D lattice, as illustrated in Fig. 4.1. One can see that it is impossible to create a single dislocation due to any continuous transformation, and that is why dislocations are called topological defects. A characteristics of a dislocation is the Burgers vector, as shown

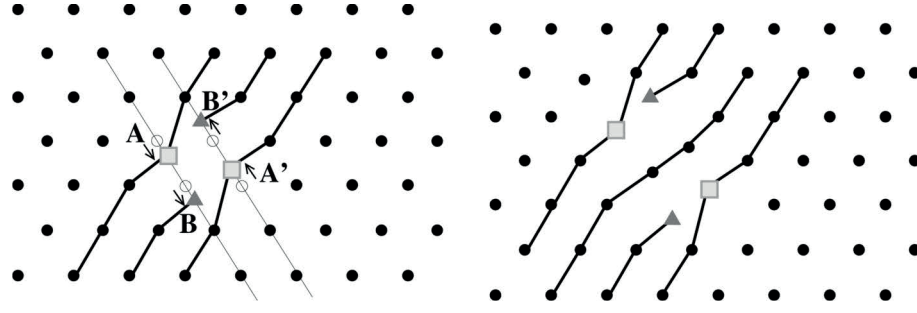


Figure 4.2 – Illustration of the formation of a dislocation pair by mismatch. The figures are reproduced from Ref. [1].

as the arrow in Fig. 4.1. It can be determined by drawing a closed loop around the dislocation and summing up all the vectors in the loop, then the net step, corresponding to a lattice vector, is the Burgers vector. If cutting the lattice along the thick shadow line in Fig. 4.1 and reconnect lattice points, the regular lattice can be restored.

As already fully demonstrated in the Ch. 3, in a triangular lattice, to which the SkL belongs, a dislocation can be viewed as a 5-7 defect pair, and thus a pair of dislocations, in contrast to a single one, can form without inserting or removing any lattice lines, but only needs a mismatch of two lattice sites, as illustrated in Fig. 4.2. One can see that such a relative movement of two lattice sites gives rise to two pairs of 5-7 defects, corresponding to two dislocations. Note that the Burgers vectors of the two dislocations are in opposite directions, and thus they sum up to zero. More generally, a collection of dislocations with vanished sum of Burgers vectors can form through continuous transformation from a regular lattice.

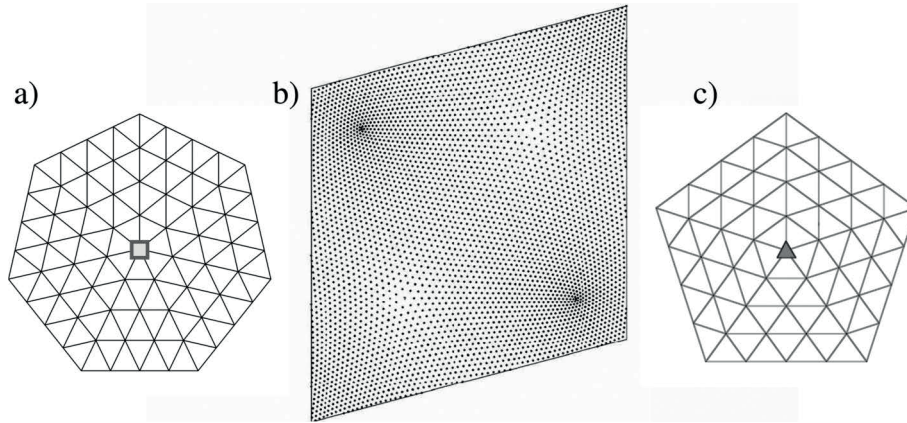


Figure 4.3 – Illustration of disclinations in triangular lattice. Note the center of a disclination in triangular lattice is either a 5- or 7-coordinate position. The formation of free disclinations can be viewed as dissociation of a 5-7 pair. The figures are reproduced from Ref. [1].

A pair of dislocations can dissociate upon excitation, and when far enough apart from each other, individual dislocations will form. Similarly, a dislocation, *i.e.* a 5-7 defect pair, can further dissociate into individual 5 and 7 coordinate sites, leading to another type of topological

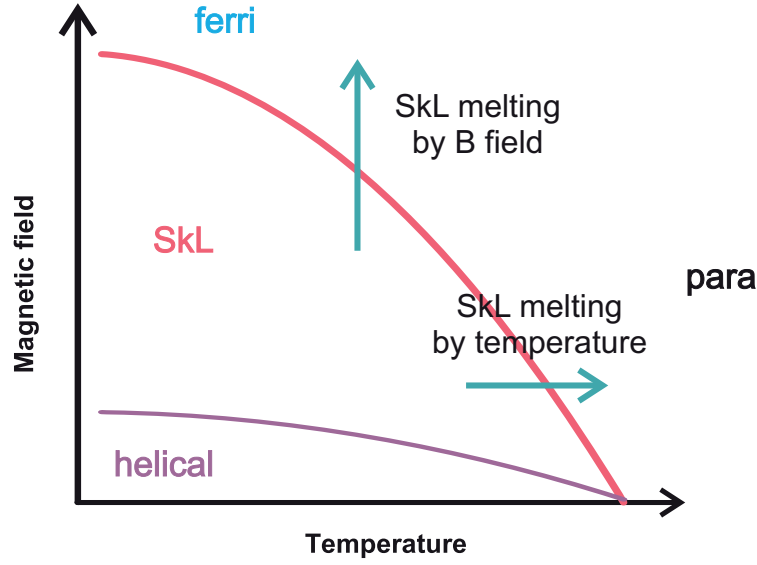


Figure 4.4 – Illustration of SkL melting induced by magnetic field and temperature respectively.

defects known as disclinations, as shown in Fig. 4.3. Rotations, rather than displacements in the case of dislocations, are needed to restore the regular lattice after the similar cutting process.

The two-step scheme of forming and dissociation of the two types of topological defects gives the basic concept of the KTHNY melting mechanism. As the thermal excitation increase, there will be firstly pairs of dislocations, then they dissociate into single ones. At this stage, the translational order is broken but the orientational order still preserves. This phase is called the hexatic phase, characterized by an algebraic decay of the orientational correlation function and an exponential decay of the translational correlation function. Further dissociation of dislocations into individual disclinations will finally break the orientational order, leading to the liquid phase, where both correlation functions decay exponentially.

Besides the thermal excitation term  $k_B T$  purely induced by finite temperature, other terms in the free energy, such as magnetic field  $-\mathbf{B} \cdot \mathbf{M}$  in the case of SkL, can also induce the phase transition with temperature to be fixed. The two melting procedures are illustrated in Fig. 4.4. I successfully melted the SkL through the two step process by tuning the magnetic field, and quantitative characterization of the correlation functions demonstrates that it is indeed a KTHNY type of phase transition.

## 4.2 Experiments and results

Single crystal  $\text{Cu}_2\text{OSeO}_3$  was aligned and cut into a cuboid with the main plane of the sample is along  $[1\bar{1}0]$  direction. Then the sample was mechanically polished down to the thickness of about  $20\mu\text{m}$ . Focused ion beam (FIB) technique was then adopted to further mill a tiny

window on the sample down to about 120nm. Since the compound is insulating, a 6nm layer of amorphous carbon was deposited onto the sample to avoid charging effect by electron beam radiation.

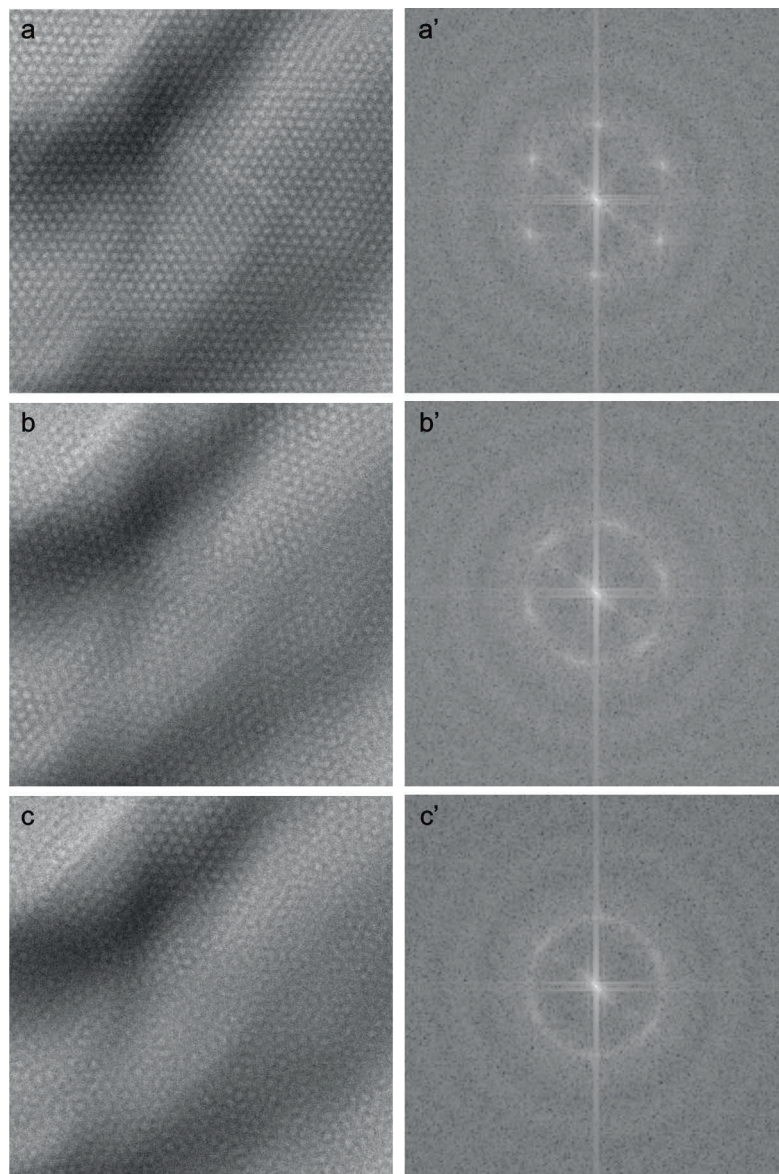


Figure 4.5 – Magnetic field induced melting process: **a.** - **c.** real space images with increasing magnetic fields, **a'.** - **c'.** corresponding FFT

A Gatan liquid helium TEM holder was used to cool the sample down below the magnetic order temperature. After zero field cooling, the sample temperature was maintained at about 19K. Magnetic field was tuned carefully so that the SkL phase showed up just after the helical to SkL phase transition. Then the magnetic field was increased step by step to melt the SkL and LTEM images were acquired at each magnetic field. For the data shown below, the specific magnetic fields were -887Oe, -1076Oe and -1140Oe for for the crystal phase, the hexatic phase



and the liquid phase respectively.

Fig. 4.5 shows the real space images of SkL at different magnetic fields and their corresponding FFT. At low magnetic field, the SkL is a well defined triangular lattice, and the FFT are six sharp Bragg peaks somposing a regular hexagon.

Increasing the magnetic field push the system into the hexatic phase where long range translational order is broken. To see this, one can draw an arbitrary line along two neighbouring skyrmions, after a short distance (several lattice spaces), the periodicity disappear. Note that there is no true long range translational order in 2D lattices at finite temperature, thus if one draws a line in the crystal phase, after long enough distance, the variance to the periodicity can also be observed, which is seen clearly in the quantitative analysis in the next section. However, the orientational symmetry still preserves in the hexatic phase, so that most sites are each surrounded by a regular hexagon. Reflecting on the FFT, there are still six separated features, but sharp spots change into arcs.

The SkL will end up into an isotropic state when further increasing the magnetic field. In this state, even the orientational order was broken, and thus various numbers of neighbouring skyrmions for each site can be observed. Only the average distance among skyrmions remained nearly the same, since it is determined solely by the relative scales of the exchange interaction and the DM interaction, which are both slowly changing quantities as a function of magnetic field. As a result, its FFT is also isotropic, as can be seen in Fig. 4.5, a full circle.

Further increasing of the magnetic field led to the spin polarized phase, which showed no magnetic contrast in our LTEM experiments since there is no in-plane component of the magnetic moments.

### 4.3 Quantitative analysis

To further understand the melting process of SkL in real space and real time, quantitative analysis is carried out. The analysis is based on the identification of skyrmion positions using the same process mentioned in Ch. 3 (technical details can be found in App. B). Then various correlation functions are calculated.

#### 4.3.1 Pair correlation function

The pair correlation function [69] characterizes the possibility of finding a particle at a given distance from a reference point, thus it reflects the density correlation of the assembly of

particles. The definition can be started from the density of a N-particle system:

$$\rho(\vec{r}) = \sum_{j=1}^N \delta(\vec{r} - \vec{r}_j) \quad (4.1)$$

Then the density-density autocorrelation function is:

$$C(\vec{r}) = \langle \rho(\vec{r}_i) \rho(\vec{r}_i + \vec{r}) \rangle_i \quad (4.2)$$

where  $\rho(\vec{r}_i) = \sum_{j=1}^N \delta(\vec{r}_i - \vec{r}_j) = 1$  and  $\rho(\vec{r}_i + \vec{r}) = \sum_{j=1}^N \delta(\vec{r}_i + \vec{r} - \vec{r}_j) = \sum_{j=1}^N \delta(\vec{r} - \vec{r}_{ij})$ , and  $\langle \rangle_i$  means averaging over  $i$ . Therefore,

$$C(\vec{r}) = \langle \rho(\vec{r}_i) \rho(\vec{r}_i + \vec{r}) \rangle_i = \left\langle \sum_{j=1}^N \delta(\vec{r} - \vec{r}_{ij}) \right\rangle_i = \frac{1}{N} \sum_{i=1}^N \sum_{j=1}^N \delta(\vec{r} - \vec{r}_{ij}) \quad (4.3)$$

To make this autocorrelation function to be the possibility of finding a particle at a displacement  $\vec{r}$  from any reference point  $\vec{r}_i$ , we need to normalize  $C(\vec{r})$  by the average density of the system  $\rho_0 = N/V$  where  $V$  is the volume of the system. Thus we have:

$$c(\vec{r}) = \frac{C(\vec{r})}{\rho_0} = \frac{V}{N^2} \sum_{i=1}^N \sum_{j=1}^N \delta(\vec{r} - \vec{r}_{ij}) \quad (4.4)$$

Averaging  $c(\vec{r})$  over angle can convert the correlation function's dependence from displacement, a vector, to distance, a scalar, as  $N_r(r) = \langle c(\vec{r}) \rangle_{angle}$ . Finally, normalizing  $N_r(r)$  over the volume of the spherical shell gives the pair correlation function:

$$g(r) = \frac{N_r}{4\pi r^2 \Delta r} = \frac{1}{4\pi N r^2 \rho_0} \sum_{j=1}^N \sum_{i=1, i \neq j}^N \delta(r - r_{ij}) = \frac{1}{2\pi N r^2 \rho_0} \sum_{j=1}^N \sum_{i>j}^N \delta(r - r_{ij}) \quad (4.5)$$

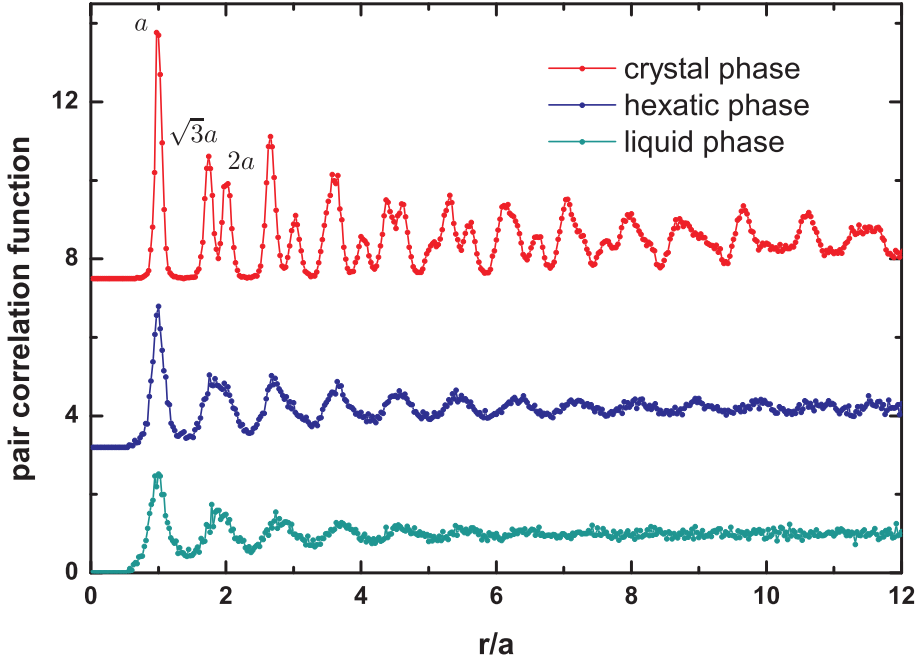


Figure 4.6 – Pair correlation functions of different SkL phases.  $a$  is the lattice constant in the corresponding phases defined at the position of the first peaks, specifically, crystal phase  $a = 76.0\text{nm}$ , hexatic phase  $a = 80.3\text{nm}$  and liquid phase  $a = 82.5\text{nm}$ . The curves are shifted vertically for clarity.

In our 2D case, the "spherical shell" is  $2\pi r\Delta r$ , and thus the correlation function is:

$$g(r) = \frac{1}{\pi N r \rho_0} \sum_{j=1}^N \sum_{i>j}^N \delta(r - r_{ij}) \quad (4.6)$$

The calculated results of  $g(r)$  at different phases are shown in Fig. 4.6

In the crystal phase, one can see clearly sharp peaks at well defined position corresponding to the long range order of the triangular lattice, as labelled for the first few positions. These peaks can be seen up to the maximum distance for the calculation. However, in the hexatic phase, at a finite distance, about  $12a$ , peaks previously exhibited in the crystal phase fade out. Moreover, peaks with close distances, *e.g.* at  $\sqrt{3}a$  and at  $2a$ , tend to merge into broad bumps. Both phenomena imply the loss of long range order. When the system further goes into the isotropic liquid phase, the cutoff for peaks is at even shorter distance, about  $8a$ , and peaks become more broad, showing further loss of long range order.

Note that here, a relative unit  $r/a$  is used for distance, and  $a$  is defined at the positions the first peaks corresponding to the nearest neighbouring distances in each phase, so they are actually different, that is,  $a = 76.0\text{nm}$  for the crystal phase,  $a = 80.3\text{nm}$  for the hexatic phase



and  $a = 82.5\text{nm}$  for the liquid phase. This implies a change in the lattice constant during the melting process. It has been reported that in Co-Zn-Mn system, the lattice spacing increase with increasing magnetic field[35].

#### 4.3.2 Structure factor

From the pair correlation function, we can get the structure factor, or vise versa[70]. Firstly, the scattered wave, either photon, electron or neutron, by the sample is the sum of waves scattered by each particle in the system:

$$\Psi_s(\vec{Q}) = \sum_{\alpha=1}^N f_{\alpha} \exp(-i\vec{Q} \cdot \vec{r}_{\alpha}) \quad (4.7)$$

where  $\vec{Q}$  is the scattering vector in the reciprocal space,  $\vec{r}$  is the position of the  $i^{th}$  particle in the real space, and  $f_i$  is its scattering form factor.

The intensity of the scattered wave, which is an observable in experiments, is:

$$I(\vec{Q}) = \Psi_s(\vec{Q}) \cdot \Psi_s^*(\vec{Q}) = \sum_{\alpha=1}^N \sum_{\beta=1}^N f_{\alpha} f_{\beta} \exp(-i\vec{Q} \cdot (\vec{r}_{\alpha} - \vec{r}_{\beta})) \quad (4.8)$$

If again averaged over spherical shell, then one get:

$$I(Q) = \sum_{\alpha=1}^N \sum_{\beta=1}^N f_{\alpha} f_{\beta} \frac{\sin(Qr_{\alpha\beta})}{Qr_{\alpha\beta}} \quad (4.9)$$

Thus the structure factor is obtained by dividing the form factor:

$$S(Q) = \frac{I(Q)}{\sum_{\alpha=1}^N f_{\alpha}^2} = 1 + \frac{2}{\sum_{\alpha=1}^N f_{\alpha}^2} \sum_{\alpha=1}^N \sum_{\beta < \alpha}^N f_{\alpha} f_{\beta} \frac{\sin(Qr_{\alpha\beta})}{Qr_{\alpha\beta}} \quad (4.10)$$

For a system consisting of identical particles, we have:

$$S(Q) = 1 + \frac{2}{N} \sum_{\alpha=1}^N \sum_{\beta<\alpha}^N \frac{\sin(Qr_{\alpha\beta})}{Q_{\alpha\beta}} \quad (4.11)$$

Insert the expression for pair correlation function Eq. 4.5, one gets:

$$S(Q) = 1 + \int_0^\infty 4\pi r^2 g(r) \frac{\sin(Qr_{\alpha\beta})}{Q_{\alpha\beta}} dr \quad (4.12)$$

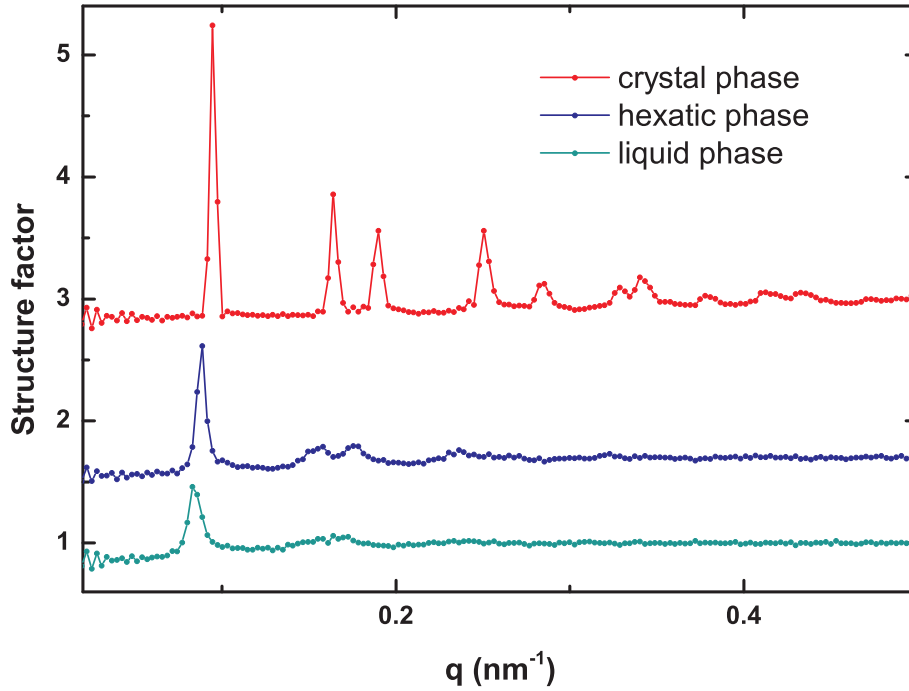


Figure 4.7 – Structure factors revealed from the pair correlation functions for all three phases. Note that different from a relative unit  $r/a$  in Fig. 4.6, an absolute unit  $nm^{-1}$  is used here.

However, in our 2D system, the "spherical" averaging of the structure factor will not end up in a simple function, but contains the zero order Bessel function of the first kind:

$$S(Q) = 1 + \frac{2}{N} \sum_{\alpha=1}^N \sum_{\beta<\alpha}^N \frac{1}{2\pi} \int_0^{2\pi} \exp(-iqr_{\alpha\beta} \cos\theta) d\theta \quad (4.13)$$

and thus one should insert 2D pair correlation function Eq. 4.6, resulting in the following form:

$$S(Q) = 1 + \int_0^\infty r \rho_0 g(r) \left( \int_0^{2\pi} \exp(-iqr \cos \theta) d\theta \right) dr \quad (4.14)$$

From Eq. 4.12, one can see that  $S(Q)$  is the Fourier transform of  $g(r)$ , thus the finite scale in the calculation will cause oscillating artifacts with the period  $T = 2\pi/R_{max}$ . A damping function  $W(r)$  can be multiplied in Eq. 4.14 to reduce the effectL:

$$W(r) = \frac{\sin(\frac{rT}{2})}{\frac{rT}{2}} = \frac{\sin(\frac{\pi r}{R_{max}})}{\frac{\pi r}{R_{max}}} \quad (4.15)$$

Then the final expression I used to calculate the structure factor is:

$$S(Q) = 1 + \int_0^\infty r \rho_0 g(r) \left( \int_0^{2\pi} \exp(-iqr \cos \theta) d\theta \right) W(r) dr \quad (4.16)$$

The derived structure factors for different phases are shown in Fig. 4.7. The loss of long range order in the melting process can be see more clearly here. In the crystal phase, many peaks show up to high spacial frequencies, implying a well organised periodic structure. In the hexatic phase, besides the main peak corresponding to the nearest neighbouring lattice spacing, weak features can also be seen in higher spacial frequencies, which become vanishing in the liquid phase. Even for the main peaks in three phases, the intensities become weaker and weaker upon melting.

### 4.3.3 Orientational and translational correlation functions

There are two order parameters that can be used to characterize the symmetry of an arrangement of particles, the translational and orientational order parameters  $\Psi_k(r)$  and  $\Psi_6(r)$ , and they are defined as the following[65]:

$$\begin{aligned} \Psi_k(r) &= e^{-i\mathbf{k}\cdot\mathbf{r}} \\ \Psi_6(r) &= \frac{1}{N_{nn}} \sum_{j=1}^{N_{nn}} e^{i6\theta_j(r)} \end{aligned} \quad (4.17)$$

where  $\mathbf{k}$  is one of the main reciprocal lattice vectors and  $N_{nn}$  is number of neighbouring

particles around the reference particle located at  $R = r$ .

Correlation functions of these local order parameters give a good description of the melting phase transition since they behave quite differently in different phases. Let's first define the spatial orientational and translational correlation functions[65]:

$$\begin{aligned} G_6(r) &= \langle \Psi_6(r) \Psi_6^*(0) \rangle = \frac{1}{N_r} \sum_{i,j}^{N_r} \Psi_6(r_i) \Psi_6^*(r_j) \\ G_k(r) &= \langle \Psi_k(r) \Psi_k^*(0) \rangle = \frac{1}{6} \sum_{l=1}^6 \frac{1}{N_r} \sum_{i,j}^{N_r} \Psi_{k_l}(r_i) \Psi_{k_l}^*(r_j) \end{aligned} \quad (4.18)$$

where  $N_r$  is the number of particles separating  $r$  away from each other.

Since there is no true long range order in 2D lattice, one would expect an algebraic decay of  $G_k(r)$  in the crystal phase  $G_k(r) \propto r^{-\eta_k}$  as shown in Ref. [62]. Theoretically, the critical value for the decay index  $\eta_k$  is  $\frac{1}{3}$ , i.e.  $\eta_k(B \rightarrow B_H) = \frac{1}{3}$ [67]. After the phase transition to the hexatic phase will appear the exponential decay  $G_k(r) \propto e^{-\frac{r}{\xi_k}}$  [61] due to the lose of the translational long range order; so does  $G_k(r)$  for the liquid phase. Here  $\xi_k$  is the translational correlation length.

The behavior is much more complicated for  $G_6(r)$ . In the crystal phase, it will keep constant close to 1, showing long range orientational order. After getting into the hexatic phase, the order starts to break and  $G_6(r)$  will decay algebraically,  $G_6(r) \propto r^{-\eta_6}$ , until reaching the decay index  $\eta_6$  reaches the critical value  $\eta_6(B \rightarrow B_L) = \frac{1}{4}$  given by the KTHNY theory. In the liquid phase,  $G_6(r)$  again has an exponentially decay behavior,  $G_6(r) \propto e^{-\frac{r}{\xi_6}}$ , with  $\xi_6$  to be the orientational correlation length.

Fig. 4.8 and Fig. 4.9 show respectively the translational and orientational correlation functions for all the three phases. Dashed brown straight lines are guides for the eye showing algebraic decay with exponent  $-\frac{1}{3}$  in translational and  $-\frac{1}{4}$  in orientational correlation functions respectively. Exponential decay behavior are also illustrated respectively by dashed violet curves. These results well demonstrate the magnetic field induced melting of the SkL is indeed a two-step process from the (quasi-) long range ordered crystal phase to the hexatic phase with breaking translational order while keeping the long range orientational order and finally to the isotropic liquid phase.

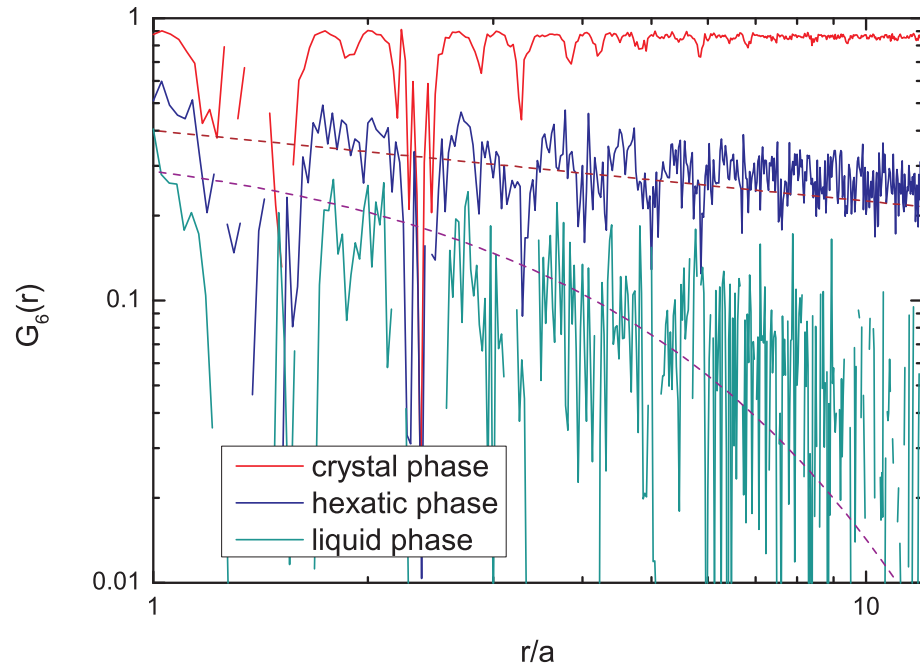


Figure 4.8 – Orientational correlation function  $G_6(r)$  of different phases. Long range order, quasi-long range order and disorder can be clearly seen respectively in crystal, hexatic and liquid phases.

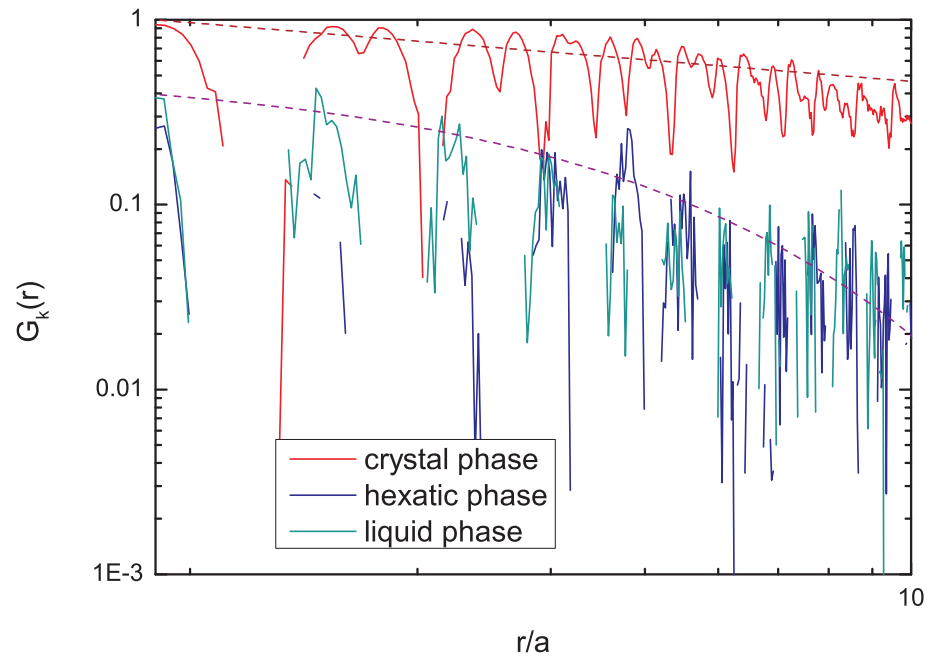


Figure 4.9 – Translational correlation function  $G_k(r)$  of different phases. Only quasi-long range order can be seen in the crystal phase, and exponential decay happens from the hexatic phase, implying no long range order exists anymore.

### 4.4 Discussions

A better understanding of the melting of the SkL should be based on a better understanding of the SkL. As introduced in Ch. 1, in the mean field consideration, the fluctuation induced order by disorder picks out the SkL in some certain range in the phase diagram as the preferred phase in the 3D case, while in the 2D case geometric constrains, and the hence demagnetic field, make the SkL phase energetically more favorable throughout the regime previously belonging to conical phase in the phase diagram. In the microscopic picture, the long range Coulomb repulsive interactions[71] among skyrmions make the triangular SkL as the ground state when the skyrmion density is low. It has also been predicted theoretically[13] that there is short range Néel type magnetic interactions among skyrmions. This interaction will lead to a square lattice on which the Néel order can be achieved while in the triangular lattice it will be frustrated. Due to the short range feature, however, the magnetic interaction can only be apparent when the skyrmion density is high enough. Experimental evidence for a square lattice was reported by T. Tanigaki *et al.*[72] in MnGe thin film in which the observed square SkL showed a lattice spacing of about 3nm, significantly smaller than that observed in other SkL hosting compounds showing much larger SkL lattice spacing (*e.g.* about 60nm in Cu<sub>2</sub>OSeO<sub>3</sub>). A. G. Green and co-workers[14] calculated the classical phonon spectrum of triangular SkL and they found 4 modes: two of them are identical to those in the electronic Wigner crystal and the other two, very stiff, represent the fluctuations of the size of skyrmions.

According to the KTHNY theory, the topological defects mediated melting process contains two second order phase transitions, as demonstrated extensively in literature and also by the results shown here. However, a first order phase transition from the crystal phase directly to the liquid phase was also theoretically proposed[14] and was experimentally evidenced[73]. In order to further understanding the magnetic field induced SkL melting in Cu<sub>2</sub>OSeO<sub>3</sub>, the specific heat investigation should be the next important direction.

One should note that even in the bulk sample, the SkL is still two dimensional, with the skyrmion plates in 2D samples changing to skyrmion rods in 3D samples[74]. Thus it can be very interesting whether the SkL in bulk samples also undergo similar melting transition. In a brief discussion, my supervisor Prof. H. Rønnow pointed out that the mobility of skyrmions in bulk SkL should be much smaller than that of the thin film SkL due to much stronger pinning by the underlying atomic lattice; our neutron experiments, on the other hand, have not shown yet any evidence on magnetic field induced melting of the SkL in bulk samples. More detailed investigations are highly demanded in this interesting topic.

Although here I only reported the magnetic field induced melting of the SkL in Cu<sub>2</sub>OSeO<sub>3</sub>, it should be expected to happen in other SkL hosts. Thermal melting by temperature can be also a very important research direction. Unique for Cu<sub>2</sub>OSeO<sub>3</sub> which has strong ME coupling, electric field may lead to the melting of the SkL as well, but the specific process may exhibit very special features.

Most knowledge on the SkL until now was obtained in the classical regime where the quantum

fluctuations are assumed negligible. Moreover, the coupling between the spin waves and the phonons of the SkL has not been fully considered yet. One would expect it is highly possible that interesting emergent properties exhibit as investigations get further into those regimes.

Based on the above discussion, one can see that detailed investigations on the melting process of the SkL from various aspects can really open a much wider view and a much deeper insight on the classical, and maybe quantum, properties on this periodic structures formed by topologically non-trivial magnetic quasi-particles.

## **4.5 Conclusion**

Magnetic field induced melting (and vice versa condensation) of the SkL in  $\text{Cu}_2\text{OSeO}_3$  was observed and analyzed quantitatively. A 2-step melting process happens upon increasing the magnetic field: first from the (near perfect) crystal SkL to the so-called hexatic phase, then from the hexatic phase to the isotropic liquid phase.

Starting from the identification of positions of skyrmions in all phases, various correlation functions, including the pair correlation function, the orientational and the translational correlation functions, were calculated. The results of which all revealed that in the first step of melting the translational symmetry of the lattice breaks while the orientational symmetry preserves; and the latter breaks in the second step of melting.

All these observations and the consequent analysis demonstrate that the magnetic field induced melting of the SkL can be well described by the KTHNY theory. This means the SkL, formed by magnetic skyrmions as quasi-particles, can still be understood in the classical 2D lattice scenario, making things much simplified. On the other hand, however, unique properties beyond the general 2D lattice description of SkL may be discovered if theories combine the phonon and spin wave considerations.





## 5 SkL dynamics induced by electric field

Due to its magnetoelectric coupling,  $\text{Cu}_2\text{OSeO}_3$  possesses emergent electric polarization in the skyrmion phase, meaning the manipulation of skyrmions can be achieved by application of electric field, as already shown in Ch. 2 with the SANS results that the SkL in  $\text{Cu}_2\text{OSeO}_3$  can be rotated by electric field. The lack of the real space information, however, leaves many questions unsolved, for example, whether the SkL rotates as a whole or it divides into domains?

On the other hand, new  $-\mathbf{P} \cdot \mathbf{E}$  term in the free energy induced by the coupling of external electric field and the emergent electric polarization in  $\text{Cu}_2\text{OSeO}_3$  may also manifest itself in other aspect, and one of such possibilities is the shift of the phase boundaries between various magnetic phases. An extremely interesting consequence of that will be the creation of skyrmions out of the ground state helical phase, rather than from the high energy spin polarized phase.

Creation and manipulation of skyrmions are the basis of "skyrmionic" devices. Manipulation of skyrmions has been achieved initially, *e.g.* by external electric field, electric current, as well as thermal gradient. While creating skyrmions by electric current was reported[75], creating skyrmions via electric field is still highly demanded, since, firstly it will adapt the current field effect transistor (FET) based electronic technology and second very low energy dissipation. The only reported approach so far is conducted on a hetero tri-layer interfacial skyrmion system, in which the Néel type skyrmions can be created and annihilated respectively out of the underlying ferromagnetic background by the application of a tip electric field in different directions[76]. Theories[77, 78] are massively proposed to show that skyrmions can be created by a local electric field in magnetoelectrically coupled chiral magnet  $\text{Cu}_2\text{OSeO}_3$ , yet again from ferromagnetic state.

Lorentz transmission electron microscopy (LTEM) is a very suitable tool for the observation and manipulation of skyrmions and has already been widely used for studying spin textures with in-plane long wave length modulation. What makes it particularly exciting is the possibility of *in situ* tuning of electric field, magnetic field and temperature, while observing the system in real space and real time. Furthermore, the local nature of LTEM further offers the

opportunity to investigate the effect of defects such as domain boundaries and dislocations. In this chapter, I will report my experimental realization in  $\text{Cu}_2\text{OSeO}_3$  of the manipulation of the SkL, and the creation of skyrmions from the helical phase by *in situ* application of electric field in LTEM. Direct quantitative analysis, including statistics on the number of skyrmions, realized via a newly developed image processing technique, fully demonstrates correlation between application of electric field and rotation of the SkL and the creation of skyrmions, respectively.

### 5.1 Experiments

I chose a sample geometry of  $\mathbf{B} \parallel [1\bar{1}0]$  and  $\mathbf{E} \parallel [11\bar{1}]$ , which is the same as adopted in the neutron experiment. The spontaneous electric polarization of the SkL is then along  $[00\bar{1}]$ , which is inside the sample plane, and will couple with the applied electric field in both positive and negative directions, as illustrated in Fig. 5.1a.

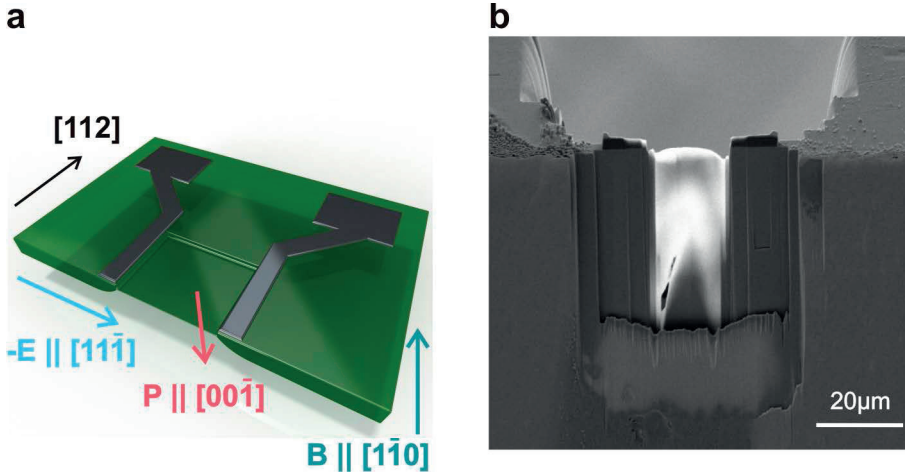


Figure 5.1 – **a.** Sample geometry. The main sample plane was chosen to be  $[1\bar{1}0]$  so that the spontaneous polarization of the SkL, along  $[00\bar{1}]$ , will be in the same plane with the applied electric field along  $[11\bar{1}]$ . The thickness of the sample lamella is about 100nm **b.** SEM image of the sample.

For the E-field induced rotation, the sample temperature was fixed at around 21K and the magnetic field was -651Oe, well inside the SkL phase according to the reported phase diagram for the thin slab  $\text{Cu}_2\text{OSeO}_3$  samples. Then the E-field was applied, and the LTEM image series were recorded at the same time.

For the E-field creation experiments, at a fixed temperature, the magnetic field was first adjusted so that the sample was within the helical phase but very close to the phase boundary between helical phase and the skyrmion phase. Then electric fields were applied to the sample and LTEM images were recorded successively.

The time intervals of the recorded image series varied from 0.3s to as fast as 0.04s. Usually one

image series contains more than 1000 frames.

## 5.2 E-field induced rotation of SkL

Initially, the experiment was carried out by manually changing the electric field from +1.78kV/mm to -1.78kV/mm back and forth while real space image series of LTEM was being recorded. Fig. 5.2 shows the typical static images of the SkL taken out from the image series and their corresponding FFTs under different electric fields respectively. LoG filtering was applied for better display effect. Since the application of the electric field will shift the TEM image by altering the electron beam, the images were firstly aligned and then a region of a big single domain was selected for clarity, as demonstrated by the FFTs.

Qualitatively, obvious rotation of the SkL can be observed in the real space images, as indicated by lines drawn on the images for guidance. The relative orientations of the SkL in the three images were calculated from their FFTs and the results are shown in Tab. 5.1. Here, the azimuth angle was defined as the averaged angle of fitted centers of all Bragg peaks with respect to the reference position shown in the insert in Fig. 5.2, and positive and negative signs mean rotations clockwise and counter-clockwise respectively.

Table 5.1 – Azimuth angles of the SkL at different electric field. Positive(negative) angle corresponds to clockwise(counter-clockwise) direction.

$U$ (V)	Azimuth angle ( $^{\circ}$ )	difference ( $^{\circ}$ )
+100	$10.83 \pm 3.99$	-
-100	$-14.20 \pm 2.89$	$-25.03 \pm 4.93$
+100	$1.91 \pm 5.17$	$16.11 \pm 5.92$

Note that a concentrated beam was used to thermally depin the SkL from the underlying atomic lattice, similar to what we did in the SANS experiments using oscillating magnetic field. As mentioned in Ch. 2, the thermal effect induced by the electron beam radiation can also rotate the SkL, thus a further demonstration of the electric field induced rotation of SkL is necessary. For this purpose, an electric field scan was carried out and the real space images were continuously recorded.

Again, after the alignment of the whole image series containing 1181 images, a big single domain region was chosen and analyzed and the results were shown in Fig. 5.3. The curve in red shows the azimuth angle of the SkL as a function of relative time and the curve in blue is the corresponding applied electric field. The strong correlation between the electric field and the orientation of the SkL revealed in the statistics then fully demonstrated the ability of electric field to rotate the SkL in magnetoelectric coupling  $\text{Cu}_2\text{OSeO}_3$ .

Note from the angle curve that at the initial period of the application of the electric field when the intensity was low, the orientation of the SkL didn't follow the electric field as it behaved later. Also a drift of the angle towards the negative side can be seen. Both of these give evidence of

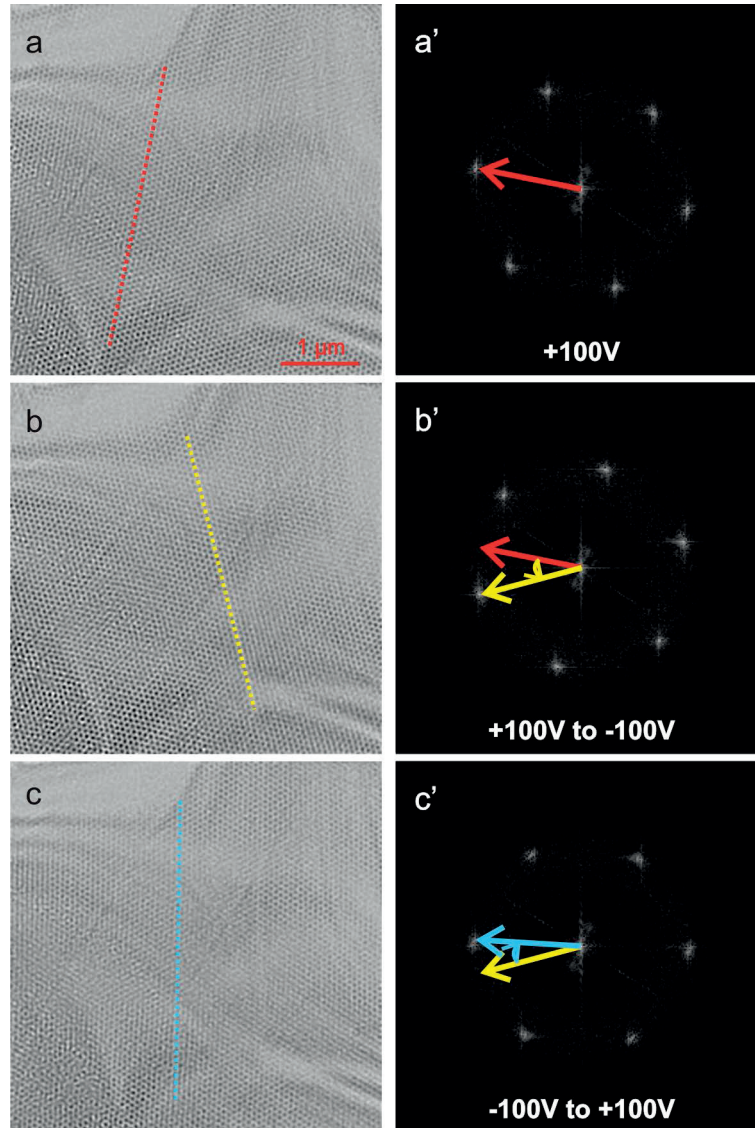


Figure 5.2 – The SkL under **a.** +1.78kV/mm and **b.** -1.78kV/mm. Lines are guide for the eye to indicate the orientation of the SkL.

thermally induced rotation and/or fluctuation of the orientation of the SkL, which emphasizes the necessity of a full scan in the demonstration of the electric field induced SkL rotation.

On the other hand, the system was hardly in equilibrium states during the electric field scan thus a quantitatively analysis like what was done in our SANS experiment cannot be carried out. But my real space investigation of the SkL rotation can still give information that SANS cannot. One such example is *how* the SkL rotates.

For a large single domain SkL, if all the skyrmions rotate in the same pace, *i.e.* the SkL rotates as a whole, then there will be only one rotation axis. This means the skyrmions closer to the

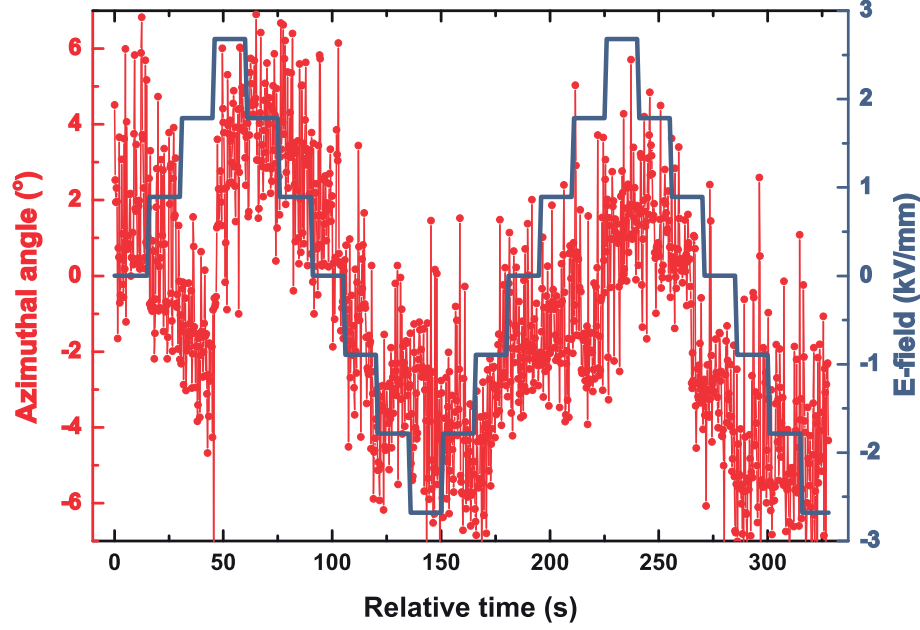


Figure 5.3 – The orientation of the SkL and the electric field as a function of time respectively. Obvious correlation can be immediately seen.

axis will move shorter distances while those further away from the axis will move longer in path. In the limit case, some skyrmions will move a path in the magnitude of the sample's scale in this hypothesis!

Another more realistic hypothesis will be that the SkL splits into multi domains and each domain rotates in its own pace, but after rotation all domains merge again into one single domain. The real space data give evidence to the multi-domain scenario, as shown in Fig. 5.4.

### 5.3 E-field creation and annihilation of skyrmions

Due to the magnetoelectric coupling, there will be spontaneous electric polarization in the magnetically ordered phases, including the helical phase, the skyrmion phase, the conical phase and the ferrimagnetic phase. With properly chosen configuration of the sample orientation, with respect to the magnetic field and the electric field respectively, there will be coupling between the polarization and the electric field, adding a new term  $-\mathbf{P} \cdot \mathbf{E}$  into the free energy. A natural idea then will be to shift the helical-skyrmion phase boundary with the application of electric field. By this means, one can create skyrmions, for example, out of a helical phase background, in sharp contrast to the most commonly theoretically proposed schemes that create skyrmions from a ferromagnetic background.

By using LTEM, I demonstrate this effect in real space and real time. Firstly, a fine adjustment of the sample environment, including the temperature and the magnetic field, was carried out to place the system in a state near the helical - SkL phase boundary but still inside the helical



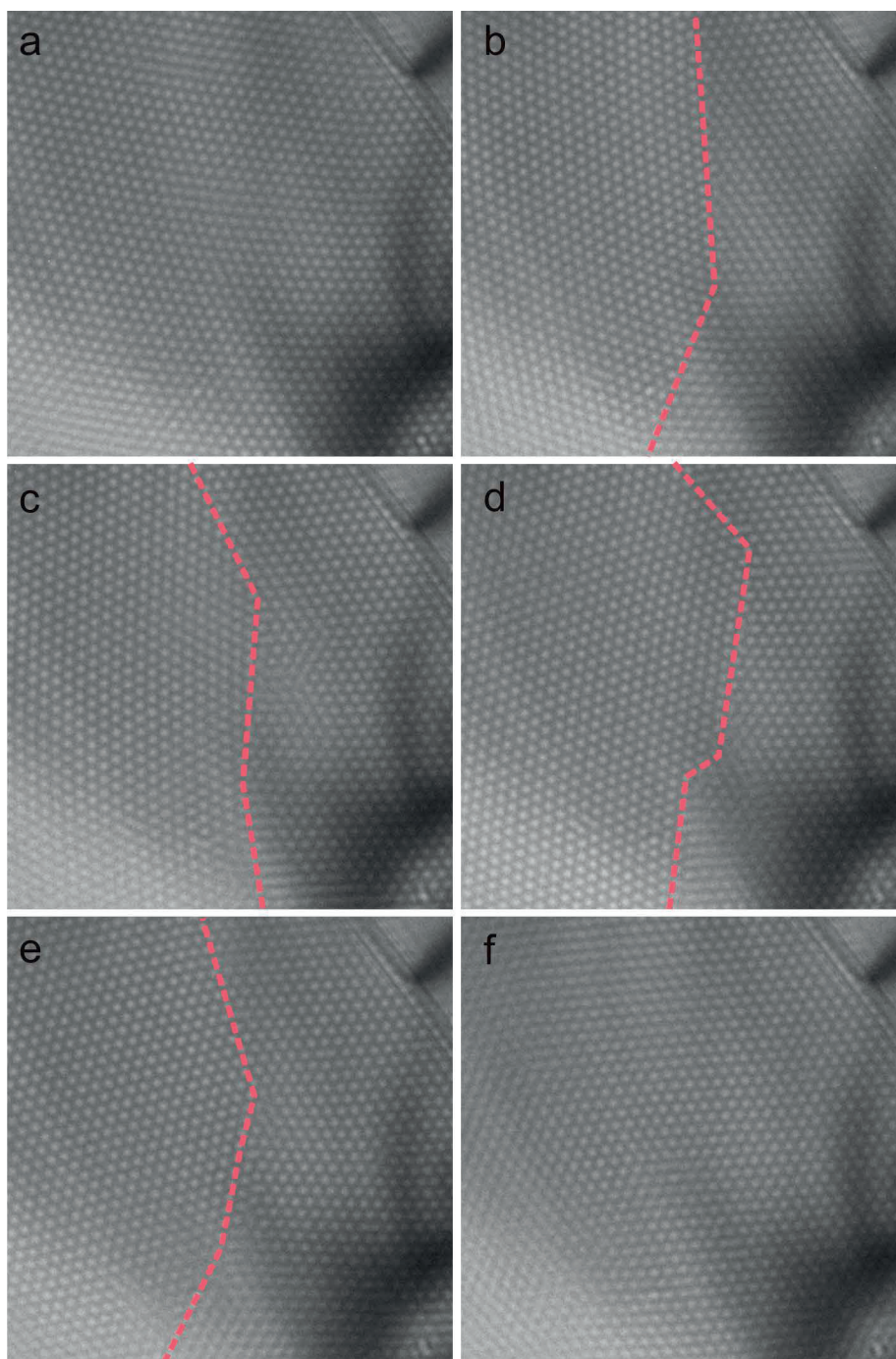


Figure 5.4 – Temporal series images showing the overall rotation of the SkL is achieved by respective rotation of smaller domains.

phase. Specifically, the magnetic field was 254Oe and the temperature was around 24.7K (with a very slight decreasing drift finally down to 24.5K when I stopped recording images), according to literature, in this condition the sample was indeed very close to the helical-SkL

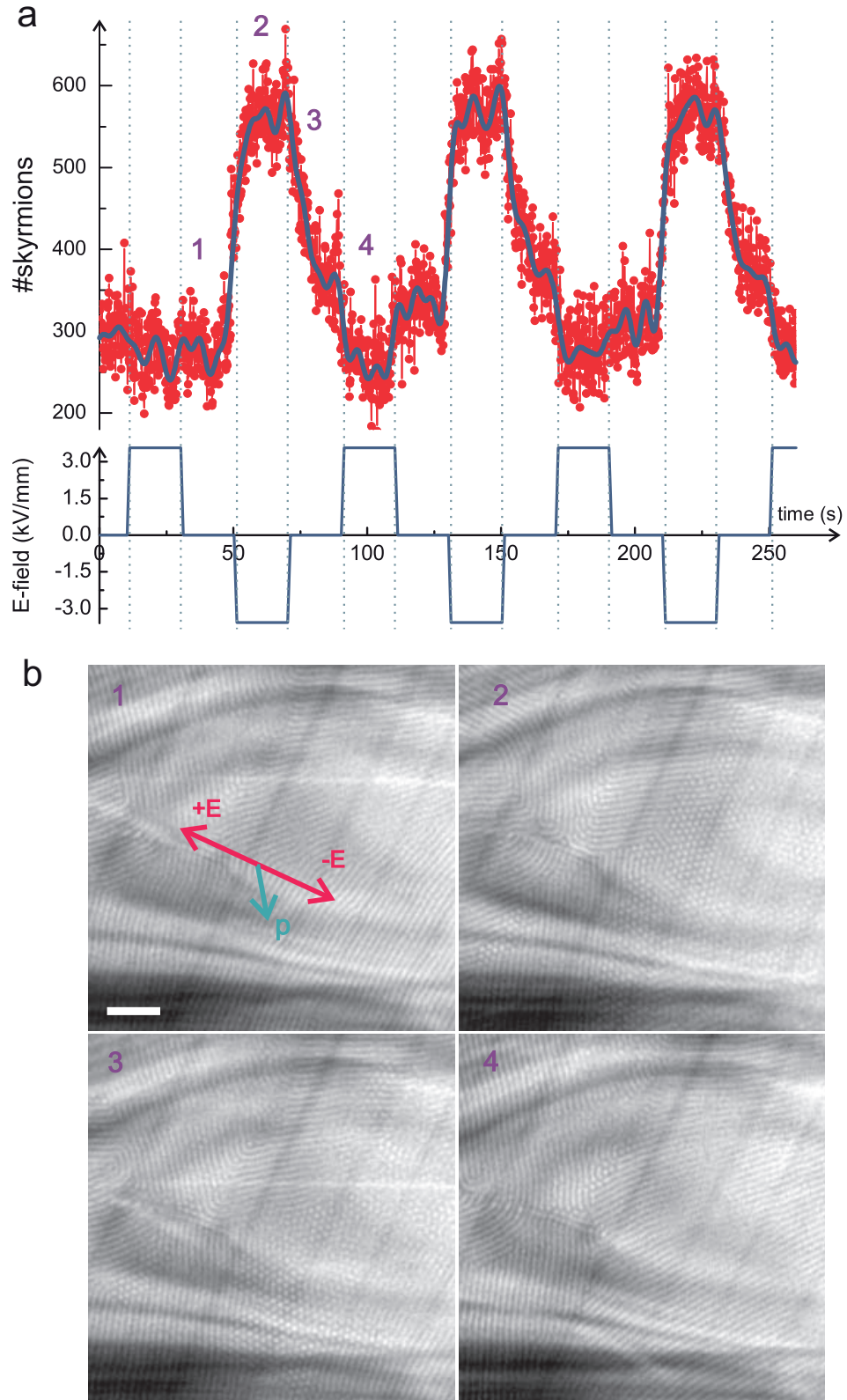


Figure 5.5 – **a.** Statistics of the number of skyrmions and the applied bipolar electric field as a function of time. The blue curve in the upper panel shows the FFT filtering for clarity. **b.** Real space images under 0kV/mm, -3.57kV/mm, 0kV/mm again and +3.57kV/mm, respectively. scale bar 500nm

phase boundary. A typical image in this state is shown in Fig. 5.5b.1, and one can see that the system was in the helical phase with multiple domains propagating in various directions, and just a few skyrmions can be found near the domain boundaries, showing evidence of the proximity to the phase boundary.

Then a sequence of electric field, 0V, +200V (3.57kV/mm) and -200V (-3.57kV/mm), was applied with each field lasting for 20s, as shown in Fig. 5.5a lower panel. Here 200V is the highest value of the voltage source. At the same time, the LTEM images were recorded with a time interval of 0.15s. Fig. 5.5b.2 shows the magnetic texture of the same area with the application of -3.57kV/mm electric field. A large domain of SkL showed up on the right side of the image, demonstrating the creation of SkL by electric field. Note that the helical domains on the left side of the image were also affected by the electric field, changing their orientations, although not converted into SkL. After switching off the field, the created skyrmions gradually disappeared, and the helical domains recovered simultaneously, as shown in Fig. 5.5b.3. Application of +3.57kV/mm electric field did not show any sign of creating skyrmions, only affected were some of the helical domains, for example, the right bottom part of Fig. 5.5b.4 if compared with Fig. 5.5b.1.

The purpose of the application of alternatively positive and negative electric fields (with zero field in between to prepare the system in the same starting point) is to demonstrate that the electric field creation of skyrmions is a mono-polar effect, which will further give strong evidence that the creation of skyrmions is the consequence of electric field. This is in sharp contrast to the situation of skyrmion creation by thermal activation, which is bipolar[34].

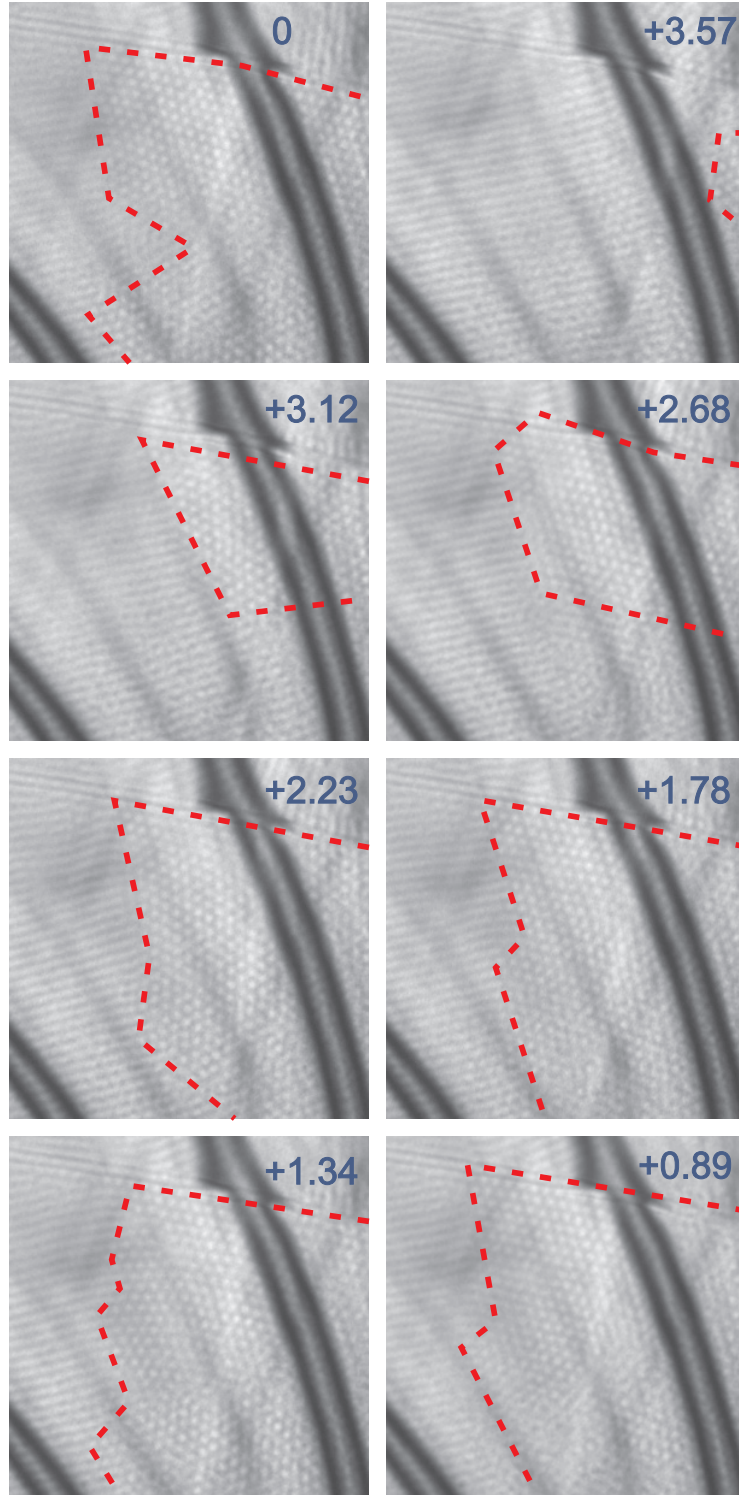
A quantitative statistics of the number of skyrmions in different electric field will give more physical information. To do so, all the images in the series were firstly aligned, then a region of interest was chosen. A window approximately the size of a single skyrmion was used to scan the images filtered by Laplacian of Gaussian (LoG) to identify local minimum, which ideally should be the center of a blob shaped object. However, since one can always find a local minimum inside a window, additional criteria should be adopted to further confirm whether it is a skyrmion. In the specific case here, with stripe shaped helical phase together in the images, the local direction map was calculated with a similar sized window scanning the images, and only those minima found previously that are unparallel with their neighbours are identified as skyrmions. More details of this algorithm, which was inspired by the algorithms used to identify fingerprints, can be found in App. B.

Fig. 5.5a upper panel shows the statistics of the number of skyrmions as function of relative time in all 1800 images recorded in a single series. The number of skyrmions obtained by the aforementioned algorithm at 0kV/mm is about 300, which is much more than the skyrmions that can be counted manually in this condition, as shown in Fig. 5.5b.1. This is because the algorithm identify places where the orientation map change a lot or cannot be accurately calculated as skyrmions. This is definitely a shortage, however, since all the images in the series were acquired in the same condition, the artifacts are almost the same for all the images.



### 5.3 E-field creation and annihilation of skyrmions

Thus it only adds a background to the statistics, without significant influence to the qualitative conclusions.



(to be continued in the next page)

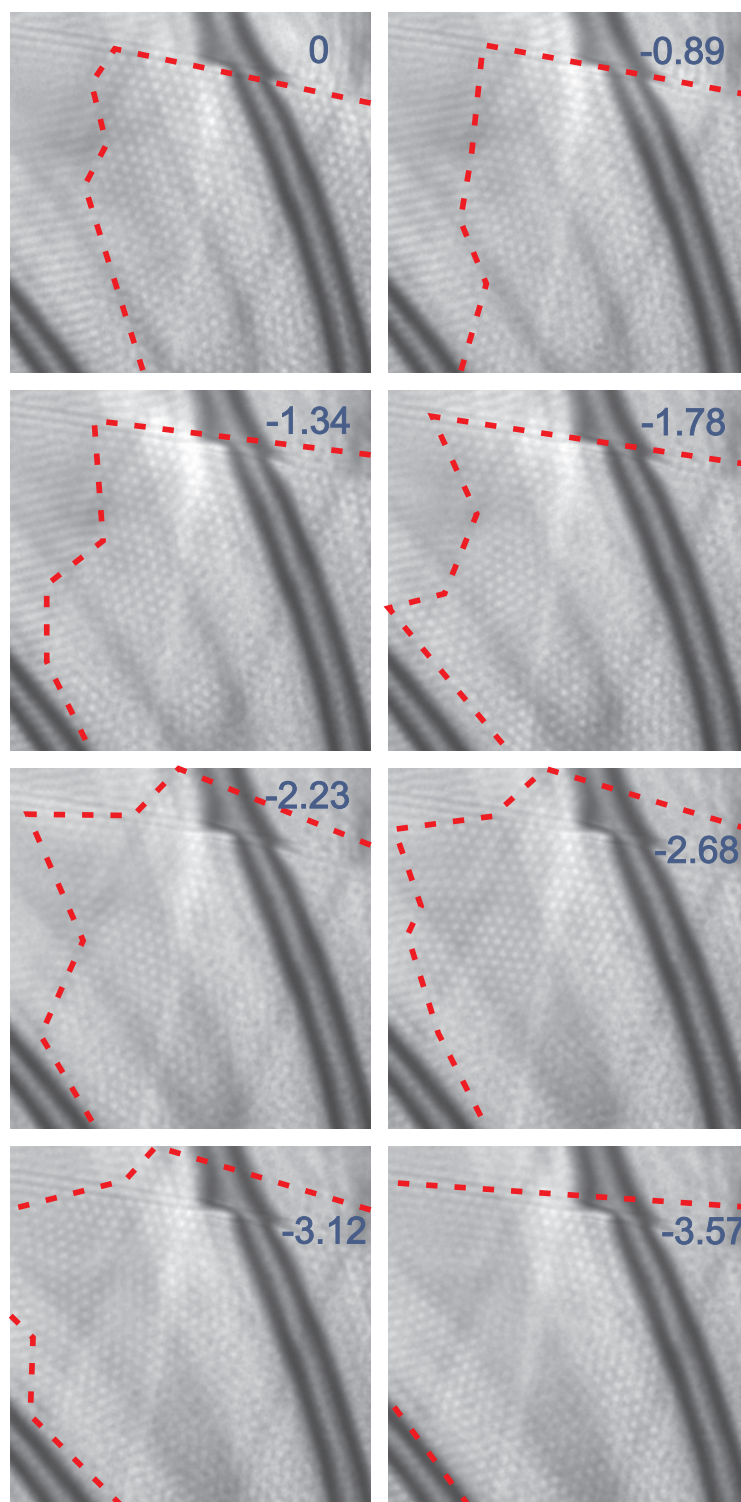


Figure 5.6 – Real space images of the moving of the SkL domain boundary in the helical phase background as a function electric field.

The statistics of the number of skyrmions fully demonstrated that one direction of electric field can create skyrmions from the helical phase. The process started from  $E=0\text{kV/mm}$ , where the numbers of skyrmions were at the level of statistical background explained above. After switching on the electric field to  $E=+3.57\text{kV/mm}$ , no change in the numbers of skyrmions was observed. Then the change of the polarity of the electric field,  $E=-3.57\text{kV/mm}$ , led to an abrupt increase of the number of skyrmions, and during the lasting time of this field value, the numbers of skyrmions were stable, forming a plateau. Switching off the electric field resulted in a relaxation of the numbers of the skyrmions gradually down to the background level.

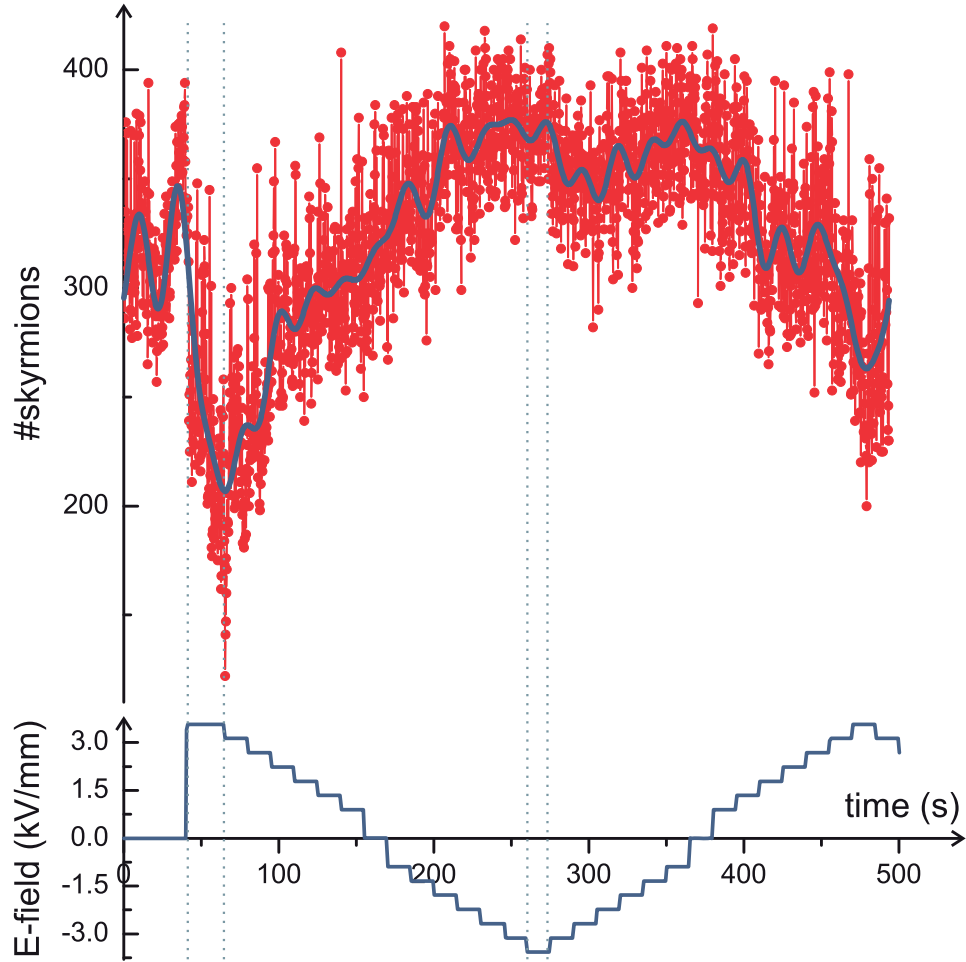


Figure 5.7 – **a.** Statistics of the number of skyrmions. The blue curve shows the FFT filtering for clarity. **b.** The applied bipolar electric field as a function of time.

Qualitative understanding of this phenomena can be achieved if one takes a look at the illustration of the directions of the electric fields as well as the spontaneous polarization of skyrmions shown in Fig. 5.5b.1. Both negative and positive electric fields can couple with the polarization of skyrmions, with the former lower down the free energy while the latter increases the free energy in contrast. Since the sample was set to a condition very close to the helical - SkL phase boundary, the free energy of both phases are almost the same. The

coupling between the negative electric field and the polarization will make the free energy of the SkL phase lower than that of the helical phase, shifting the phase equilibrium so that skyrmions can be created.

More interestingly, since it is a first order phase transition from the helical to the SkL phase, fine tuning of the conditions can lead to the state at which there will be co-existence of helices and skyrmions. Applying electric field in this condition will then achieve the manipulation of the skyrmion domain, as shown in Fig. 5.6. Starting at 0kV/mm, there was already a small but finite SkL domain prepared at 408Oe and 24.7K, as highlighted by the red dashed line. Switching on the electric field to +3.57kV/mm significantly suppressed the scale of the domain, making it shrink to the corner of the field of view. With the decrease of the positive electric field, the scale of the SkL domain recovered correspondingly. After changing into the negative side of the electric field, the SkL domain grew bigger than the starting point. At the largest negative field, -3.57kV/mm, the SkL domain extended even out of the field of view.

The same quantitative statistics was also carried out, and the results are shown in Fig. 5.7. Initially, finite numbers of skyrmions were revealed at 0kV/mm. Then a sharp decrease of the number of skyrmions can be observed exactly at the edge of the highest positive electric field, +3.57kV/mm. Increase of the number of skyrmions corresponds perfectly with the change of the electric field towards the negative side, reaching its peak at the largest negative value, -3.57kV/mm. This phenomenon is reversible, as one can see that changing back of the electric field to the positive side will again suppress the number of skyrmions. Note that the fluctuation of the number of skyrmions near the peak is due to the blurring of the images. Detailed explanation can be found in App. B.

### 5.4 Discussion

Although not yet carried out calculations here in my thesis, one would naturally expect a free energy  $F(E)$  that depends on the E-field to the first order  $F(E) \propto E$ . Only in this form can the mathematical description reflect mono-polar feature of the experimental results. While the first experiments shown here demonstrates more in a qualitative manner the E-field creation/annihilation of skyrmions, the second experiment scanning E-field has the potential to extract quantitative information. The direct measured quantity in this experiment is the number of skyrmions in a certain domain out of the helical phase background, *i.e.* one got the experimental relation of  $N_s^{raw}(E)$ . Since the system was set in a helical-SkL coexisting state, there is a background  $N_{s0}$  at  $E = 0$ kV/mm; also included is a fluctuation term  $\Delta N_s$  induced *e.g.* thermally. Thus we have:

$$N_s(E) = N_s^{raw}(E) - N_{s0} - \Delta N_s \quad (5.1)$$

On the other hand, it is possible to derive the chemical potential of skyrmions  $\mu_s$  as a function of  $N_s$ ,  $\frac{\partial \mu_s}{\partial N_s}$ . Combining the two, one can get:

$$\frac{\partial \mu_s}{\partial E} = \frac{\partial \mu_s}{\partial N_s} \frac{\partial N_s}{\partial E} \quad (5.2)$$

Compared to the free energy, the chemical potential is a measurable quantity. Through this process, one would get a better and quantitative understanding of the thermodynamics of the SkL, especially near the phase boundary, where the mean field theory does not work properly.

One might probably have already noticed that in Fig. 5.5b, the helical domain on the top left of the images was affected by the applied E-field, from straight stripes at 0kV/mm to bent ones at -3.57kV/mm. Combining the *d-p* hybridization ME mechanism and the helical spin configuration give by Eq. 2.3 with  $n = 1$ , there is spontaneous electric polarization in the helical phase, and hence effects induced by E-field can be expected. So far as I know, however, not much work has been down on the ME related effects in the helical phase (or the conical phase which does not show up in thin samples for LTEM investigations). Although topologically trivial, I think through well designed experiments and careful analysis of the data, interesting properties will also be dug out, as evidenced by the data shown here.

Another interesting phenomenon in my experimental results is, in a multi- $\vec{q}$  helical state, the application of the E-field can only create skyrmions in a certain helical domain. This implies a  $\vec{q}$  dependence of the free energy after applying the E-field probably due to the difference in the directions of the ME coupling induced electric polarization. Given that experimentally observed, both by SANS and LTEM, ground state is the multi- $\vec{q}$  state, the preference of skyrmion creation to a certain helical propagation direction (or maybe more precisely a certain range of  $\vec{q}$  directions) makes it possible to engineer the material so that, for example, skyrmions can be easier (or equivalently, more difficult) to be created, or the creation can be limited to a desired position. The material engineering can be artificial defects on the surface of the sample or specially designed magnetic/electric field. I think the realization of this controllable creation of skyrmions can significantly promote the development of skyrmion based spintronic devices.

## 5.5 Conclusion

The magnetoelectric coupling of  $\text{Cu}_2\text{OSeO}_3$  provides a unique way of manipulating and tuning its SkL state. The rotation of the SkL induced by the electric field was demonstrated in the real space and real time, consistent qualitatively very well with our SANS experiments. My study also demonstrates that the rotation is achieved by splitting the SkL into multiple domains and they rotate respectively then form a single large SkL domain in the new energetically favored orientation.

Moreover, the creation and annihilation of skyrmions (SkL) from the helical phase was observed for the first time in the real space and real time. The quantitative analysis exhibits a strong correlation between the application of the negative/positive electric field and the creation/annihilation of skyrmions, which fully demonstrates the role played by the electric field.

For finite domains of SkL in the helical phase, the application of electric was demonstrated capable to control the scale of the SkL domain, implying the technical or even industrial application of skyrmions in *e.g.* next generation magnetic storage.



## 6 Conclusion and outlooks

### 6.1 Conclusion

In summary, this thesis presents, hopefully, a systematic investigation of the SkL in ME coupling compound  $\text{Cu}_2\text{OSeO}_3$ , based on the magnetic and ME properties of bulk crystals and focused on thin film samples investigated by LTEM, from static thermodynamics to dynamics induced by various stimulations including thermal fluctuations and external fields. Specifically:

The magnetization study on single crystal bulk  $\text{Cu}_2\text{OSeO}_3$  samples revealed well consistent properties with those reported in literature, demonstrating high quality of our samples. Self-established magnetoelectric susceptibility ( $dM/dE$ ) measurement provides a direct approach to investigate directly the ME properties not only in  $\text{Cu}_2\text{OSeO}_3$  but also in other systems with ME coupling. Moreover,  $dM/dE$  curves exhibit sharp peaks at the phase boundaries of  $\text{Cu}_2\text{OSeO}_3$ , making it a very powerful tool in the studies of phase transition. Electric field induced rotation of SkL in  $\text{Cu}_2\text{OSeO}_3$  was demonstrated by SANS experiments and a perturbation theory considering magnetic anisotropic energy up to the 6th order was proposed to explain the observation.

Magnetic textures of thin film  $\text{Cu}_2\text{OSeO}_3$  with long modulations were observed and investigated by LTEM, including the helical phase, the SkL phase, the phase transition from the former to the latter induced by magnetic field, and the existence of skyrmions in the helices as defects. Fluctuations of the SkL were also observed, induced by either ambient conditions or by intensive electron beam radiation.

Further, the magnetic field induced melting (and vice versa condensation) of the SkL in  $\text{Cu}_2\text{OSeO}_3$  was observed and analyzed quantitatively. A 2-step melting process happens upon increasing the magnetic field. Quantitative analysis based on various correlation functions, including the pair correlation function, the orientational and the translational correlation functions, all revealed that in the first step of melting the translational symmetry of the lattice breaks while the orientational symmetry preserves; and the latter breaks in the second step



of melting, demonstrating that the magnetic field induced melting of the SkL can be well described by the KTHNY theory.

Finally, ME coupling induced effects in  $\text{Cu}_2\text{OSeO}_3$  were investigated in two aspects. The rotation of the SkL induced by the electric field was demonstrated in the real space and real time, demonstrating that the rotation is achieved by splitting the SkL into multiple domains and they rotate respectively then form a single large SkL domain in the new energetically favored orientation. The creation and annihilation of skyrmions (SkL) from the helical phase was realized for the first time in the real space and real time. quantitative analysis exhibits a strong correlation between the application of the negative/positive electric field and the creation/annihilation of skyrmions, which fully demonstrates the role played by the electric field.

My studies, especially those focused on the emergent properties induced by external fields, are believed to provide deeper insight into the fundamental knowledge of the SkL in  $\text{Cu}_2\text{OSeO}_3$  and to strongly promote the the development of skyrmion based spintronic applications.

## 6.2 Outlooks

### 6.2.1 For fundamental research

Although remaining under very intensive investigations, there are still massive open questions. For example, various proposals have been made to drive skyrmions in a controllable manner, by electric field, by electric current, or by thermal flow and so on, yet few experimental clues has been reported. While current researches focus more on the single particle properties of skyrmions, properties originating from the interactions among skyrmions and between skyrmions and their embedding environments (such as the underlying atomic lattice) should receive more attention.

I would like to emphasize here that properties arising from the periodic potentials, including the magnetic, electric and even topological potentials, lack sufficient notice so far as I know. Similar as the success of the band theory in the atomic lattice, making fully use of the periodicity of SkL may also open a conspicuously new aspect in this research field.

Effective magnetic monopoles in SkL systems can also be extremely interesting, yet more theoretical and experimental efforts are demanded,

### 6.2.2 For application

Race track memories are thought to be the most possible application for skyrmion based techniques for the time being. While the basic conditions needed for their realization, *i.e.* controllable creating, moving and detecting skyrmions, have already been achieved or are approaching, the assembly of all these into one device seems still be challenging. Compared

to the bulk systems in which the skyrmions usually exist far below the room temperature and compose periodic lattices, the interfacial systems seem a more possible candidate. It does not make no sense to expect a prototype of such devices in a very near future.



# A Image processing

Most data shown and analyzed in this thesis are in the form of images, thus various image processing tools were used. All processes were carried out in MATLAB.

## A.1 Image filters

A digitized bitmap image is nothing but a matrix with each element representing the brightness of each pixel for a gray scale image or three matrices of that for a RGB image. In some occasions, the range of those matrix elements need to be normalized for the next steps. In my work, it was done as the following[79]:

$$I_N(i, j) = \begin{cases} M_N + \sqrt{\frac{\sigma_N(I_0(i, j) - M_0)^2}{\sigma_0}} & \text{if } I_0(i, j) > M_0 \\ M_N - \sqrt{\frac{\sigma_N(I_0(i, j) - M_0)^2}{\sigma_0}} & \text{otherwise} \end{cases} \quad (\text{A.1})$$

where  $I_0$  and  $\sigma_0$  are the estimated mean and variance of the original image  $I_0$ , respectively, and  $I_N$  and  $\sigma_N$  are the desired corresponding values for the normalized image  $I_N$ .

Filters are widely used in image processing to achieve various effects. The most important image filters used in this thesis are Gaussian filter and Laplacian of Gaussian (LoG) filter respectively. These two belong to the same type of filters that in principle calculate the convolutions of a kernel matrix  $K$  with the input matrix  $I$ . To be clear but keep the generality, the following is the definition of the convolution operation in 1D:

$$(I * K)[i] = \sum_{n=1}^m K[n] \cdot I[i - j + m/2] \quad (\text{A.2})$$

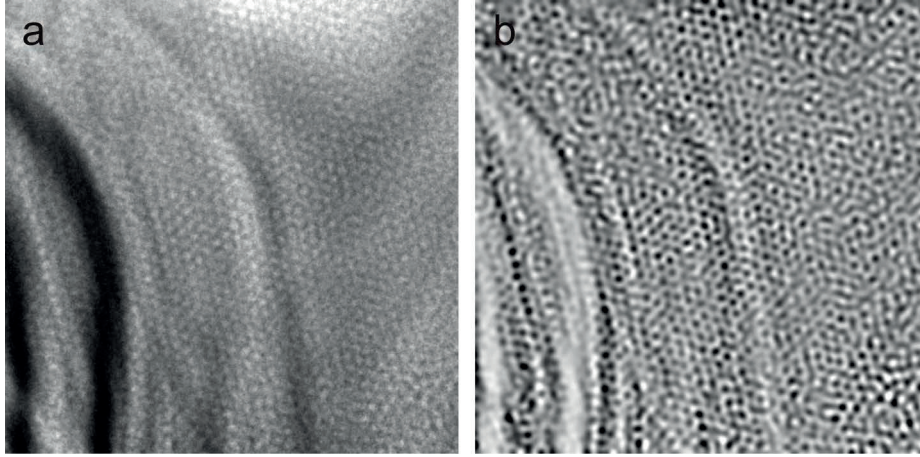


Figure A.1 – **a.** Raw image of skyrmions. **b.** After LoG filtering. One can clearly see that the contrasts of skyrmions are strongly enhanced after the LoG filtering.

where  $m$  is the length of the kernel vector  $K$ . In the convolution process, the kernel is slided throughout the input and the sums of the products of corresponding elements are calculated as the new elements in the result.

For the Gaussian filter, the kernel is:

$$G(x, y) = \frac{1}{2\pi\sigma^2} e^{-\frac{x^2+y^2}{2\sigma^2}} \quad (\text{A.3})$$

Gaussian filter is a low-pass filter, thus it is usually used for "blurring" the image, *i.e.* to smooth the image and reduce the noise.

The kernel of the LoG filter is:

$$\text{LoG}(x, y) = -\frac{1}{\pi\sigma^4} \left(1 - \frac{x^2 + y^2}{2\sigma^2}\right) e^{-\frac{x^2+y^2}{2\sigma^2}} \quad (\text{A.4})$$

The LoG filter is very crucial in my work since its effect is to emphasize objects in the image with a round shape, or as their are wide called, "blobs". Skyrmions are such kind of blobs that extremely suitable for LoG filter, as can be clearly seen in Fig. A.1. Note that skyrmions hidden inside a very dark region show up after filtering. Another good properties of LoG is that the local minimum of a blob in the filtered image corresponds to the center of mass of the blob in the original image, as a result, the following skyrmion identification process can be significantly simplified into searching for the local minima, without losing precision in the center positioins of skyrmions.

Fourier transform (FT) is widely used in analyzing signals in the frequency domain, either temporal or spacial. The FT of  $f(t)$  is defined as:

$$g(\omega) = \int_{-\infty}^{+\infty} f(t) e^{-i2\pi\omega t} dt \quad (\text{A.5})$$

In the image processing, discrete Fourier transform (DFT) is used:

$$g_k = \sum_{j=1}^N f_j e^{-\frac{i2\pi j}{N} k} \quad k = 0, \dots, N-1 \quad (\text{A.6})$$

where  $N$  is the length of  $f$ .

Calculations directly based on Eq. A.6 have a complexity of  $O(N^2)$ , and the employment of a fast Fourier transform algorithm can reduce it to  $O(N \ln N)$ . The FFT used in MATLAB is based on FFTW library.

## A.2 Image registration

When acquiring a series of images, part of them may shift with respect to the others due to the adjustment of parameters or fluctuations. One typical example of this is the images acquired for TIE analysis. Tuning the focus of the lenses will induce displacement of images. The TIE calculation, however, relies very much on the alignment of the regions of interest. Thus aligning all images is usually the first step when dealing with image series. This process is also called registration in image processing.

Using MATLAB, the image registration can be achieved through two steps. Firstly, an estimation of transformation needed to align two images is obtained by calculating the phase correlations between the two images. Then the result is used as the initial condition for an optimization based registration process. The former step is good for finding the gross registration and the latter one is good for calculating the precise alignment. The combination of the two steps results in very good alignment for image series analyzed in this thesis. One example is shown in Fig. A.2

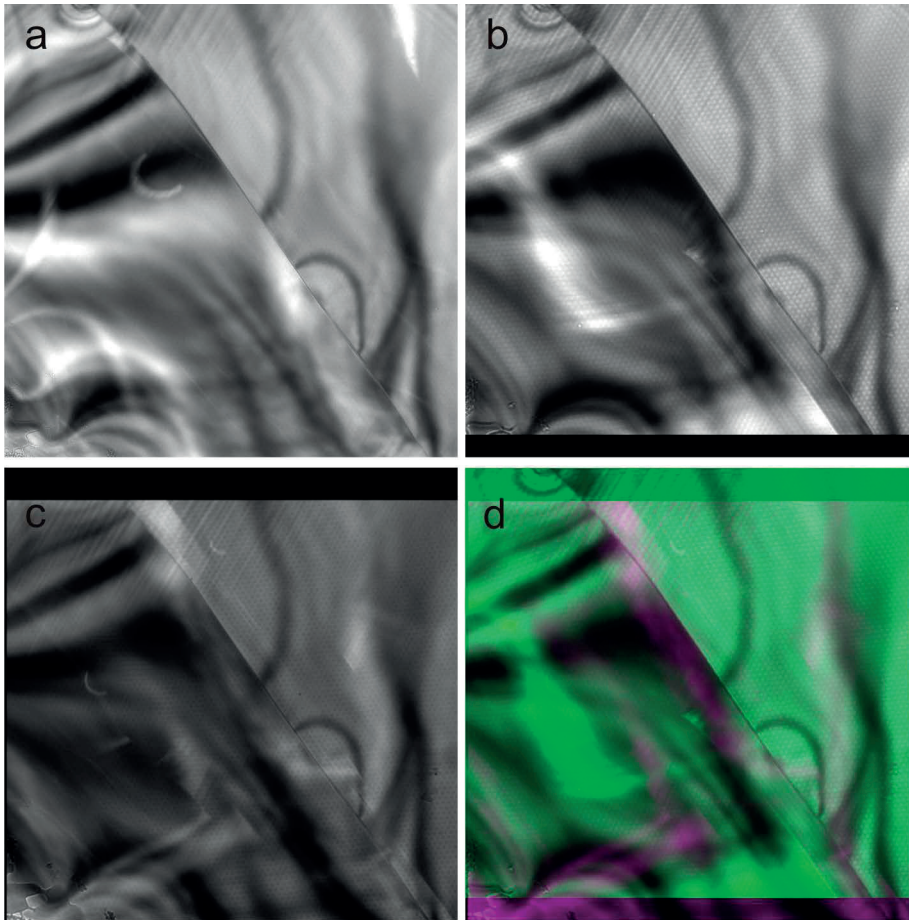


Figure A.2 – Image registration. **b.** and **c.** are images registered with respect to **a.**, and **d.** shows the overlap of **b.** and **c.** in green and magenta level respectively, thus in the well aligned regions one can see only the green color since it was put on top of the other one. Only small a portion of the overlapped image shows the second color, demonstrating a perfect alignment.



## B Algorithm of skyrmion identification

### B.1 Images full of skyrmnions

In my work, if an image is fully filled by skyrmions, it implies that the distances between skyrmions and their sizes are nearly the same respectively, since both are determined only by internal parameters of the system, *i.e.*, by  $J$  and  $|\mathbf{D}|$ . After LoG filtering of the images, skyrmions are highlighted with their centers of mass being the local minima. Then, the problem becomes the identification of those minima.

A scan throughout the image by a small square box approximately the same size as the skyrmions will be carried out. As illustrated in Fig. B.1, the scan is "dynamical", that is, moving the box until a local minimum is at the center of the box. It is of big advantages in this way: firstly, it is not sensitive how the skyrmions are arranged in the image, whether forming lattice or isotropic, whether the lattice vectors parallel with the horizontal or longitudinal directions or having an angle; second, the only pre-set parameter is the size of the box, and then the algorithm will work automatically.

For more complicated cases, however, more parameters are needed for a good identification. For example, if skyrmions only appear in part of the image, leaving the other region magnetically trivial, then a proper chosen threshold will be introduced in addition to the process described above.

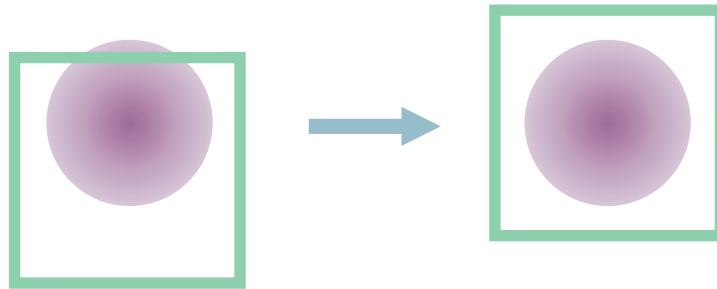


Figure B.1 – Illustration of the dynamical box algorithm.

### B.2 Images with both skyrmions and helices

There is a special case in which skyrmions embed in the background of the helical phase, as commonly seen in the E-field creation experiments. Ideally, the helical phase should be homogeneous along the stripes, but in practice, especially after the LoG filtering, there are always local minima with similar symmetry as skyrmions. Simply employing the scan algorithm will then confuse those minima inside the helical phase with the true skyrmions, leading to dramatic errors.

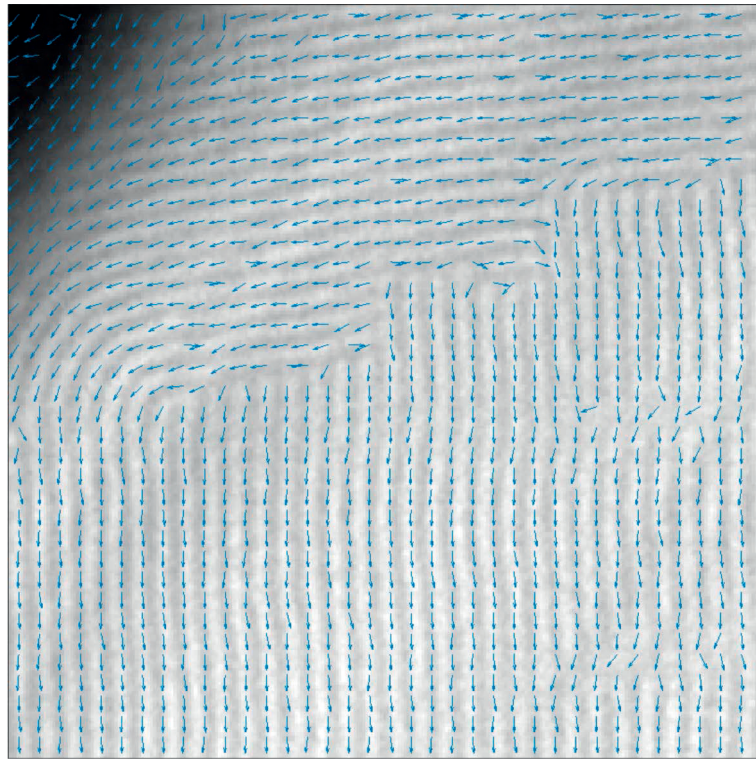


Figure B.2 – Orientational map of an image containing two helical domains.

On the other hand, since gray level of the helical phase is usually similar to that of skyrmions in the same image, setting a threshold will not help much, if not totally useless. Note that the most important difference between helices and skyrmions is that the former have a strong anisotropy while the latter are more isotropic. To make fully use of this point, a technique that widely used in the finger print identification is then adopted in this case, that is, calculating the orientational map of the image[80, 81].

The image will first be divided into small  $w \times w$  sized boxes, then local orientation  $\theta$  of a box

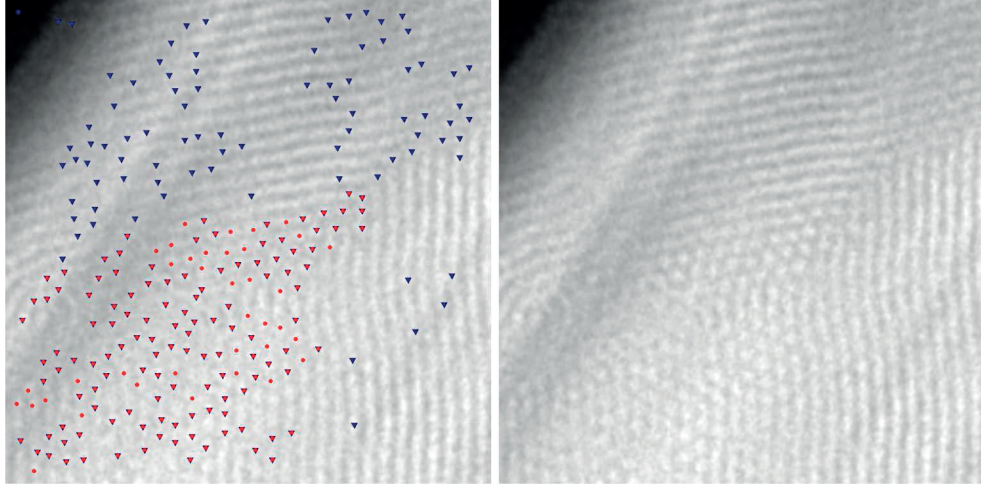


Figure B.3 – The left panel shows the skyrmion identification with the presence of helical phase background. Blue triangles indicate the results of the automatic algorithm and red circles denote the manually corrected skyrmion positions. Original image is shown on the right panel.

centered at  $(u, v)$  will be estimated as the following[79]:

$$\begin{aligned}
 V_x(u, v) &= \sum_{i=u-\frac{w}{2}}^{u+\frac{w}{2}} \sum_{j=v-\frac{w}{2}}^{v+\frac{w}{2}} 2\partial_x(i, j)\partial_y(i, j) \\
 V_y(u, v) &= \sum_{i=u-\frac{w}{2}}^{u+\frac{w}{2}} \sum_{j=v-\frac{w}{2}}^{v+\frac{w}{2}} \left( \partial_x^2(i, j)\partial_y^2(i, j) \right) \\
 \theta(u, v) &= \frac{1}{2} \arctan\left(\frac{V_y(u, v)}{V_x(u, v)}\right)
 \end{aligned} \tag{B.1}$$

Here,  $(\partial_x(i, j), \partial_y(i, j))$  is the gradient of pixel  $(i, j)$ . Fig. B.2 shows an example of the orientational map of a image in which two helical domains co-exist. Then skyrmions embedded in helical phase can be identified if a local minimum inside a box that has a local orientation significantly different from its neighbours, as shown in Fig. B.3.

This algorithm was used to count the number of skyrmions in image series with the presence of the helical phase, as can be found in Ch. 5. Although it does give artifacts in the results, but if images are acquired in the same condition with short time intervals, then these artifacts will most probably be a nearly constant background, which is just the case shown in Ch. 5.



# Bibliography

- [1] Hans-Hennig von Grünberg, Peter Keim, and Georg Maret. Phase Transitions in Two-Dimensional Colloidal Systems. In Gerhard Gompper and Michael Schick, editors, *Soft Matter*, pages 41–86. Wiley-VCH Verlag GmbH & Co. KGaA, 2007. [\(document\)](#), [4.1](#), [4.2](#), [4.3](#)
- [2] S. Mühlbauer, B. Binz, F. Jonietz, C. Pfleiderer, A. Rosch, A. Neubauer, R. Georgii, and P. Böni. Skyrmion Lattice in a Chiral Magnet. *Science*, 323(5916):915–919, 2009. [1](#), [1.1](#), [1.3.2](#)
- [3] Naoto Nagaosa and Yoshinori Tokura. Topological properties and dynamics of magnetic skyrmions. *Nature Nanotechnology*, 8(12):899–911, 2013. [1](#), [1.2.2](#), [1.2.3](#), [1.4](#)
- [4] X. Z. Yu, Y. Onose, N. Kanazawa, J. H. Park, J. H. Han, Y. Matsui, N. Nagaosa, and Y. Tokura. Real-space observation of a two-dimensional skyrmion crystal. *Nature*, 465(7300):901–904, 2010. [1](#), [1.1](#)
- [5] Minhyea Lee, Y. Onose, Y. Tokura, and N. P. Ong. Hidden constant in the anomalous Hall effect of high-purity magnet MnSi. *Physical Review B*, 75(17):172403, 2007. [1](#)
- [6] A. Neubauer, C. Pfleiderer, B. Binz, A. Rosch, R. Ritz, P. G. Niklowitz, and P. Böni. Topological Hall Effect in the a Phase of MnSi. *Physical Review Letters*, 102(18):186602, 2009. [1](#), [1.3](#), [1.2.2](#), [1.2.2](#), [1.6](#), [1.3.2](#)
- [7] J. S. White, K. Prša, P. Huang, A. A. Omrani, I. Živković, M. Bartkowiak, H. Berger, A. Magrez, J. L. Gavilano, G. Nagy, J. Zang, and H. M. Rønnow. Electric-Field-Induced Skyrmion Distortion and Giant Lattice Rotation in the Magnetoelectric Insulator Cu<sub>2</sub>OSeO<sub>3</sub>. *Physical Review Letters*, 113(10):107203, 2014. [1](#), [2.2.3](#), [2.2.3](#), [2.12](#)
- [8] Karin Everschor, Markus Garst, R. A. Duine, and Achim Rosch. Current-induced rotational torques in the skyrmion lattice phase of chiral magnets. *Physical Review B*, 84(6):064401, 2011. [1](#), [1.2.3](#)
- [9] Wanjun Jiang, Pramey Upadhyaya, Wei Zhang, Guoqiang Yu, M. Benjamin Jungfleisch, Frank Y. Fradin, John E. Pearson, Yaroslav Tserkovnyak, Kang L. Wang, Olle Heinonen, Suzanne G. E. te Velthuis, and Axel Hoffmann. Blowing magnetic skyrmion bubbles. *Science*, 349(6245):283–286, 2015. [1](#), [1.2.3](#)

## Bibliography

---

- [10] Albert Fert, Vincent Cros, and João Sampaio. Skyrmions on the track. *Nature Nanotechnology*, 8(3):152–156, 2013. [1](#), [1.1](#), [1.2](#)
- [11] T. H. R. Skyrme. A unified field theory of mesons and baryons. *Nuclear Physics*, 31:556–569, 1962. [1.1](#)
- [12] A. N. Bogdanov and D. A. Yablonskii. Thermodynamically stable "vortices" in magnetically ordered crystals. The mixed state of magnets. *Zh. Eksp. Teor. Fiz.*, 95(1):178 – 182, 1989. [1.1](#)
- [13] L. Brey, H. A. Fertig, R. Côté, and A. H. MacDonald. Skyrme Crystal in a Two-Dimensional Electron Gas. *Physical Review Letters*, 75(13):2562–2565, 1995. [1.1](#), [4.4](#)
- [14] A. G. Green, I. I. Kogan, and A. M. Tsvelik. Skyrmions in the quantum Hall effect at finite Zeeman coupling. *Physical Review B*, 54(23):16838–16849, 1996. [1.1](#), [4.4](#)
- [15] I. Kézsmárki, S. Bordács, P. Milde, E. Neuber, L. M. Eng, J. S. White, H. M. Rønnow, C. D. Dewhurst, M. Mochizuki, K. Yanai, H. Nakamura, D. Ehlers, V. Tsurkan, and A. Loidl. Néel-type skyrmion lattice with confined orientation in the polar magnetic semiconductor  $\text{GaV}_4\text{S}_8$ . *Nature Materials*, 14(11):1116–1122, 2015. [1.1](#), [1.1](#)
- [16] Christian Pfleiderer. Magnetic order: Surfaces get hairy. *Nature Physics*, 7(9):673–674, 2011. [1.1](#)
- [17] I. Dzyaloshinsky. A thermodynamic theory of “weak” ferromagnetism of antiferromagnetics. *Journal of Physics and Chemistry of Solids*, 4(4):241–255, 1958. [1.1](#)
- [18] Tôru Moriya. Anisotropic Superexchange Interaction and Weak Ferromagnetism. *Physical Review*, 120(1):91–98, 1960. [1.1](#)
- [19] X. Z. Yu, N. Kanazawa, Y. Onose, K. Kimoto, W. Z. Zhang, S. Ishiwata, Y. Matsui, and Y. Tokura. Near room-temperature formation of a skyrmion crystal in thin-films of the helimagnet  $\text{FeGe}$ . *Nature Materials*, 10(2):106–109, 2011. [1.1](#)
- [20] S. Seki, X. Z. Yu, S. Ishiwata, and Y. Tokura. Observation of Skyrmions in a Multiferroic Material. *Science*, 336(6078):198–201, 2012. [1.1](#), [2.3](#), [2.2.2](#), [2.6](#), [3.3](#)
- [21] S. Seki, S. Ishiwata, and Y. Tokura. Magnetoelectric nature of skyrmions in a chiral magnetic insulator  $\text{Cu}_2\text{OSeO}_3$ . *Physical Review B*, 86(6):060403, 2012. [1.1](#), [2.1.2](#), [2.2.2](#), [2.6](#)
- [22] Y. Tokunaga, X. Z. Yu, J. S. White, H. M. Rønnow, D. Morikawa, Y. Taguchi, and Y. Tokura. A new class of chiral materials hosting magnetic skyrmions beyond room temperature. *Nature Communications*, 6:7638, 2015. [1.1](#)
- [23] B. Binz and A. Vishwanath. Chirality induced anomalous-Hall effect in helical spin crystals. *Physica B: Condensed Matter*, 403:1336–1340, 2008. [1.2.1](#)

- 
- [24] Hans-Benjamin Braun. Topological effects in nanomagnetism: from superparamagnetism to chiral quantum solitons. *Advances in Physics*, 61(1):1–116, 2012. [1.2.1](#), [1.2.1](#)
- [25] Dong Liang, John P. DeGrave, Matthew J. Stolt, Yoshinori Tokura, and Song Jin. Current-driven dynamics of skyrmions stabilized in MnSi nanowires revealed by topological Hall effect. *Nature Communications*, 6:8217, 2015. [1.2.2](#)
- [26] Christian Pfleiderer and Achim Rosch. Condensed-matter physics: Single skyrmions spotted. *Nature*, 465(7300):880–881, June 2010. [1.3](#)
- [27] Yoshinori Tokura and Shinichiro Seki. Multiferroics with Spiral Spin Orders. *Advanced Materials*, 22(14):1554–1565, 2010. [1.2.3](#)
- [28] Jiadong Zang, Maxim Mostovoy, Jung Hoon Han, and Naoto Nagaosa. Dynamics of Skyrmion Crystals in Metallic Thin Films. *Physical Review Letters*, 107(13):136804, 2011. [1.2.3](#)
- [29] Karin Everschor, Markus Garst, Benedikt Binz, Florian Jonietz, Sebastian Mühlbauer, Christian Pfleiderer, and Achim Rosch. Rotating skyrmion lattices by spin torques and field or temperature gradients. *Physical Review B*, 86(5):054432, 2012. [1.2.3](#)
- [30] R. Tomasello, E. Martinez, R. Zivieri, L. Torres, M. Carpentieri, and G. Finocchio. A strategy for the design of skyrmion racetrack memories. *Scientific Reports*, 4:6784, 2014. [1.2.3](#)
- [31] Xichao Zhang, Yan Zhou, Motohiko Ezawa, G. P. Zhao, and Weisheng Zhao. Magnetic skyrmion transistor: skyrmion motion in a voltage-gated nanotrack. *Scientific Reports*, 5:11369, 2015. [1.2.3](#)
- [32] F. Jonietz, S. Mühlbauer, C. Pfleiderer, A. Neubauer, W. Münzer, A. Bauer, T. Adams, R. Georgii, P. Böni, R. A. Duine, K. Everschor, M. Garst, and A. Rosch. Spin Transfer Torques in MnSi at Ultralow Current Densities. *Science*, 330(6011):1648–1651, 2010. [1.2.3](#)
- [33] X. Z. Yu, N. Kanazawa, W. Z. Zhang, T. Nagai, T. Hara, K. Kimoto, Y. Matsui, Y. Onose, and Y. Tokura. Skyrmion flow near room temperature in an ultralow current density. *Nature Communications*, 3:988, 2012. [1.2.3](#)
- [34] Hiroshi Oike, Akiko Kikkawa, Naoya Kanazawa, Yasujiro Taguchi, Masashi Kawasaki, Yoshinori Tokura, and Fumitaka Kagawa. Interplay between topological and thermodynamic stability in a metastable magnetic skyrmion lattice. *Nature Physics*, 12(1):62–66, 2016. [1.3.2](#), [5.3](#)
- [35] K. Karube, J. S. White, N. Reynolds, J. L. Gavilano, H. Oike, A. Kikkawa, F. Kagawa, Y. Tokunaga, H. M. Rønnow, Y. Tokura, and Y. Taguchi. Robust metastable skyrmions and their triangular–square lattice structural transition in a high-temperature chiral magnet. *Nature Materials*, 15(12):1237–1242, 2016. [1.3.2](#), [4.3.1](#)



## Bibliography

---

- [36] Koya Makino, Johannes D. Reim, Daiki Higashi, Daisuke Okuyama, Taku J. Sato, Yusuke Nambu, Elliot P. Gilbert, Norman Booth, Sinichiro Seki, and Yoshinori Tokura. Thermal stability and irreversibility of skyrmion-lattice phases in  $\text{Cu}_2\text{OSeO}_3$ . *arXiv:1608.06359 [cond-mat]*, 2016. [1.3.2](#)
- [37] I. Levatić, P. Popčević, V. Šurija, A. Kruchkov, H. Berger, A. Magrez, J. S. White, H. M. Rønnow, and I. Živković. Dramatic pressure-driven enhancement of bulk skyrmion stability. *Scientific Reports*, 6:21347, 2016. [1.3.2](#)
- [38] Y. Okamura, F. Kagawa, S. Seki, and Y. Tokura. Transition to and from the skyrmion lattice phase by electric fields in a magnetoelectric compound. *Nature Communications*, 7:12669, 2016. [1.3.2](#)
- [39] M. Mochizuki, X. Z. Yu, S. Seki, N. Kanazawa, W. Koshibae, J. Zang, M. Mostovoy, Y. Tokura, and N. Nagaosa. Thermally driven ratchet motion of a skyrmion microcrystal and topological magnon Hall effect. *Nature Materials*, 13(3):241–246, 2014. [1.3.2](#), [3.5](#)
- [40] Jan-Willem G. Bos, Claire V. Colin, and Thomas T. M. Palstra. Magnetoelectric coupling in the cubic ferrimagnet  $\text{Cu}_2\text{OSeO}_3$ . *Physical Review B*, 78(9):094416, 2008. [2.1](#)
- [41] Jin-Hong Park and Jung Hoon Han. Zero-temperature phases for chiral magnets in three dimensions. *Physical Review B*, 83(18):184406, 2011. [2.1.1](#), [2.1.1](#), [2.1.1](#), [3.3](#)
- [42] L. D. Landau, E.M. Lifshitz. *Electrodynamics of Continuous Media*. 1960. [2.1.1](#)
- [43] P. Bak and M. H. Jensen. Theory of helical magnetic structures and phase transitions in MnSi and FeGe. *Journal of Physics C: Solid State Physics*, 13(31):L881, 1980. [2.1.1](#)
- [44] F. N. Rybakov, A. B. Borisov, and A. N. Bogdanov. Three-dimensional skyrmion states in thin films of cubic helimagnets. *Physical Review B*, 87(9):094424, 2013. [2.1.1](#)
- [45] Sumilan Banerjee, James Rowland, Onur Erten, and Mohit Randeria. Enhanced Stability of Skyrmions in Two-Dimensional Chiral Magnets with Rashba Spin-Orbit Coupling. *Physical Review X*, 4(3):031045, 2014. [2.1.1](#)
- [46] Utkan Güngördü, Rabindra Nepal, Oleg A. Tretiakov, Kirill Belashchenko, and Alexey A. Kovalev. Stability of skyrmion lattices and symmetries of quasi-two-dimensional chiral magnets. *Physical Review B*, 93(6):064428, 2016. [2.1.1](#)
- [47] Chenglong Jia, Shigeki Onoda, Naoto Nagaosa, and Jung Hoon Han. Bond electronic polarization induced by spin. *Physical Review B*, 74(22):224444, 2006. [2.1.2](#)
- [48] Chenglong Jia, Shigeki Onoda, Naoto Nagaosa, and Jung Hoon Han. Microscopic theory of spin-polarization coupling in multiferroic transition metal oxides. *Physical Review B*, 76(14):144424, 2007. [2.1.2](#)
- [49] Taka-hisa Arima. Ferroelectricity Induced by Proper-Screw Type Magnetic Order. *Journal of the Physical Society of Japan*, 76(7):073702, 2007. [2.1.2](#)

- 
- [50] H. Murakawa, Y. Onose, S. Miyahara, N. Furukawa, and Y. Tokura. Comprehensive study of the ferroelectricity induced by the spin-dependent d-p hybridization mechanism in  $\text{Ba}_2\text{XGe}_2\text{O}_7$  (X = Mn, Co, and Cu). *Physical Review B*, 85(17):174106, 2012. [2.1.2](#)
  - [51] M. Belesi, I. Rousochatzakis, M. Abid, U. K. Rößler, H. Berger, and J.-Ph. Ansermet. Magnetolectric effects in single crystals of the cubic ferrimagnetic helimagnet  $\text{Cu}_2\text{OSeO}_3$ . *Physical Review B*, 85(22):224413, 2012. [2.1.2](#)
  - [52] A. A. Omrani, J. S. White, K. Prša, I. Živković, H. Berger, A. Magrez, Ye-Hua Liu, J. H. Han, and H. M. Rønnow. Exploration of the helimagnetic and skyrmion lattice phase diagram in  $\text{Cu}_2\text{OSeO}_3$  using magnetoelectric susceptibility. *Physical Review B*, 89(6):064406, 2014. [2.2.2](#), [2.2.2](#), [2.2.2](#)
  - [53] Arash Alahgholipour Omrani. *Nanofabricated Devices based on Intrinsically Layered Correlated Electron Materials*. PhD thesis, 2013. [2.2.2](#)
  - [54] I. Živković, J. S. White, H. M. Rønnow, K. Prša, and H. Berger. Critical scaling in the cubic helimagnet  $\text{Cu}_2\text{OSeO}_3$ . *Physical Review B*, 89(6):060401, 2014. [2.2.2](#)
  - [55] Ye-Hua Liu, Jung Hoon Han, A. A. Omrani, H. M. Rønnow, and You-Quan Li. Theory of magneto-electric susceptibility in multiferroic chiral magnets. *arXiv:1310.5293 [cond-mat]*, 2013. [2.2.2](#)
  - [56] Kazuo Ishizuka and Brendan Allman. Phase measurement of atomic resolution image using transport of intensity equation. *Journal of Electron Microscopy*, 54(3):191–197, 2005. [3.1](#), [3.6](#)
  - [57] Jayaraman Rajeswari, Ping Huang, Giulia Fulvia Mancini, Yoshie Murooka, Tatiana Latychevskaia, Damien McGrouther, Marco Cantoni, Edoardo Baldini, Jonathan Stuart White, Arnaud Magrez, Thierry Giamarchi, Henrik Moodysson Rønnow, and Fabrizio Carbone. Filming the formation and fluctuation of skyrmion domains by cryo-Lorentz transmission electron microscopy. *Proceedings of the National Academy of Sciences*, 112(46):14212–14217, 2015. [3.7](#), [3.4](#), [3.10](#), [3.11](#)
  - [58] Motohiko Ezawa. Compact merons and skyrmions in thin chiral magnetic films. *Physical Review B*, 83(10):100408, 2011. [3.4](#)
  - [59] Shi-Zeng Lin, Avadh Saxena, and Cristian D. Batista. Skyrmion fractionalization and merons in chiral magnets with easy-plane anisotropy. *Physical Review B*, 91(22):224407, 2015. [3.4](#)
  - [60] R. Peierls. Quelques propriétés typiques des corps solides. *Annales de l'institut Henri Poincaré*, 5(3):177–222, 1935. [3.6](#)
  - [61] N. D. Mermin. Crystalline Order in Two Dimensions. *Physical Review*, 176(1):250–254, 1968. [3.6](#), [4.3.3](#)

## Bibliography

---

- [62] J. M. Kosterlitz and D. J. Thouless. Ordering, metastability and phase transitions in two-dimensional systems. *Journal of Physics C: Solid State Physics*, 6(7):1181, 1973. [3.6](#), [4](#), [4.3.3](#)
- [63] Thierry Giamarchi and Pierre Le Doussal. Elastic theory of flux lattices in the presence of weak disorder. *Physical Review B*, 52(2):1242–1270, 1995. [3.6](#)
- [64] A. P. Young. Melting and the vector Coulomb gas in two dimensions. *Physical Review B*, 19(4):1855–1866, 1979. [4](#)
- [65] David R. Nelson and B. I. Halperin. Dislocation-mediated melting in two dimensions. *Physical Review B*, 19(5):2457–2484, 1979. [4](#), [4.3.3](#), [4.3.3](#)
- [66] F. A. Lindemann. Ueber die berechnung molekularer eigenfrequenzen. *Physik. Z.*, 11:609–612, 1910. [4.1](#)
- [67] K. Zahn, R. Lenke, and G. Maret. Two-Stage Melting of Paramagnetic Colloidal Crystals in Two Dimensions. *Physical Review Letters*, 82(13):2721–2724, 1999. [4.1](#), [4.3.3](#)
- [68] I. Guillamón, R. Córdoba, J. Sesé, J. M. De Teresa, M. R. Ibarra, S. Vieira, and H. Suderow. Enhancement of long-range correlations in a 2d vortex lattice by an incommensurate 1d disorder potential. *Nature Physics*, 10(11):851–856, 2014. [4.1](#)
- [69] J. Lu and J. A. Szpunar. Applications of the embedded-atom method to glass formation and crystallization of liquid and glass transition-metal nickel. *Philosophical Magazine A*, 75(4):1057–1066, 1997. [4.3.1](#)
- [70] Zhibin Lin and Leonid V. Zhigilei. Time-resolved diffraction profiles and atomic dynamics in short-pulse laser-induced structural transformations: Molecular dynamics study. *Physical Review B*, 73(18):184113, 2006. [4.3.2](#)
- [71] Carsten Timm, S. M. Girvin, and H. A. Fertig. Skyrmion lattice melting in the quantum Hall system. *Physical Review B*, 58(16):10634–10647, 1998. [4.4](#)
- [72] Toshiaki Tanigaki, Kiyohito Shibata, Naoya Kanazawa, Xiuzhen Yu, Yoshinori Onose, Hyun Soon Park, Daisuke Shindo, and Yoshinori Tokura. Real-Space Observation of Short-Period Cubic Lattice of Skyrmions in MnGe. *Nano Letters*, 15(8):5438–5442, 2015. [4.4](#)
- [73] V. Bayot, E. Grivei, S. Melinte, M. B. Santos, and M. Shayegan. Giant Low Temperature Heat Capacity of GaAs Quantum Wells near Landau Level Filling  $\nu = 1$ . *Physical Review Letters*, 76(24):4584–4587, 1996. [4.4](#)
- [74] P. Milde, D. Köhler, J. Seidel, L. M. Eng, A. Bauer, A. Chacon, J. Kindervater, S. Mühlbauer, C. Pfleiderer, S. Buhrandt, C. Schütte, and A. Rosch. Unwinding of a Skyrmion Lattice by Magnetic Monopoles. *Science*, 340(6136):1076–1080, 2013. [4.4](#)

- 
- [75] Niklas Romming, Christian Hanneken, Matthias Menzel, Jessica E. Bickel, Boris Wolter, Kirsten von Bergmann, André Kubetzka, and Roland Wiesendanger. Writing and Deleting Single Magnetic Skyrmions. *Science*, 341(6146):636–639, August 2013. [5](#)
  - [76] Pin-Jui Hsu, André Kubetzka, Aurore Finco, Niklas Romming, Kirsten von Bergmann, and Roland Wiesendanger. Electric field driven switching of individual magnetic skyrmions. *arXiv:1601.02935 [cond-mat]*, 2016. [5](#)
  - [77] Masahito Mochizuki and Yoshio Watanabe. Writing a skyrmion on multiferroic materials. *Applied Physics Letters*, 107(8):082409, 2015. [5](#)
  - [78] Masahito Mochizuki. Creation of Skyrmions by Electric Field on Chiral-Lattice Magnetic Insulators. *Advanced Electronic Materials*, 2(1):1500180, 2016. [5](#)
  - [79] Lin Hong, Yifei Wan, and A. Jain. Fingerprint image enhancement: algorithm and performance evaluation. *IEEE Transactions on Pattern Analysis and Machine Intelligence*, 20(8):777–789, 1998. [A.1](#), [B.2](#)
  - [80] A. R. Rao and B. G. Schunck. Computing oriented texture fields. In *IEEE Computer Society Conference on Computer Vision and Pattern Recognition, 1989. Proceedings CVPR '89*, pages 61–68, 1989. [B.2](#)
  - [81] A. R. Rao and R. C. Jain. Computerized flow field analysis: oriented texture fields. *IEEE Transactions on Pattern Analysis and Machine Intelligence*, 14(7):693–709, 1992. [B.2](#)



# Curriculum Vitae

## Ping Huang

Gender: Male

Born: 04/01/1984

Nationality: Chinese

Email: [ping.huang@epfl.ch](mailto:ping.huang@epfl.ch)

Current Affiliation: Laboratory for Quantum Magnetism, École Polytechnique Fédérale de Lausanne



## Education:

**Ph.D candidate:** Laboratory for Quantum Magnetism (LQM), École Polytechnique Fédérale de Lausanne (EPFL), Lausanne, Switzerland, Jan. 2013 – present

**M.Sc.:** School of Physics, Wuhan University, Wuhan, China, Sep. 2006 – Jun. 2008  
Condensed Matter Physics

**B.Sc.:** School of Physics, Wuhan University, Wuhan, China, Sep. 2002 – Jun. 2006  
Condensed Matter Physics

## Research Interests:

Emergent and dynamical properties of strongly correlated electron materials.

Structure, charge, spin and orbital ordering and their collective excitations via various experimental measurements.

Phase transition, criticality and complexity by experiments and computational simulations.

## Research Experiences:

Jan. 2012 – present, Dynamic properties of skyrmion in magnetoelectric coupling helimagnet  $\text{Cu}_2\text{OSeO}_3$  by Lorentz Electron transmission electron microscopy (LTEM)

Jan. 2009 – Dec. 2011, Structure, electronic and magnetic properties of nitrophenyl diazonium functionalized graphene

Sep. 2006 – Jun. 2008, Charge and orbital ordering in spinel compound  $\text{MgTi}_2\text{O}_4$  via electric transport investigations, and experimental study and Monte Carlo simulation of liquid-gas type phase-transition of spin ice compound  $\text{Dy}_2\text{Ti}_2\text{O}_7$  induced by magnetic field along  $[111]$  direction

## Publication List

- [1] Jayaraman Rajeswari, Ping Huang, Giulia Fulvia Mancini, Yoshie Murooka, Tatiana Latychevskaia, Damien McGrouther, Marco Cantoni, Edoardo Baldini, Jonathan Stuart White, Arnaud Magrez, Thierry Giamarchi, Henrik Moodysson Rønnow, and Fabrizio Carbone. Filming the formation and uctuation of skyrmion domains by cryo-Lorentz transmission electron microscopy. *Proc.Natl. Acad. of Sci.*, 112: 14212, 2015.
- [2] J. S. White, K. Prša, P. Huang, A. A. Omrani, I. Živković, M. Bartkowiak, H. Berger, A. Magrez, J. L. Gavilano, G. Nagy, J. Zang, and H.M. Rønnow. Electric-Field-Induced Skyrmion Distortion and Giant Lattice Rotation in the Magnetoelectric Insulator  $\text{Cu}_2\text{OSeO}_3$ . *Phys. Rev. Lett.*, 113: 107203, 2014.
- [3] Ping Huang, Long Jing, Huarui Zhu, and Xueyun Gao. Diazonium Functionalized Graphene: Microstructure, Electric, and Magnetic Properties. *Acc. Chem. Res.*, 46: 43, 2013.
- [4] Ping Huang, Huarui Zhu, Long Jing, Yuliang Zhao, and Xueyun Gao. Graphene Covalently Binding Aryl Groups: Conductivity Increases Rather than Decreases. *ACS Nano*, 5: 7945, 2011.
- [5] Ping Huang, Huarui Zhu, Long Jing, Taisen Zuo, Yuliang Zhao, and Xueyun Gao. Microstructure evolution of diazonium functionalized graphene: A potential approach to change graphene electronic structure. *J. Mater. Chem.*, 22: 2063, 2012.
- [6] Ping Huang, Long Jing, Hua Rui Zhu, and Xue Yun Gao. Transport properties of diazonium functionalized graphene: chiral two-dimensional hole gases. *J. Phys.: Condens. Matter*, 24: 235305, 2012.
- [7] Long Jing, Ping Huang, Huarui Zhu, and Xueyun Gao. Spin-Polarized Semiconductors: Tuning the Electronic Structure of Graphene by Introducing a Regular Pattern of  $\text{sp}^3$  Carbons on the Graphene Plane. *Small*, 9: 306, 2013.
- [8] V. Dyadkin, K. Prša, S. V. Grigoriev, J. S. White, P. Huang, H. M. Rønnow, A. Magrez, C. D. Dewhurst, and D. Chernyshov. Chirality of structure and magnetism in the magnetoelectric compound  $\text{Cu}_2\text{OSeO}_3$ . *Phys. Rev. B*, 89: 140409, 2014.
- [9] A. Pisoni, S. Katrych, A. Arakcheeva, T. Verebélyi, M. Bokor, P. Huang, R. Gaál, P. Matus, J. Karpinski, and L. Forró. Single crystals of superconducting  $\text{SmFeAsOH}_x$ : structure and properties. *Phys. Rev. B*, 94: 024525, 2016.



